2023-07

Thermo-Electro-Optical Properties of Disordered Nanowire Networks

Esteki, Koorosh

UNIVERSITY OF CALGARY

Thermo-Electro-Optical Properties of Disordered Nanowire Networks

by

Koorosh Esteki

A THESIS

SUBMITTED TO THE FACULTY OF GRADUATE STUDIES

IN PARTIAL FULFILLMENT OF THE REQUIREMENTS FOR THE

DEGREE OF DOCTOR OF PHILOSOPHY

GRADUATE PROGRAM IN PHYSICS AND ASTRONOMY

CALGARY, ALBERTA

JULY, 2023

Abstract

Metallic nanowire networks are promising candidates for next-generation transparent conductors, owing to their exceptional electrical and thermal conductivity, high optical transparency, and mechanical flexibility. A nanowire network is a disordered arrangement of nanowires that exhibits no discernible long-range order or periodicity. Previous studies have placed significant emphasis on the individual analysis of electrical resistance, optical transmission, and thermal conduction in diverse network materials. Nonetheless, insufficient focus has been devoted to comprehending the relationship between the multiple extrinsic and intrinsic variables that characterize a disordered nanowire network (or an ensemble of them) and the trade-offs that arise when investigating the system response trio of namely electrical/optical/thermal natures. This thesis presents a comprehensive computational study that exclusively employs theoretical and numerical models to examine the thermoelectric and optical characteristics of two types of disordered metallic nanowire networks: (i) junction-based random nanowire networks and (ii) seamless random nanowire networks. The raw materials that compose their nanowires are metals namely, silver, gold, copper, and aluminium and we used a variety of computational tools to obtain prominent physical quantities that infer the network's performance such as sheet (electrical) resistance, optical transmission, and temperature variation. A range of adjustable parameters, including those pertaining to geometrical structure in device design, have been systematically tuned in order to conduct a figure of merit analysis with respect to thermal and electrical conduction, and optical transmission of the network materials. Moreover, we obtained local current and temperature mappings that detail the conduction mechanisms used by the networks to propagate signals through their disordered skeleton. We verified that, under certain conditions, junction-based and seamless nanowire networks fall into the same temperature distribution mechanisms that can be generally described with Weibull probability density functions. This study offers valuable insights into the electrical/optical/thermal performance of disordered nanowire networks prone to transparent conductor applications.

Preface

Publications resulting, partially or wholly, from this work:

- **K. Esteki**, D. Curic, H. G. Manning, E. Sheerin, M. S. Ferreira, J. J. Boland, and C. G. Rocha, "Thermo-electro-optical properties of seamless metallic nanowire networks for transparent conductor applications", Nanoscale 15, 10394 (2023).

- **K. Esteki**, H. G. Manning, E. Sheerin, M. S. Ferreira, J. J. Boland, and C. G. Rocha, "Tuning the electro-optical properties of nanowire networks", Nanoscale 13, 15369 (2021).

- S. Alialy, **K. Esteki**, M. S. Ferreira, J. J. Boland, and C. G. Rocha, "Nonlinear ion drift-diffusion memristance description of TiO_2 RRAM devices", Nanoscale Advances 2, 2514 (2020).

Land Acknowledgement

This research was carried out in Calgary. We acknowledge and pay tribute to the traditional territories of the peoples of Treaty 7, which include the Blackfoot Confederacy (comprised of the Siksika, the Piikani, and the Kainai First Nations), the Tsuut'ina First Nation, and the Stoney Nakoda (including Chiniki, Bearspaw, and Goodstoney First Nations). The City of Calgary is also home to the Métis Nation of Alberta Region 3.

Acknowledgements

Table of Contents

List of Figures and Illustrations

List of Tables

List of Symbols, Abbreviations and Nomenclature

Symbol	Definition
0D	Zero Dimension
1D	One Dimension
2D	Two Dimensions
3D	Three Dimensions
AR	Aspect Ratio
$AR_\circ$	Aspect Ratio of Cylindrical Nanowire
$AR_\blacksquare$	Aspect Ratio Rectangular Nano Channel
AF	Area Fraction
CAD	Computer-Aided Design
D_w	Depth of Rectangular Nano Channel
DC	Direct Current
d_w	Diameter of Cylindrical Nanowire
EC	Electric Current
EMT	Effective Medium Theory
EMI SE	Electromagnetic Interference Shielding Effectiveness
FOM	Figure(s) of Merit
FEM	Finite Element Method
GUI	Graphical User Interface
HT	Heat Transfer
h_{cond}	Heat Transfer Coefficients
ITO	Indium Tin Oxide
JDA	Junction Dominated Assumption
k_{cond}	Thermal Conductivity
L_w	Length of Nanowire
MNA	Modified Nodal Analysis
MNR	Multi-Nodal Representation
MLST	Mie Light Scattering Theory
NWN(s)	Nanowire Network(s)
NDR	Negative Differential Resistance
n_w	Network Density
n_c	Network Critical Density/Curved Nanowire Network Density

n_j	Junction Density
ODE	Ordinary Differential Equation(s)
PML	Perfectly Matched Layer
PEC(s)	Perfect Electric Conductor(s)
PDF	Probability Density Function
PET	Polyethylene Terephthalate
Q_{ext}	Optical Extinction Efficiency Factor
Q_{sca}	Optical Scattering Efficiency Factor
Q_{abs}	Optical Absorption Efficiency Factor
R_{jxn}	Junction Resistance
R_{in}	Inner Resistance
R_s	Sheet Resistance
R_c	Source/Drain Electrode Contact Resistance
RF	Radio Frequency
RRAM	Resistive Random Access Memory
SEM	Scanning Electron Microscopy
T_{op}	Optical Transmittance
T	Temperature
TEM	Transmission Electron Microscopy
TCE(s)	Transparent Conducting Electrode(s)
TC(s)	Transparent Conductor(s)
TM	Transverse Magnetic Mode
TE	Transverse Electric Mode
W_w	Width of Rectangular Nano Channel
ϵ_{radi}	Thermal Emissivity Coefficients
λ	Wavelength
ρ	Electrical Resistivity
σ_{opt}	Optical Conductivity
σ_{cond}	Electrical Conductivity
σ_{ext}	Optical Extinction Cross-Section
σ_{sca}	Optical Scattering Cross-Section
σ_{abs}	Optical Absorption Cross-Section
$\mathcal{L}$	Lorenz Number

Chapter 1

Introduction

1.1 Nanowire Networks

The significant advancements made in nanotechnology have a major impact on a wide range of modern industries [1–3]. It is well established that the properties of nanomaterials are highly connected to their physically constrained structures and intrinsic features, which include their geometrical shapes and sizes, atomic structure, and chemical compositions [4,5]. When a material's dimensions are shrunk to the nanoscale, its fundamental properties can be dramatically altered [6]. For instance, nanomaterials have a substantially higher surface-areas-to-volume ratio than their bulk counterparts, resulting in increased chemical reactivity/sensitivity and mechanical strength [7]. Similarly, at the nanoscale, quantum effects can become far more important in shaping the characteristics and properties of the materials, resulting in unique electrical, optical, thermal, mechanical, and magnetic behaviours [8]. For example, structural feature such as sufficiently large aspect ratios in nanomaterials is advantageous to light-propagation paths toward photonic circuit integrations [9]. Hence, identifying nanomaterials according to their physical properties is critical for comprehending the diversity of their nanostructures. They can be classified into four types according to their dimensions including zero dimension (0D), one dimension (1D), two dimensions (2D),

and three dimensions (3D) [10]. The majority of 0D nanomaterials are in the category of quantum dots with characteristic sizes smaller than 100 nm [11]; examples include Fullerene-based quantum dots [12], graphene quantum dots [13], carbon quantum dots [14], inorganic quantum dots [15], and magnetic nanoparticles [16]. Nanostructures are considered to be 1D if their thickness and width are in the nanoscale range but their length is in the micrometer (μm) range or greater. Nanowires [17], nanotubes [18] and nanofibers [19] are all examples of 1D nanomaterials. 2D nanomaterials have width and length that are in the micrometer range and yet their depth is in the very few nanometer (nm) range. Graphene, being one of the most commonly noted 2D materials, has unique characteristics that make it useful in a broad range of applications [20]. Materials that are not restricted to nanoscale in any dimension are called 3D materials or bulks; bundles of nanowires, nanotubes, and multi-layer materials may all be found in this category [21]. It is worth mentioning that materials manufactured in the mesoscale (~ 0.1 mm to 5 mm) can be viewed as bridging the gap between macro- and microscale systems because they share traits with both classifications while still holding their own distinct properties [22]. In this thesis, we will focus on 1D nanomaterials composed of solid wide segments with lengths of the order of micrometers and width/depth of the order of nanometers.

Nanowires can be metallic, semiconducting, or insulating based on their chemical compositions and electronic properties, with metallic and insulating nanowires being particularly suited for plasmonic, and photonic applications, while semiconducting nanowires show promise for light generation and sensing applications [25–27]. Metallic nanowires have been intensively studied as a valuable 1D nanostructure because of their unique features, which include outstanding thermal and electrical conductivity, high aspect ratio, remarkable mechanical flexibility, exceptional optical transparency, and so on [28–31]. As a result of this, metallic nanowires are being viewed as multifunctional engineering materials because of their unique properties, which are not present in their bulk equivalents [32, 33]. Metallic nanowires research has sparked innovation in a number of fields over the last two decades,
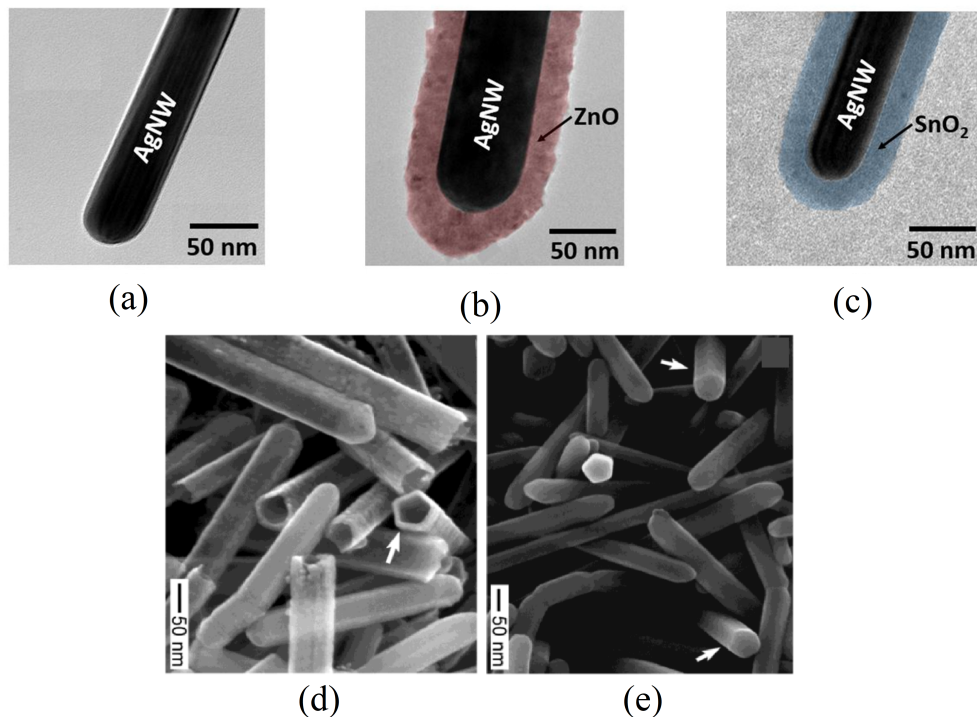
Figure 1.1: (Top panels) Transmission electron microscopy (TEM) images from [23]: (a) bare silver nanowire, (b) silver nanowire coated with ZnO, (c) and silver nanowire coated with SnO_2. (Bottom panels) Scanning electron microscopy (SEM) images: (d) gold nanotubes, and (e) silver nanowires. Panels (d,e): reprinted (adapted) with permission from reference [24]. Copyright 2003 American Chemical Society.

including flexible transparent conductive films and electrodes [34–36], conductive polymer nanocomposites [37, 38], touch sensors [39, 40], photovoltaic cells [41, 42], electrochromic devices [43, 44], wearable optoelectronic devices [45, 46], thermal energy storage [47, 48], biomedical science [49, 50] and chemical sensors [51, 52], brain-inspired neuromorphic computing applications [53, 54], and transparent heaters [55, 56]. Silver [57, 58], copper [59, 60], gold [61, 62], and aluminum nanowires [63, 64], in particular, have advanced rapidly on the frontier of metallic nanowire technologies, making them up-and-coming candidates for next-generation engineering materials [55, 65, 66]. The development of characterization techniques, on the other hand, has led to numerous synthesis processes that produce metallic nanowires of uniform size at minimal cost [29, 55, 65, 66]. Metallic nanowires have been manufactured using a variety of shape-controlled processes, including hard template [67], soft template [68],

electro-deposition [69], wet reduction [70], and chemical vapour deposition [71] methods. Among the numerous metallic nanowires, Ag, Au, Al, and Cu have received significant attention, owing to their similar physical and chemical properties at room temperature [31]. Figure 1.1 shows Ag nanowires and Au nanotubes fabricated at different geometries and compositions. Figure 1.1 (a-c) illustrate bare and coated Ag nanowires [23] whereas Figure 1.1 (d) evidences the hollow cross-section of Au nanotubes with bundles of (e) bare (solid) Ag nanowires [24].

Many of these nanowires can be bundled together to form thin films or synthetic layers that can be used in modern electronics. The need for faster, smaller, and more powerful electronics has been a significant driving force in increasing demands for transparent conductive electrodes which are crucial components for flexible thermoelectronic and optoelectronic devices [66, 72]. Indium Tin Oxides (ITO) is the most often used transparent conductive electrode material today, but limitations raise from its brittle ceramic nature, shortage of supply, and high cost of preparation using the vacuum deposition technique. Such challenges linked to ITO limit its broad use in emerging flexible devices and other next-generation applications [73]. Numerous efforts have been undertaken to produce ITO substitutes, including carbon nanotube networks [74], graphene thin films [75], conductive polymers [76], and metal nanowire networks (NWNs) [29, 73]. When deciding on the best material for a given application, it is critical to evaluate the costs associated with the raw materials and manufacturing procedures required to create the electrode or device component [29, 73]. Among these materials, metallic nanowires as transparent electrodes are considered promising candidates to replace ITO due to their superior electrical, thermal, mechanical, and optical properties and low cost of fabrication [29, 55, 66, 73]. Metal NWNs are composed of randomly distributed nanowires over a substrate in which the nanowire interconnects entangle in a disordered fashion to form a percolative network.
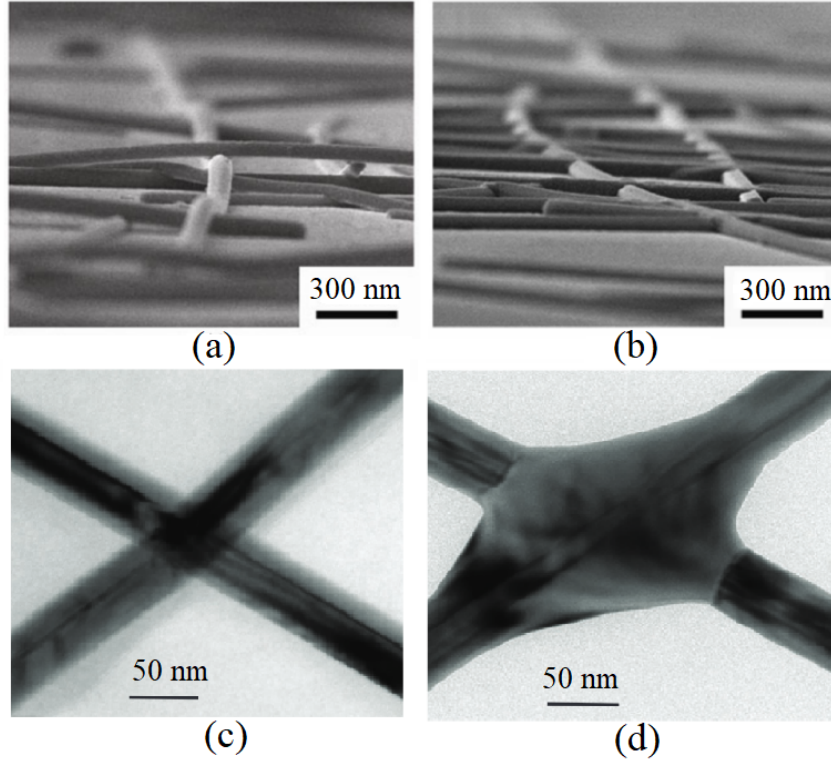
Figure 1.2: (a) SEM off-angle cross-sectional image reveals touching-wire (junction-based) connections in Ag nanowires. (b) SEM off-angle cross-sectional image reveals tightly linked Ag nanowires with smooth surfaces after mechanically compressed junction treatment. Panels (a,b): images from [77] and reproduced with permission from Springer Nature. (c) TEM image of an Ag nanowire junction before junction optical treatment. (d) TEM image of an Ag nanowire junction after optical welding. Panels (c,d): images from [78] and reproduced with permission from Springer Nature.

Solution-based deposition methods such as Meyer rod [79], dip, or spray coating [80] can be used to efficiently construct NWN samples of distinct sizes. Large junction resistances between intersecting nanowires in the network can be a result of the surface coatings of individual nanowires, which are generally made of insulating oxides or polymers [81, 82]. Direct measurements of junction resistances have been carried out for a variety of nanowire systems, and the influence of these observations on the overall device behaviour has been thoroughly investigated [83, 84]. However, even after using severe post-treatment techniques such as annealing, electroforming, or plasmonic welding, the impact of junction resistances in NWNs can be a rather complex task to resolve [82, 83]. Figure 1.2 (a,b) display SEM images

of Ag nanowire junctions of a network before and after the mechanical pressing treatment [77] while (c,d) show TEM images of Ag nanowire junctions before and after junction plasmonic welding [78]. Regardless of the junction treatment, the contact point between each pair of nanowires will never offer "zero resistance" as porous interfaces between the wires and the presence of defects can still play a role in the wire-to-wire conduction process. Yet, experimental realizations of NWNs for applications in flexible transparent conductors are a broad topic that will be reviewed in the next section.

1.1.1 Transparent Conductors

Transparent conducting electrodes (TCEs) or simply transparent conductors (TCs) are materials that combine high electrical conduction and high optical transparency, primarily in the visible spectral range, which are typically trade-off physical properties [29, 55, 65, 66]. Flexible displays and touch screens [85], thin-film heaters [86], wearable sensors [87], neural interfaces [88], and solar cells [89] are some of the technologies in which TCEs have demonstrated notable operational efficiency. ITO has dominated the industry for decades due to its excellent transparency and conductivity [29, 66]. However, indium scarcity and the requirement for high-vacuum deposition and high-temperature annealing still keep the costs of ITO as TCEs relatively high. Furthermore, its intrinsic brittleness has limited its prospective applications in burgeoning optoelectronics, which necessitate not only excellent transparency and conductivity but also mechanical flexibility. Alternatives have lately been offered, including conducting polymers [76], carbon nanotubes [74], graphene [75], and metallic networks [66, 90]. Among them, unstable conducting polymers with low conductivity are still far from practical implementation [91]; carbon nanotubes are also not competitive due to high junction resistance and semiconducting properties [92]; and transparent graphene, despite its high mobility, cannot compete in conductivity with ITO due to its low carrier concentration and the costly large-area fabrication processes [93]. Metallic networks, particularly Ag NWNs, on the other hand, have become a well-known replacement for ITO due

to their outstanding optical transmittance, electrical and thermal conductivity as well as mechanical flexibility [94]. Figure 1.3 depicts SEM images of Ag random NWNs [94]. Other NWNs and array layouts made of other metals, e.g. Al, can be found in [95].

(a)   (b)
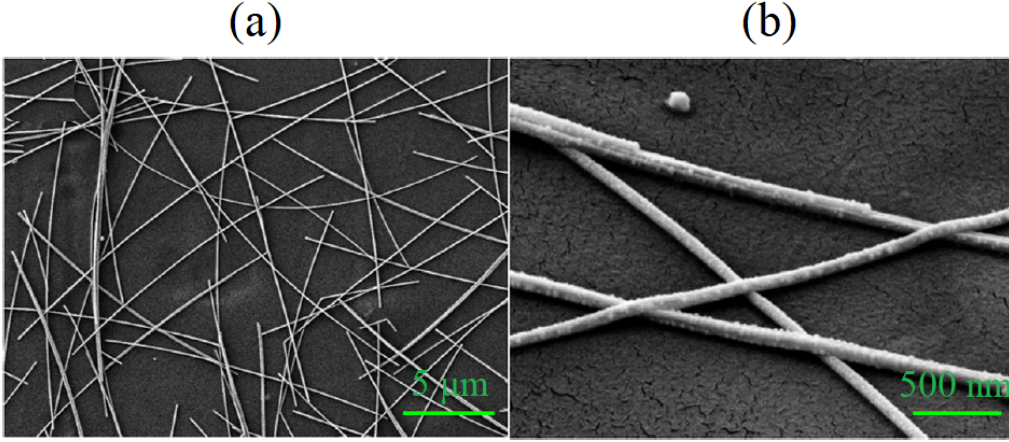
Figure 1.3: (a) SEM image of an Ag NWN. (b) High-magnification of an Ag NWN from panel (a). Images taken from [94].

1.1.2 Structural Properties of Nanowire Networks

The geometrical, physical, and intrinsic factors of the nanowire materials, as well as the device arrangement, have a significant impact on the performance of nanowire networks which includes the electrical and thermal conductivity, optical transmittance besides mechanical flexibility [29, 55, 56, 90]. A variety of control parameters affects these properties of such networks, including structural ones such as the nanowire aspect ratio (AR), defined as the nanowire length (L_w) divided by the nanowire diameter (d_w) or $AR_{\bigcirc} = L_w/d_w$ in which the subscript $\bigcirc$ indicates AR of cylindrical nanowires with a circular cross-sectional area. However, NWNs are not restricted to only cylindrical nanowires; they can be fabricated with other layouts and designs, e.g., seamless NWNs (pattern-based junctionless NWNs that will be discussed later in Chapter 4) are composed of nanowire segments or nanochannels with rectangular cross-sectional areas with AR defined as the width of the nanowire (W_w) divided by its depth (D_w), or $AR_{\blacksquare} = W_w/D_w$ in which the subscript $\blacksquare$ indicates AR of nanowires with

a rectangular/square cross-sectional area. The NWN density (n_w), defined as the number of nanowires per unit of area, the orientation of the nanowires with respect to a reference axis, the effects of nanowire curvature or wire persistence length, and the network area fraction (AF) [96–98] are also other parameters that can be tuned to control the electrical-optical-thermal properties of NWN systems. Not only the individual nanowires can be synthesized at different geometries, shapes, and sizes but also the layout of the network device can be constructed according to a variety of forms [99, 100]. Figure 1.4 depicts several NWN structures composed of diverse layouts and materials deposited on a substrate. This figure shows experimental and computer-generated images of distinct NWN layouts that inspired the work of this thesis. Figures 1.4 (a,b) depict a random NWN created by distributing Ag nanowires over a square surface without any particular constraint. The network is shown for both experimental SEM image [101] and a computer-generated model [97], respectively. Such NWNs are referred to as "standard" NWNs throughout this thesis. Random metallic NWNs are resistive arrays that exhibit equivalent or sheet resistance (R_s) that can be determined experimentally or by numerical methods. R_s is mostly dependent on the connectivity profile of the network, junction resistance values (R_{jxn}) originated from the multiple interwire connections, and the inner resistance of the nanowires themselves (R_{in}) [82, 102]. Figures 1.4 (c,d) display experimental [103] and computer-generated Ag NWN structure [97] with a different device layout; these networks are patterned with squared gaps forming small voids or "windows" with the intent of enhancing transparency features. These types of networks are called mesh or transparent grid design NWNs [103, 104]. A closer inspection of all NWN examples in this figure can already demonstrate that such systems are not entirely made of perfectly straight wires. Figures 1.4 (e,f) illustrate experimental SEM image [105] and computer-generated of combined straight and curved Ag nanowires [97] randomly deposited over a substrate area, respectively. These are referred to as "hybrid" NWNs throughout this thesis, indicating the fact that they are made of both straight and curved nanowires. We will discuss in detail the characterization and computational study done on the NWNs

depicted in Figures 1.4 (a-f) in Chapter 3. These are referred to as junction-based NWNs since electrical signals essentially flow from wire to wire through their contact points. Figures 1.4 (g,h) show an experimental SEM image of a silicon NWN [81] manufactured as a continuous nano-crack network alongside its computer-generated representation. The key difference between the network shown in Figures 1.4 (g,h) and the junction-based NWNs in Figures 1.4 (a-f) is that the nanowires in the former are seamlessly connected to each other, whereas in the latter, the nanowires are connected in such a way that they generate extra resistance at their junctions. This seamless connectivity in the network shown in Figures 1.4 (g,h) can potentially lead to improved electrical conductivity and performance compared to the standard NWNs. Figures 1.4 (g,h) are referred to as "seamless" NWNs throughout this thesis to remind the fact that they lack contact junctions at the nanowires intersections, and we will discuss more details about this type of network in Chapter 4.
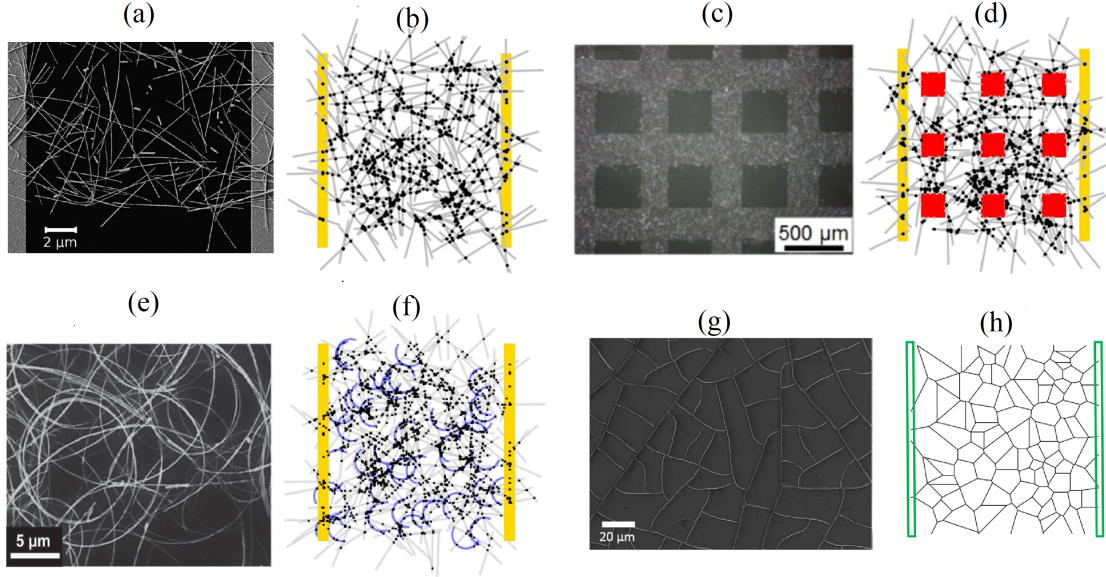
Figure 1.4: (a) Micrograph experimental image of a random (standard) Ag NWN [101] paired with a (b) computational representation of this type of NWN [97]. Panel (a): reproduced from Ref. [101] with permission from the PCCP Owner Societies. Panel (b): reproduced from Ref. [97] with permission from the Royal Society of Chemistry. (c) Micrograph experimental image of an Ag mesh-pattern NWN paired with a (d) computational representation of this type of NWN [97]. Panel (c): image reprinted (adapted) with permission from reference [103]. Copyright 2020 American Chemical Society. Panel (d): reproduced from Ref. [97] with permission from the Royal Society of Chemistry. (e) Micrograph experimental image of an Ag hybrid curved-straight NWN [105] paired with a (f) computational representation of this type of NWN [97]. Panel (f): reproduced from Ref. [97] with permission from the Royal Society of Chemistry. (g) Micrograph experimental image of a seamless silicon NWN from [81] paired with a (h) computational representation of this type of NWN. Panel (h): reproduced from Ref. [106] with permission from the Royal Society of Chemistry. In the computer-generated panels, different elements of the NWNs are colour-coded to aid in their identification. The junctions between two nanowires are represented by black circles, straight nanowires are depicted as grey sticks and curved ones are shown as blue semi-circles. Additionally, vertical yellow (or green) thick lines on each side of the network represent source and drain electrodes for electrical modelling.

Given the wide variety of tunable parameters, distinct NWN device layouts, and complex trade-off physical responses, the goal of this thesis is to develop a comprehensive computational framework that can shed light on the electrical-optical-thermal properties of disordered NWN systems that are prone to TCE applications. This computational framework has the purpose to inform on how typical trade-off quantities such as sheet resistance and optical transmission can be optimized with respect to the structural and intrinsic tunable param-

eters of distinct NWN layouts. In other words, we are able to establish tunable strategies for the parameters to decide for instance how much optical transmission one can trade for lower resistance values and vice-versa. The coupled thermal-electrical responses are also investigated and are contrasted in terms of the system's tunable parameters and its overall connectivity features. We built a modular computational framework that can navigate through four sub-modules addressing distinct responses and characterization schemes of disordered NWNs as shown in Figure 1.5. The sub-modules can conduct statistical ensemble analysis of numerous NWN samples as well as customized analysis of an individual NWN structure built with very specific settings. Before going into the physical responses (electrical, optical, and thermal), an in-depth spatial characterization of the NWN structure (or an ensemble of them) is conducted using in-house scripts which give information on the network connectivity, density, junction or intersection mappings, and nanowire characteristic length distributions if applicable. This stage is required so we can establish a relationship between the structural features of the NWNs with their physical responses. This structural mapping is hence fed into the "electrical", "optical", and "thermal" sub-modules equipped with distinct software to extract prominent physical responses from the NWNs including sheet resistance, optical transmission, current-flow and temperature distribution profiles. More details on each computational procedure will be given in the subsequent chapters but, to also enable the coupling of these sub-modules and their respective outcomes, one requires the use of a rich set of computational packages as the following: in-house scripts written in Python programming language, a Mie light scattering theory (MLST) [107] MATLAB packaged named MatScat written by [108, 109], and COMSOL Multiphysics® software [110], a multiphysics simulation package that allows users to simulate and analyze complex physical phenomena involving multiple physics schemes and with the aid of graphical user interface (GUI). This schematic summarizes the computational framework followed throughout this thesis; note that even though the scope of this thesis is purely computational, we always compared our numerical results with experimental findings by extensive literature search.

11
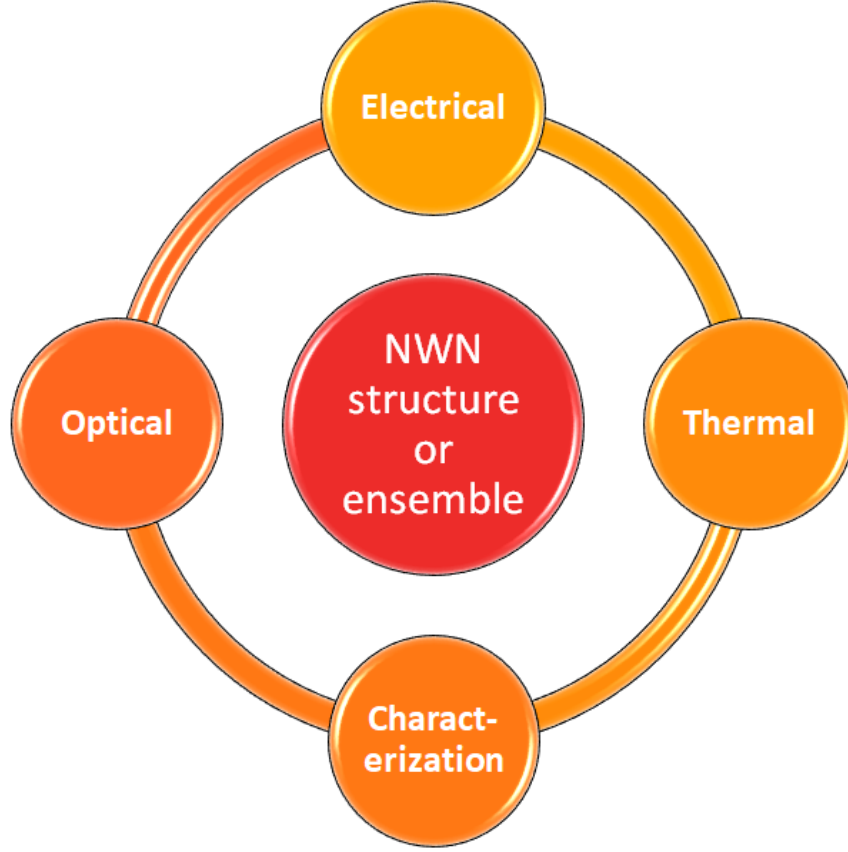
Figure 1.5: Schematics of the computational framework developed to study the thermo-electro-optical properties of disordered metallic NWNs in this work. To conduct a comprehensive analysis of NWNs, it is necessary to define several key parameters related to their structural design, such as aspect ratio, area fraction, nanowire density, angular orientation, curvature, device layout, and intrinsic material properties. This is included in the spatial "characterization" module. Once these parameters are established, the next steps involve the development of computational modules for electrical, optical, and thermal simulations, employing COMSOL Multiphysics® software [110] as well as in-house computational implementations to provide a thorough understanding of the behaviour of NWNs under various conditions. This whole framework is equipped to perform statistical studies in ensembles of NWNs or customized studies of individual NWN structures. Reproduced from Ref. [106] permission from the Royal Society of Chemistry.

1.1.3 Electrical and Optical Properties of Nanowire Networks

The electrical and optical properties of NWNs have been widely investigated over the past decade by theoretical and experimental efforts. Due to the disordered and percolative na-

ture of NWNs, it can be rather difficult to pinpoint a (R_s, T_{op}) pair for a given set of structural/intrinsic parameters with certainty. But most importantly, the electrodes that will probe the electrical response of the NWNs need to percolate, i.e., nanowires need to be dispersed in such a way that the electrodes are shortcut by them. Many experimental and computational studies devoted to determining the electro-optical properties of metallic NWNs which can be analyzed in terms of figures of merit (FOM) in which R_s and T_{op}, taken for distinct NWN devices, can be plotted as Cartesian axes to see how these quantities correlate in response to a spanning parameter phase space [98, 111]. Many works have pointed out that metal NWNs can exhibit low $R_s \leqslant 100 \,\Omega/\square$ (units of ohms per square) and high optical transparency $T_{op} \geq 90\%$ with regards to their chemical compositions, geometrical and physical properties of the nanowires as well as the device-architecture [29, 72, 96]. Bae et al. [111] highlighted that TCEs must have high optical transmittance, typically, $T_{op} \geq 90\%$, while the electrical R_s varies according to the device's operation and purpose. From touch screens and flexible displays to solar cells, these technologies typically function at resistance levels ranging from $500 \,\Omega/\square$ to lower as $1 \,\Omega/\square$ [111]. The latter discusses the typical sheet resistance ranges for various applications involving TCEs. For most industrial applications, TCEs may have a sheet resistance of less than $500 \,\Omega/\square$. Organic light-emitting diodes and solar cells, for instance, should have sheet resistances $< 50 \,\Omega/\square$, while touchscreens should have sheet resistances of $200 - 500 \,\Omega/\square$, according to industry standards [111]. Figure 1.6 shows a FOM collection for various transparent conductor devices made of distinct materials and layouts to also highlight the sheet resistance variance among the various applications and the desired high optical transmittance values ($> 90\%$) [98]. Still in terms of FOM, Figure 1.7 shows a comparison between the standard TCE ITO with other contemporary thin-film nanoscale materials and a schematics to illustrate the costs of fabricating some of these material groups with respect to their conductivity. These figures illustrate that the trade-off between high optical transmittance, low sheet resistance, and costs are significant aspects to be considered when choosing material alternatives for TCE applications [58, 112].
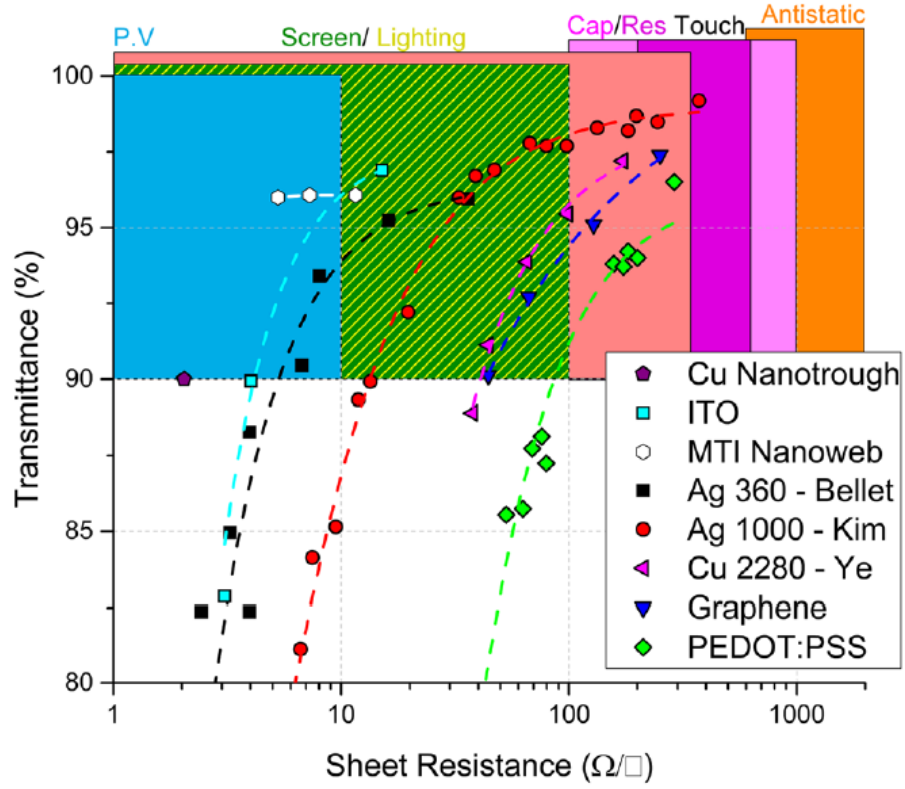
Figure 1.6: Relationship between sheet resistance and optical transmittance for various transparent conductor applications (photovoltaic (PV), screen/lighting, capacitive and resistive touch screens, and antistatic coatings) highlighted on the top part of the panel [98]. Legend distinguishes materials in their respective transparent conductor technologies. This data information was taken from the references [113] (Cu Nanotrough and ITO), [114] (MTI Nanoweb), [115] (Ag 360 - Bellet), [116] (Ag 1000 - Kim), [117] (Cu 2280 - Ye), [117, 118] (Graphene), and [119] (PEDOT:PSS).
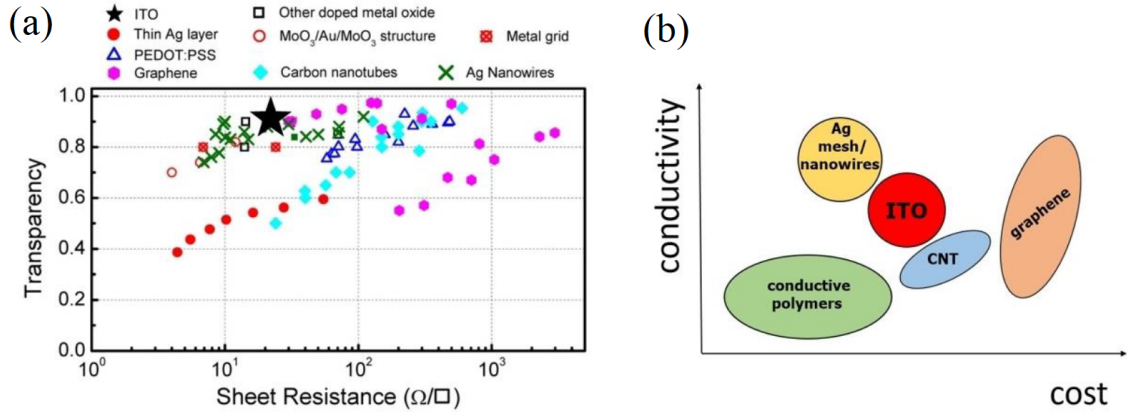
Figure 1.7: (a) FOM for several material groups. Reproduced by permission from [120]. (b) Schematics illustrating the costs in terms of the conductivity properties of each material group, including the standard ITO and Ag mesh/nanowires [112].

Many experimental works have effectively performed FOM trade-off analysis in NWN thin films, however, many questions remain unanswered and empirical examination can be costly and time-consuming [96]. Experimental sample sizes can be limited, undermining therefore a meaningful statistical analysis of the FOM and other physical properties such as spatial characterization of the NWN samples and their temperature distribution profiles. NWNs can also be described analytically; several research studies have attempted to find closed-form equations for estimating the sheet resistance and optical transmittance of 2D random percolating networks. Interestingly, there are analytical formulations of the effective sheet resistance and optical transmittance as a function of physical parameters which are worth understanding to elucidate typical trends between R_s and T_{op} [82, 101, 121, 122]. Nonetheless, there is not a universal or generalized closed-form expression ruling the correlation of R_s and T_{op}. Some of these analytical approaches are empirical or semi-empirical which require fitting with experimental data for very specific sample characteristics and conditions [123, 124]. One can utilize the following expression to predict the relationship between transmittance and sheet resistance of a material. This equation can be useful for designing and optimizing transparent conductive materials but its applicability should be carefully evaluated for each specific case [125, 126]:

$$T_{op} = \left[1 + \frac{188.5}{R_s} \times \frac{\sigma_{opt}}{\sigma_{cond}}\right]^{-2}.$$ (1.1)

In the above equation, σ_{cond} is the electrical conductivity of metal nanowires, and σ_{opt} is the optical conductivity related to the chemical compositions of the nanowires. Equation (1.1) establishes a phenomenological relation between T_{op} and R_s that emphasizes the trade-off aspect of these two quantities, and how they can relate with intrinsic quantities such as σ_{opt} and σ_{cond}. But this relation is also linked to other specifics associated with the NWN connectivity and device layout, turning it into a non-ubiquitous relation [123].

1.1.4 Thermal Properties of Nanowire Networks

Metallic nanowires' thermal characteristics include their thermal conductivity, temperature dependency of their electrical conductivity, and thermal stability [127–129]. There have been studies on how the thermal conductivity of metallic nanowires relates to their electrical conductivity. It has been found that the thermal (k_{cond}) and electrical (σ_{cond}) conductivities of metals are inextricably linked via the Wiedemann–Franz law [130] given by

$$\mathcal{L} = \left(\frac{k_{cond}}{\sigma_{cond}}\right)\frac{1}{T}$$ (1.2)

in which T is the temperature and $\mathcal{L}$ is the Lorenz number, typically $\mathcal{L} = 2.44 \times 10^{-8}$ WΩK^{-2} [131, 132]. It is important to note that the proportionality factor of the Wiedemann–Franz law can vary with respect to the material's characteristic sizes. For instance, the thermal conductivity of platinum (Pt) nanowires ($L_w \sim 10\,\mu$m and $d_w \sim 100$ nm) was recently compared to electrical conductivity measurements at ambient temperature. The electrical and thermal conductivity of the nanowire was reduced by a factor of 2.5 and 3.4, respectively, as compared to bulk data [132]. Thus, the Lorenz number of the nanowire was discovered to be lower than the bulk Lorenz number of metals, with a 25% difference [131, 132]. This drop is frequently linked to electron scattering at grain boundaries.

Grain boundaries are the borders between crystalline grains in a substance. As electrons travel through a material, they can confront grain boundaries, which can behave as impediments that scatter the electrons and restrict their mobility. This phenomenon is known as "electrons scattering at grain boundaries". In the context of nanowires, grain boundaries can have a substantial effect on the material's electrical, thermal, and mechanical characteristics. With nanowires, the size of the wire is comparable to the dimension of the grains, hence grain boundaries can have a greater impact on the behaviour of the material than in bulk structures. This could result in perturbations to the nanowire's thermal and electrical conductivities as well as their mechanical characteristics. Comprehending and controlling grain boundary behaviour is crucial to the development of high-performance nanowires for a variety of applications [133, 134].

Heat, oxygen, and moisture have all been shown to impact the thermal properties of individual metallic nanowires and NWNs which can lead to negative outcomes such as structural failures as a result of melting. Many efforts have been dedicated to probing their thermal applicability in electronic systems [127, 135]. For example, even though the melting point of Ag in its bulk form is extremely high (1173 K), multiple investigations have proven that when Ag nanowires are subjected to temperatures of 523 K or higher, they degrade into nanodots as a result of Rayleigh instability. Rayleigh instability is a phenomenon in which a thin structure fractures into small elements as a result of surface tension when its diameter gets ever so small that its surface energy surpasses its bulk energy. In a nanowire subjected to a high electrical potential, the electric field generates axial compression, degrading the nanowire's diameter. As the diameter grows too thin, the wire fragments into nanodots or smaller particles [136]. This can be even more of an issue when dealing with random metallic NWNs in which the electrical and heat fluxes in the network are not uniformly distributed across it [127, 137]. As another example, the breakdown of the Au NWNs at high current densities was investigated using infrared microscopy as shown in Figure 1.8 [129]. This technique is advantageous for discovering and identifying hotspots inside the network that

contribute to the network's failure. A further drawback of the random NWNs is that the contact area between the nanowires is extremely small, in the range of a few tens of nanometers, i.e., not conducive to efficient thermal diffusion [138]. Because of this, it is necessary to measure and evaluate the localized electrical and thermal dynamic behaviour in individual nanowires during the device operation if one wants to have a detailed understanding of the thermal mechanisms involved in the disordered nanowire mesh [139]. Several papers on the thermal phenomena of metal NWNs have been published employing experimental techniques such as electrical mapping [140] and thermoreflectance [141], but sufficient thermal/spatial resolution can be a challenge to achieve in such experiments. This is where computational simulations can be of aid as those conducted in this thesis and inspired by computational efforts such as in [128]. Because it is extremely hard to monitor the electrical current and thermal profiles experimentally at each nanowire, we dedicated to investigating not only the optical and electrical responses of disordered NWNs but also their thermal properties; this was done with multiphysics simulation packages [110] that can provide high-resolution thermal/spatial profiles and allow us to set realistic materials' settings and conditions.
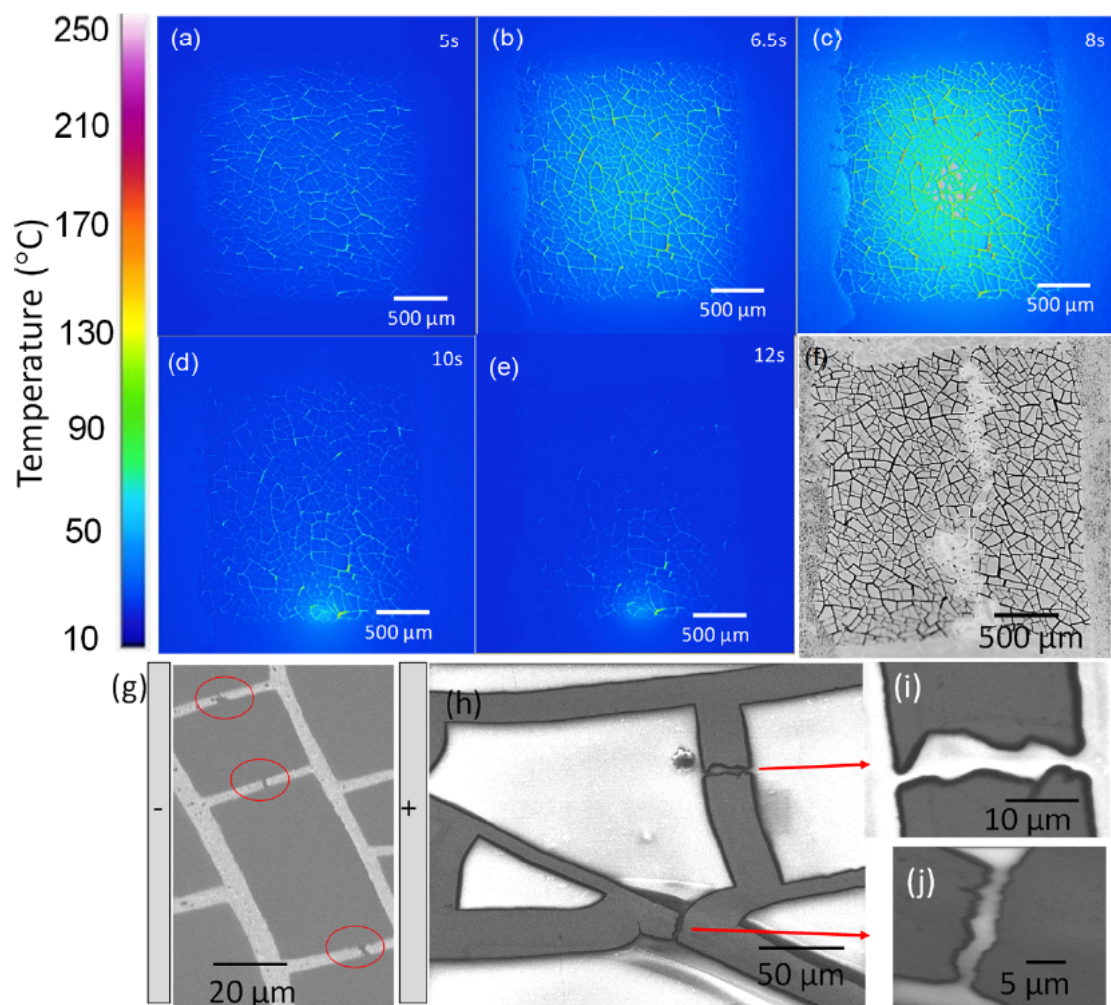
Figure 1.8: (a-e) A series of thermal photos taken at various points in time demonstrating the disintegration of the Au NWN on PET (polyethylene terephthalate) at 1.3 V. The temperature of the Au NWN grows with time, resulting in hotspots and eventually the network's failure. In panel (c), the grey portions around the heater's centre indicate picture saturation and correspond to the heater network's hottest places. (f) Infrared radiance image of an unpowered network following a breakdown, highlighting the damaged wires in the bright zone in the network's core. (g) SEM images of the network from the locations of breakdown (highlighted by the red circles). (h-j) Optical images at high magnification illustrating the breakdown areas. Image Reprinted (adapted) with permission from [129]. Copyright 2017 American Chemical Society.

1.2 Thesis Outline and Objectives

This thesis comprises five chapters, including this introduction. Our main goal is to provide a comprehensive study, by means of computational tools, that can inform on the electro-optical-thermal properties of TCEs made of random NWNs. Such physical properties often relate in a trade-off manner in which one can be improved at the expense of the other and vice-versa. For this reason, we devised a computational framework that can quantify how much gain/loss seemingly competitive physical responses in NWN systems impart on each other. In the following chapters, we will highlight the main computational tools and methods used to address the research goal elucidated above. Computational and theoretical descriptions such as the ones we worked with are very important because they allow making predictions about the electro-optical-thermal responses of highly disordered nanostructures such as the NWNs studied in this thesis and help us understand the main physical mechanisms ruling the intensity of such responses. NWNs as TCEs need to offer optimum transparency, tunable sheet resistance, and thermal stability, and these properties were covered in this work. Mechanical durability is also an important quality for next-generation flexible display technologies, however, we did not have time to explore this last property. The computational study of the mechanical properties of TCE NWNs will be discussed in Chapter 5 as an outlook for future work leading from this thesis. Overall, all these qualities (electro-optical-thermal-mechanical) are controlled by the network's underlying charge-carrier dynamics and geometric properties, which have been emphasised by several publications in the literature, many of which have been undertaken by our group and collaborators at Trinity College Dublin [98, 101, 142–144]. Particularly, my most recent contributions to the field resulting from this thesis can be found in [97, 106, 145].

Chapter 2 lays down the theoretical foundation and mathematical background that will be used throughout this thesis. We describe in detail the theories and models behind the computational toolkit we developed during this PhD experience. Some of the concepts are but not limited to: percolation theory, graph/network characterization, Mie light scattering

theory, Kirchhoff's circuit laws, conduction properties of nanomaterials, and resistive network theory. Chapter 3 covers the computational framework and its algorithms that model the electro-optical specifications of two distinct NWN layouts: the (standard) random NWNs and NWNs patterned by a transparent mesh to enhance transparency [97]. Aluminium, gold, copper, and silver nanowires are the materials of choice for transparent conducting electrodes in this study. We have investigated a diverse range of tunable parameters, including the network area fraction (AF), length-to-diameter aspect ratio (AR), and the angular orientations of the nanowires. Aside from that, the optical extinction efficiency coefficients of each material were predicted using two different approaches: Mie light scattering theory implemented in MatScat package developed by Schäfer [108, 109] and the finite element method (FEM) incorporated in COMSOL Multiphysics® simulation software. We were able to calculate and compare distinct FOM to establish the main trade-offs related to enhancing optical transmittance with the expense of reducing conductance and vice-versa. This study provided valuable insights into the design of next-generation TCE devices which are NWN-based [97].

Chapter 4 expands on what was developed in Chapter 3, albeit with a shift in focus towards the investigation of thermo-electro-optical properties of the so-called seamless NWNs. The latter is a nanostructure comprising nanowires devoid of any interwire contact junctions, thereby exhibiting a continuous and uninterrupted network configuration. The absence of junctions endows the NWN with distinct characteristics, such as elevated conductivity and surface area-to-volume ratios, rendering it an auspicious contender for a broad spectrum of applications in nanotechnology. Employing in-house computational methods and coupled electro-thermal models developed in COMSOL Multiphysics® software [110], we have carried out an in-depth computational work to examine the thermo-electro-optical properties of seamless NWNs and how they relate with their geometrical characteristics. Combining Ohm's law and Kirchhoff's circuit laws, sheet resistance estimates for random seamless NWNs were conducted and contrasted to those derived using COMSOL Multiphysics® software [110]. In this study, aluminium, gold, copper, and silver nanowires were used to evaluate

the transparent and electrical conduction performance of the systems as well as how they respond thermally [106]. Chapter 5 contains the conclusions of this thesis and also presents an outlook for future work.

This study presents significant contributions to the topic of computational modelling of transparent conductors utilizing NWNs, which are highlighted by the following key deliveries:

- Consolidation of a robust computational framework applicable to seamless and junction-based metallic NWNs at microscale dimensions that provide a systematic figure of merit analysis of optical transmission versus sheet resistance plus insights on their coupled electro-thermal properties.

- Comprehensive examination of various geometrical factors and their influence on the disordered NWNs ultimate performance and responses. This study considers the tuning of geometrical/spatial parameters such as area fraction, aspect ratio, network density, angular distribution constraints, grid-pattern layout, and variation in nanowire dimensions and curvature. NWNs of distinct material composition were also studied; we focused on metallic nanowires made of Ag, Al, Au, and Cu so we can contrast in quantitative terms their intrinsic material features. For example, the optical extinction efficiency factors of Ag, Al, Au, and Cu were calculated for two prevalent nanowire geometries, namely circular and square cross-sectional areas. The spectral data encompassing a broad wavelength range from 200 nm to 1200 nm has been examined, and are validated by Mie light scattering theory.

- The present study has also examined hybrid network architectures made of a mixture of straight and curved nanowires to reflect more realistic NWN scenarios since not all nanowires are perfectly straight; they can exhibit curvature, kinks, and mechanical distortions. Such curvature-related defects are known to increase the overall resistance of the network with the advantage of reducing its coverage area fraction. Such reduction favours the optical transmission of the NWNs. We quantified this trade-off in hybrid

NWNs composed of distinct concentrations of straight and curved nanowires. The latter was modelled as semi-circles so that we can control their arc length and radius.

- Contribution to the bulk of knowledge related to electro-thermal conduction transport at diffusive regimes of disordered interconnected nanomaterials under external stimuli or distinct operational conditions. This is particularly relevant due to the frequent occurrence of current density aggregation at specific locations in the network material, resulting in the formation of localized hotspots with elevated currents/temperatures that may damage individual nanowires locally. This phenomenon can cause breakdowns in the network and lead to excessive average temperatures and sufficiently high sheet resistance.

- Some of the collective features of many-body systems such as NWNs can be understood in terms of probability distributions that can be described by means of probability density functions fitting those distributions. In particular, previous works have demonstrated that the Weibull probability density function can envelop temperature distributions in junction-based NWNs [141, 146]. Our study demonstrates that the Weibull probability density function also describes temperature distributions in seamless NWNs, suggesting that Weibull may be characteristic of the thermal properties of random NWNs comprised of disordered resistor networks set at certain physical conditions.

- In addition to figures of merit, electromagnetic emissions generated by device components at high frequencies, e.g. radio frequency (RF), are also an important factor in transparent conductors since excessive emissions can not only cause device malfunction and shorten its operational lifetime but can also affect human health. We performed an analysis of the electromagnetic interference shielding effectiveness (EMI SE) in NWNs from a model [147–150] that relates the sheet resistance with the EMI SE performance of the NWN. As a result, we were able to quantify EMI SE from the

electrical properties of NWN films to estimate their specific electromagnetic emissions.

It is important to note that the focus of my PhD work was on the study of NWNs in the context of TCEs resulting in the main articles in [97, 106]. However, right at the start of this PhD experience, I did have the opportunity to participate as co-author in the study "Nonlinear ion drift-diffusion memristance description of TiO_2 RRAM devices" [145]. The purpose of my participation in that work was to give me an introduction to computational programming and to get acquainted with some of the in-house codes describing conduction mechanisms in individual nanowires. Computational physics was not part of my background prior to this PhD experience, nonetheless, this initial collaboration enabled me a hands-on approach to some of the computational tools relevant to what became the main topic of this thesis which is the study of electrical-optical-thermal properties of TCE NWNs. A practical exercise to get acquainted with computational numerical methods is to solve ordinary differential equations (ODE) that model a certain physical phenomenon. In that work [145], I was able to test how well a set of ODEs fitted experimental current-voltage hysteresis obtained for single nanowires made of Au–Ti/TiO_2/Ti–Au exhibiting intriguing resistive-switching features prone for use in Resistive Random Access Memory (RRAM) technologies. The current-voltage characteristics of these nanowires are rich in terms of physical mechanisms competing including Schottky barrier, quantum tunnelling, ionic drift/diffusion, and negative differential resistance (NDR) behaviour. A complex set of nonlinear ODEs was adapted to capture all stages and dynamical features outlined by the experimental current-voltage characteristics obtained by our collaborators at Trinity College Dublin [145]. Once this introductory computational work was completed for my learning, we established the current line of research aiming at the computational description of TCE NWNs as outlined in the chapters of this thesis.

Chapter 2

Theoretical Background and Methodology

2.1 Percolation Theory

In the context of NWNs, the term "percolative NWN" refers to a network of nanowires that are randomly oriented and interconnected in such a manner as to enable the transport of electrical current across the network. The fact that there is a threshold density of nanowires beyond which the network turns conductive and below which it continues to be insulating is one of the most important characteristics of such a network. Percolation theory [151–153], which explains the critical behaviour of systems formed of randomly dispersed/positioned elements that are connected, can describe this threshold behaviour. The application of percolation theory to our work could be illustrated by Figure 2.1. The computer-generated disordered NWNs sandwiched between source/drain electrodes are depicted in Figure 2.1 (a-c). Panel (a) exhibits a lack of enough nanowire density, below the critical threshold density, while panels (b,c) have high nanowire densities above the threshold critical density. This results in panel (a) being unable to facilitate current flow through the network, whereas panels (b,c) enable current flow between the source and drain electrodes. It is important

to note that changes in the network structure can alter the current flow path, as shown in panels (b,c), where the least resistive path is altered (represented by the connected black stick nanowires). Panel (b) depicts a standard disordered NWN, while panel (c) shows the same NWN with a grid-pattern window architecture.
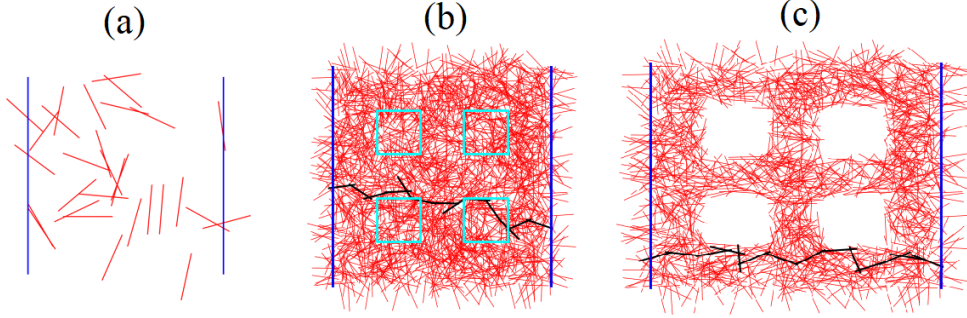
Figure 2.1: (a-c) Computer-generated random NWNs in two phases (percolative and non-percolative). The two vertical blue lines represent source/drain electrodes. The black connected sticks show the least resistive path through which current can flow through stick nanowires between source/drain electrodes. Nanowires are displayed by red lines. (a) A non-percolative random NWN with insufficient nanowire density so that electrodes are not bridged. (b) Standard random NWN with enough density (3.2 nanowires per μm^2) to percolate. The four cyan windows only serve to mark locations in which an alteration is going to be made in the NWN structure as depicted on panel (c). (c) Same NWN structure shown in panel (b) with grid-pattern design (2.3 nanowires per μm^2).

Percolation, in the broad context of condensed matter physics, can be defined as the process by which paths through a porous material are formed or connected; it can refer to any type of information that may be deemed to travel through a system that displays a collection of open and closed channels [153]. Everyday life is filled with simple instances of percolation, the most prominent being the percolation of water through ground coffee beans to provide that wonderful caffeine boost that appears to drive our contemporary world. The phenomenon of percolation has been used in a wide variety of fields, including but not limited to physics [153], petroleum [154], ecology [155], and material science [156], to name just a few. Percolation theory investigates how elements in a particular system are related to one another and their behaviours when clustered together. These elements may be linked to one another in a number of different ways, and the connections between them can

be interpreted as either open or closed routes. Studying a percolating system is primarily concerned with determining the density of open paths at which a phase transition occurs in one or more system characteristics. An important feature of transitions in percolating media is that they are often linked with the production of an overlaid cluster that spans the system. The critical density n_c at which this happens is being sought in the investigation of percolating systems [123]. In the context of the NWN spanning electrodes, this quantity can be defined as the critical nanowire density at which source and drain electrodes are connected by nanowires randomly spread in between and this can be obtained numerically, typically via Monte Carlo simulations in stick percolation systems as will be discussed later. Before addressing percolation concepts in the context of NWN TCEs, it is important to provide a few definitions and nomenclature related types of percolation commonly studied in physical systems [153]:

- Site percolation: open or closed pathways are constrained to a regular lattice of sites in these systems. If two sites share one side of the designated lattice, they are considered linked. A site is either open and empty or closed and inhabited under this approach.

- Bond percolation: the sides of the unit cell are either open or closed, and the lattice sides are considered bonds. If the lattice vertices share a closed bond, they become sites and are considered linked.

- Discrete percolation: systems that include a regular lattice of points where each point has a chance of being either occupied or unoccupied. Connected or nearby occupied points create clusters, and when the frequency of occupancy rises, clusters combine to produce bigger clusters so that the system can ultimately percolate.

- Continuum percolation: systems in which no discretization of the sites is conducted; sites or objects are dispersed randomly in these systems and are deemed to be related if the basis touches or overlaps. NWNs fall in this percolation category.

A system must have at least one cluster that meets the system's percolation requirements for it to be percolating. Figure 2.2 provides graphical representations of bond and site percolations on a discrete square lattice, respectively. This exemplifies a case of discrete percolation in which the spatial domain is regular and periodic, outlining a square lattice mesh. An extensive study on 2D continuum percolation of randomly distributed objects of different shapes (circles, sticks, and squares) was done by [157]. The 2D random stick percolation problem is a continuum percolation case we use to represent graphically a real NWN system. The boundaries of our system are specified by the electrodes that will interrogate the NWN electrically. In this way, one can define the density percolation threshold as the lowest concentration of nanowires that percolate the electrodes to produce electrical conduction through the network frame. If electrodes are not percolated, no conduction occurs as it is assumed that the NWN is deposited over an insulating substrate. A randomly generated NWN is made of nanowires that have the same likelihood of landing anywhere on the substrate and their orientation with respect to a reference axis is also selected randomly. Pike and Seager [151] utilized percolation theory and simulations to demonstrate that the critical density of randomly oriented 2D sticks (n_c) could be estimated using the following expression [151]

$$n_c L_w^2 = Q_c \tag{2.1}$$

in which L_w is the length of the sticks (considering all the same) and Q_c is a constant that can be determined numerically; in the case of random stick percolation, it was found that $Q_c \approx 5.7$ [151]. It is worth mentioning that the criteria for a connection to occur between two sticks is that their centres should be within L_w of one another and that their relative orientations be such that they intersect. NWNs in which the nanowire density is $n_w \ll n_c$ are likely not electrically active and thus inappropriate for use in TCE applications [99,124,151]. However, if $n_w \gg n_c$, the NWN is most likely electrically bridged, however, a trade-off effect starts to emerge in which denser NWNs can be good for electrical conduction but not for optical transparency. As denser the NWN is, more light will be obstructed, limiting its

28

performance in terms of transparency.
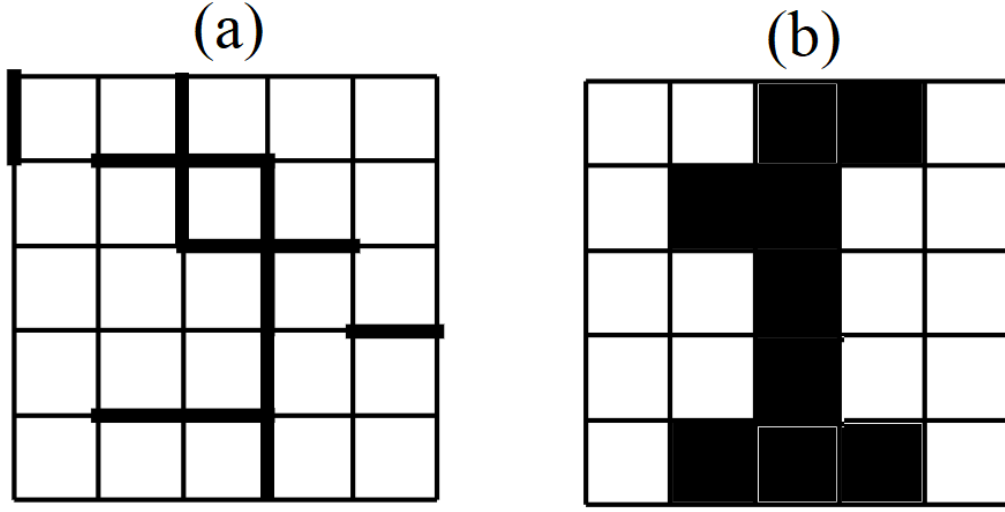
Figure 2.2: Representation of (a) bond percolation and (b) site percolation. On both panels, two boundaries of the lattice (top and bottom) are spanned (or percolated) by (a) bonds represented by bold edges and (b) sites represented by black squares.

The underlying basis of the electrical characteristics of 2D NWNs is a percolation process applied to a resistive circuit network. The conductance of the network is governed by the number and length of the network's electrical channels. These channels are produced by the interconnection of sticks across the network and often have a complicated geometry of parallel and series resistances. The most extensively and effectively utilized techniques for investigating percolation behaviours in the 2D random sticks (with resistive properties) are based on Monte Carlo schemes [152]. These investigations focus on statistical percolation, in which sticks are dispersed randomly on a surface and create percolating routes as their density rises. This also enables ensemble treatment in which averages and standard deviations of the relevant physical quantities can be obtained by generating multiple configurational NWN samples. Many of our findings and results require a robust statistical treatment in which ensembles made of multiple NWN samples are computer-generated in a controllable fashion, e.g., many of our analyses require ensembles of NWNs of fixed densities in which the spatial

arrangement of the nanowires is simply shuffled, but keeping n_w at a fixed value.

2.2 Electrical Modeling of Random Nanowire Networks

For a network with random connectivity, a more generalized method based on graph and Kirchhoff's circuit laws is more suitable to extract the electrical properties of a resistive network such as our NWNs. The illustration of the method in this section is based on the materials contained in O'Callaghan's thesis [82] that served as base literature for my studies. The simplest picture is to represent the NWN as a mathematical graph in which the nanowires are treated as equipotential nodes and their pair-wise connections are resistive edges. Therefore, a NWN containing $\mathcal{N}$ wires can be mapped into a graph of $\mathcal{N}_w$ nodes with E_w edges labelled as $E_w \equiv (i, j)$ if wires i and j are connected. The edges represent conductive connections with an associated conductance value of g_{ij}. Figure 2.3 shows a graph example with $\mathcal{N}_w = 5$ and $E_w = 6$ (represented by the line segments and with their respective conductance values, g_{ij}). This graph is identified as a weighted graph with conductances used as weights for the edges [82, 158] and the nodes labelled by integer numbers are nanowires. I will use this graph to illustrate the construction of the Kirchhoff resistive matrix that can be used to solve the Kirchhoff circuit equations considering the presence of a current source. This scheme was coded in a programming script written in Python language [159] to characterize NWNs electrically.
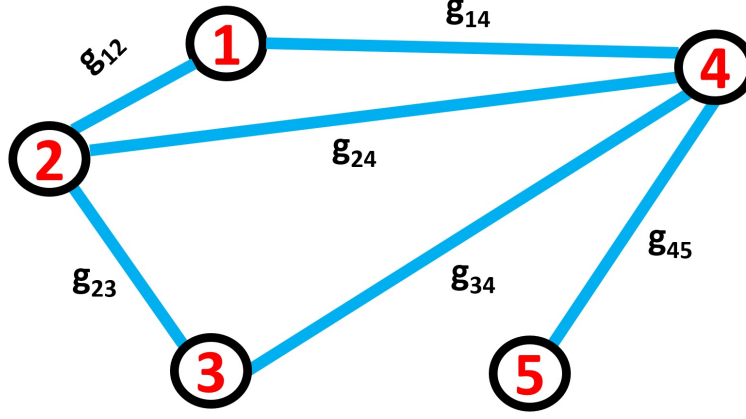
Figure 2.3: A graph example containing $\mathcal{N}_w$ = 5 nodes (circles) and E_w = 6 edges (line segments). Each edge has a weight given by a conductance value g_{ij} being (i,j) a pair of linked index nodes. Here, the subscript "w" stands for "wire".

The connectivity of a (weighted) graph can be described by the so-called Adjacency matrix, $\hat{A}$, which stores the information of the nearest connected neighbours of each node. If nodes i and j $(i \neq j)$ are connected, then the off-diagonal elements of this matrix are given by g_{ij} and zero otherwise. The (weighted) degree of each node d_i can be stored in the so-called Degree matrix, $\hat{D}$, a diagonal matrix whose non-zero elements are given by [160–162]

$$d_i = \sum_{j=1}^{\mathcal{N}_w} A_{ij} \tag{2.2}$$

where A_{ij} are the Adjacency matrix elements. The Laplacian matrix of the graph, $\hat{L}$, can be obtained by subtracting these two matrices as $\hat{L} = \hat{D} - \hat{A}$. For example, for the graph in Figure 2.3, these three matrices are given by

$$\hat{A} = \begin{pmatrix} 0 & g_{12} & 0 & g_{14} & 0 \\ g_{12} & 0 & g_{23} & g_{24} & 0 \\ 0 & g_{23} & 0 & g_{34} & 0 \\ g_{14} & g_{24} & g_{34} & 0 & g_{45} \\ 0 & 0 & 0 & g_{45} & 0 \end{pmatrix},$$

$$\hat{D} = \begin{pmatrix} d_1 & & & & \\ & d_2 & & \huge 0 & \\ & & d_3 & & \\ & \huge 0 & & d_4 & \\ & & & & d_5 \end{pmatrix}, \quad (2.3)$$

$$\hat{L} = \hat{D} - \hat{A} = \begin{pmatrix} d_1 & -g_{12} & 0 & -g_{14} & 0 \\ -g_{12} & d_2 & -g_{23} & -g_{24} & 0 \\ 0 & -g_{23} & d_3 & -g_{34} & 0 \\ -g_{14} & -g_{24} & -g_{34} & d_4 & -g_{45} \\ 0 & 0 & 0 & -g_{45} & d_5 \end{pmatrix}.$$

This weighted Laplacian matrix is also known as the Kirchhoff matrix or conductance matrix because it is a matrix carrying conductance information. In a conductor, Ohm's law is given by $G\,\Delta V = I$ where G is the conductance, ΔV is the voltage drop, and I is the current. The resistance is simply $R = 1/G$. For a circuit network with multiple voltage nodes and conductors as in the graph of Figure 2.3, Ohm's law can be written in matrix form as

$$\hat{G}\vec{V} = \vec{I} \quad (2.4)$$

in which $\hat{G} \equiv \hat{L}$, $\vec{V}$ is a voltage vector containing the voltages at each node and $\vec{I}$ is the current vector whose elements are non-zero only at the nodal sources and sinks. Applying

Kirchhoff's current law in which the sum of currents flowing in and out of a circuit node is conserved, it is possible to make the equivalence

$$
\begin{aligned}
d_1 &= g_{12} + g_{14} \\
d_2 &= g_{12} + g_{23} + g_{24} \\
d_3 &= g_{23} + g_{34} \\
d_4 &= g_{14} + g_{24} + g_{34} + g_{45} \\
d_5 &= g_{45}
\end{aligned}
\tag{2.5}
$$

in which d_i in the equations above are identified as weighted degrees. The equivalences above should serve to guarantee that the Kirchhoff's voltage law stating that the sum of the voltage differences around any closed loop in a circuit must be zero will be respected when we write the system of linear circuit equations embedded in Equation (2.4). Let's assume that a pair of nodes m and n can act as source and drain of current, respectively. This means one can inject an amount of current i_0 at node m and extract it at node n. The elements of the current vector can then be written as $I_j = i_0(\delta_{jm} - \delta_{jn})$ where $j = 1, ..., \mathcal{N}_w$ and δ is the Kronecker Delta. Source and sink nodes are used to simulate the presence of electrodes that will perturb and probe the electrical properties of the circuit network. Equation (2.4) can now be solved for $\vec{V}$ using a numerical library that solves a system of linear equations of the type $\hat{L}\vec{x} = \vec{b}$ where $\hat{L}$ is a symmetric matrix, $\vec{b}$ is a given vector, and $\vec{x}$ is a vector with unknowns. From the solution of $\vec{V}$, the equivalent resistance (R_{eq}) taken between two reference nodes (m, n) can be calculated as

$$
(R_{eq})_{mn} = \frac{|V_m - V_n|}{i_0}.
\tag{2.6}
$$

For example, consider the graph in Figure 2.3 with $i_0 = 1$ A and $g_{ij} = 1$ S $\forall\ (i, j)$ pair, by constructing its associated Laplacian matrix and solving the system of linear circuit equations

with two particular configurations of current sources, we obtained an equivalent resistance of $(R_{eq})_{15} = (R_{eq})_{35} = 1.625\ \Omega$. This framework for computing equivalent resistances and other electrical properties in resistive NWNs is a subset of a more generalized algorithm named Modified Nodal Analysis (MNA) [161] which provides a recipe to extract electrical quantities out of complex circuits that can be made of multiple current/voltage sources, resistors, capacitors, and inductors. Due to the simplicity of our device setup (a two-terminal resistive NWN), we do not need to code all circuit modalities and conditions required for the generalized MNA method, as a result, we implemented the simple matrix scheme elucidated in this section.

2.2.1   Computational Methods for Random Nanowire Networks

The resistance of a NWN is dependent on a variety of key parameters, including length and diameter of the nanowires, interwire junction resistances (R_{jxn}), nanowire inner resistance (R_{in}), nanowire or network density (n_w), connectivity profile, device dimensions, to mention a few [29, 66, 82, 84, 97, 98, 144, 163]. An effective method for addressing this complicated parameter phase space is to use computers and to map the NWN onto a node-voltage analysis in which each nanowire is a node and is linked to its closest neighbours with a resistor modelling the electrical properties of the interwire junction. If a nanowire is mapped as an equipotential node, we can say that a simplification is being made in the model because one loses information related to the inner wire resistance; this equipotential nodal representation does not enable a resolution to distinguish nodes within the same nanowire that would be modelled by R_{in}. Within this approximation, an assumption can be made that states that the junction resistance R_{jxn} is substantially larger than the nanowire inner resistance R_{in} and so dominates the network's electrical performance. This methodology has been known as the Junction Dominated Assumption (JDA) [144]. According to Monte Carlo simulations, the conduction profile in conductive stick networks is particularly sensitive to the ratio R_{in}/R_{jxn} [82, 164]. The resistive behaviour of carbon nanotube networks has been

effectively estimated utilizing JDA because the resistance of individual nanotubes is very low in comparison to the resistance of a junction formed by two nanotubes [83]. Metallic nanowire junctions, on the other hand, have been revealed to have relatively lower junction resistances, and as a consequence, the nanowires themselves have a considerable effect on the network conductivity [78]. In the following, a model is presented that accounts for both of the nanowire resistances (R_{in} and R_{jxn}) referred to as the Multi-Nodal Representation (MNR). We debate how MNR and JDA are affected in distinct ways by the underlying parameters that were discussed at the beginning of this section. To compute the sheet resistance of a NWN, the nanowire mesh must be converted into a mathematical graph that reflects the connectivity information of the network to which node-voltage points are allocated. Thus, Kirchhoff's system of linear equations can be constructed. Each wire in the JDA mapping is represented by a common-voltage circuit node coupled to other wires by junction resistors. A NWN with N_w wires can produce an N_w-node resistive graph. An off-diagonal component of the Kirchhoff matrix is an interwire junction conductance between wires i and j. Figure 2.4 (a) shows a diagram of a basic NWN (top) and its JDA visual presentation (bottom) [144]. This graphical depiction has three nodes, one per nanowire, and two interwire junctions with resistance R_{jxn}. Because there is no contact between wires W1 and W2, there is no resistance in the graph presentation for this connection. Within the JDA, the placements of the nanowires are arbitrary; only the network's connectivity profile and R_{jxn} values dictate its electrical characteristics. Because this mapping only affects interwire connection, the inner wire resistances R_{in} of the nanowire segments are not accounted for in this model [142, 144].
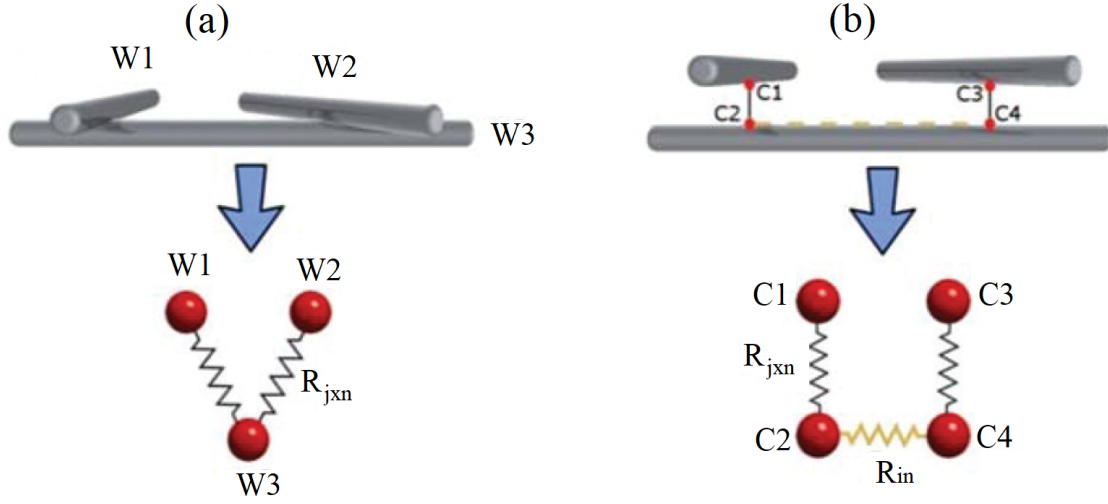
Figure 2.4: (a) (Junction Dominated Approximation - JDA) NWN schematic with three wires labelled as W1, W2, and W3 and two interwire junctions (by contact), one between wires (W1,W3) and the other between wires (W2,W3) [144]. A circuit representation of the NWN is shown underneath the drawing; there are three equipotential nodes consisting of three wires and two interwire junction resistors represented by black resistor symbols with resistances R_{jxn}. (b) (Multi-Nodal Representation - MNR) A detailed look at the three wires depicted in panel (a) [144]. The four connecting nodes are represented by the red dots designated C1, C2, C3, and C4. The NWN is represented by a MNR circuit underneath the sketch. Connection (voltage) nodes belonging to the same junction are indicated in black and connected by a junction resistor R_{jxn}. The neighbouring connection nodes on W3, C2 and C4, are linked by a nanowire segment resistor R_{in}, shown by a yellow resistor symbol. Reproduced from Ref. [144] with permission from the Royal Society of Chemistry.

Although JDA appears to work well for materials that have reasonably high junction resistances, discarding the nanowire resistance is not an ideal solution for materials in which the nanowire resistance is comparable to the resistance of the junctions. Integrating the inner wire resistance contribution to the model via MNR as described earlier results in an increase in the level of complexity of the simulations. The MNR description takes into consideration the finite material resistance of the wires as shown in Figure 2.4 (b), which not only makes the model more robust and flexible but also enables it to explain a greater variety of wire systems with distinctively different material properties [82, 96, 144]. Figure 2.4 (b) depicts a NWN motif with its corresponding MNR graph representation [144]. In this architecture, the total number of nodes is $2N_j$, wherein N_j is the total number of junctions in the system. The

inner wire resistor between nodes C2 and C4 is coloured yellow, whereas the two junction resistors (C1,C2) and (C3,C4) are coloured black. It is also worth noting that contributions from the wires' dead ends are not reflected in this picture. Unlike the JDA, MNR requires the positions of the wires and their respective intersections in the system to be considered because the lengths between adjacent connection nodes are crucial for the computation of nanowire inner resistances. Due to the usage of a large number of voltage nodes to split the wires, this technique needs a considerable amount of computing resources; memory and processing demands are substantially greater depending on the size of the NWN to be studied. Besides computation/numerical methods, analytical descriptions based on effective medium theory (EMT) were also attempted to minimize dependency on computing power [101] to relate the sheet resistance of the network with a multitude of characteristic parameters such as the wire density, R_{jxn}, the nanowire resistivity (ρ), the electrode size and separation. The support of closed-form analytical expressions helps to reduce the amount of memory and time that is used for numerical computation, but with the expense that some physical considerations are treated only 'effectively'. In this thesis, we will prioritize the complete MNR description in which all nanowire segments and material specifications are fully considered in the model since we aim at a computational description for quantitative prediction rather than just qualitative.

2.3   Characterization of Random Nanowire Networks

Before conducting any electrical, optical, or thermal assessment on the NWNs, we need to perform a spatial characterization of their network structure so this information can be related to the physical responses that we are going to study. All NWN samples studied in this thesis are computer-generated; some of their spatial features can be set during their digital generation, and some can be quantified or processed after the NWN structure has been generated. The computational aspect of this work gives us freedom to generate NWN

structures with different levels of complexity, e.g., a widely adopted simplification is to generate random NWNs considering that the lengths of all wires are the same. However, the length of actual nanowires manufactured experimentally is never precisely the same [82,102]. As such, we can generate random NWNs composed of nanowires of distinct lengths built from a distribution of lengths. A common nanowire length distribution provided by our experimental collaborators in Trinity College Dublin is to consider that L_w is Gaussian distributed. For instance, many of their Ag nanowire sample batches exhibit $\langle L_w \rangle$ = 7 μm Gaussian distributed with a dispersion of σ_{std} = 1.8 μm [82, 102, 144]. As a result, we have the possibility of computer-generating NWNs made of nanowires of distinct lengths and diameters as well that can be picked from a pre-defined probability distribution. This is exemplified in Figure 2.5 which shows on panel (a) a computer-generated NWN with all interwire connections already detected (black circles) and vertical wire segments (in blue) that will act as electrodes. That NWN does not have all nanowires with the exact same length, they were sorted from a dispersed nanowire length distribution as shown on panel (b).
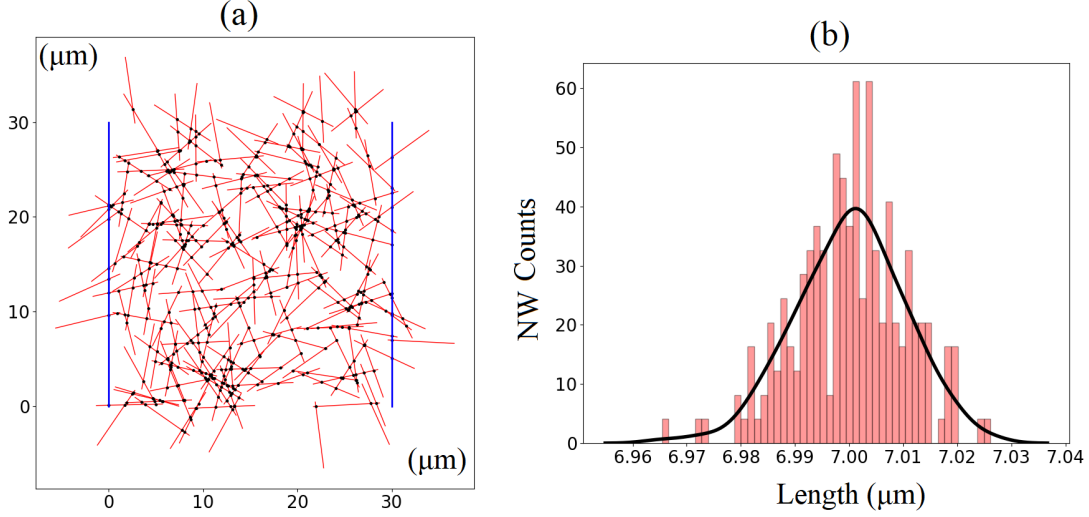
Figure 2.5: (a) A computer-generated random NWN with a wire density of $n_w = 0.25\,\mu\mathrm{m}^{-2}$ composed of nanowires (red lines) with $\langle L_w \rangle = 7\,\mu\mathrm{m}$ and $\sigma_{std} = 0.01\,\mu\mathrm{m}$ (standard deviation) taken from the Gaussian length distribution shown on panel (b). The dimensions of the network are $30 \times 30\,\mu\mathrm{m}$, and the electrodes are indicated by the vertical blue lines on each side of the network. The intersections between two nanowires are shown by the black circles. (b) Histograms of nanowire lengths are shown in red bars and the corresponding normal distribution in black bell shape with $\langle L_w \rangle = 7 \pm 0.01\,\mu\mathrm{m}$.

The placement, shape, and material properties of the electrodes used to interrogate the NWN electrically are also important factors that can affect the resistance and current flow characteristics of the system [100]. Resistance is expected to increase with the separation of the electrodes and this is depicted in Figure 2.6 (a). Each data point was calculated using in-house codes written in Python language [159] that compute the sheet resistance of random NWNs with a fixed number of nanowires $N_w = 300$. Another important characterization conducted by our computational implementation is to predict how the n_w relates to the density of interwire junctions (n_j). This can be obtained by building a NWN ensemble at incremental nanowire densities and determining the average interwire intersections per unit of area. Figure 2.6 (b) depicts this relation which is expected to follow a quadratic dependence as $n_j = w_j L_w^2 n_w^2$ with w_j being a fitting parameter determined as $w_j = 0.318$ [82, 165].
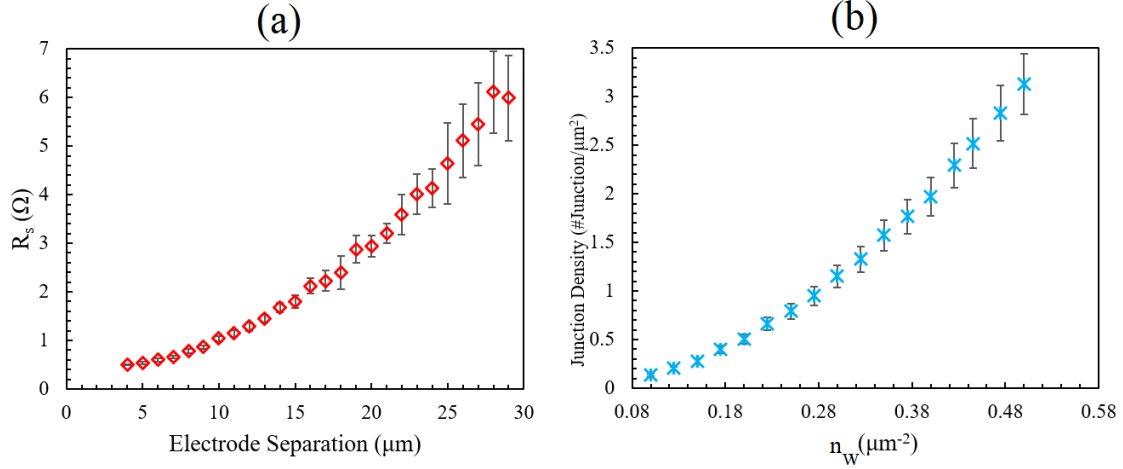
Figure 2.6: (a) Sheet resistance versus electrode separation obtained for an ensemble of random NWNs made of Ag nanowires. Every data point is the average taken from 10 NWN samples, and we also depict the standard deviation as error bars. The dimensions of the NWNs were fixed at 30×30 μm. The resistances were calculated assuming JDA for the sake of illustration. All junction resistances were set to be $R_{jxn} = 30$ Ω, and the nanowire lengths were set to be $L_w = 7$ μm for all nanowires, and the total number of nanowires was fixed at $N_w = 300$. (b) Interwire junction density versus nanowire density obtained for ensembles of random NWNs made of Ag. Every data point is the average taken from 10 NWN samples, and we also depict the standard deviation as error bars.

The junction resistance information is a common resistive metric between MNR and JDA. To compare the difference between these two models, one may require to fix R_{jxn} and run the simulation for a variety of different NWN geometries to find the relationship between these two approaches. This relationship has been already investigated in our group in past works [144], but we repeated the same analysis in this thesis to make sure that our most updated codes can also reproduce the expected differences between the two approaches. Figure 2.7 (a) depicts the sheet resistance versus nanowire density for JDA and MNR models for NWNs made of nanowires of fixed aspect ratio AR $= L_w/d_w = 233$, in which d_w is the diameter of the nanowires and L_w being the length of nanowires. The junction resistances were fixed at $R_{jxn} = 30$ Ω. In this figure, when both models have the same density, MNR exhibits greater sheet resistances than JDA; this is because MNR considers R_{in}, making the network systems more "resistive". The sheet resistance values depicted in the figure are average values taken over 10 random NWN configurational samples and the error bars

represent standard deviations. Deviations around $\langle R_s \rangle$ are found to be larger, particularly for NWNs with densities close to that of the network's critical density ($n_c \sim 0.1~\mu m^{-2}$) which can be estimated from Equation (2.1). This enhancement in uncertainty in the sheet resistance is a reflection of the sparsity of the network in which spatial fluctuations associated with the randomness of the nanowires' positions play a larger role in the electrical response of sufficiently sparse systems. The sheet resistance average (and its associated standard deviation) is reduced as the NWN density increases due to the creation of additional parallel pathways in the network.
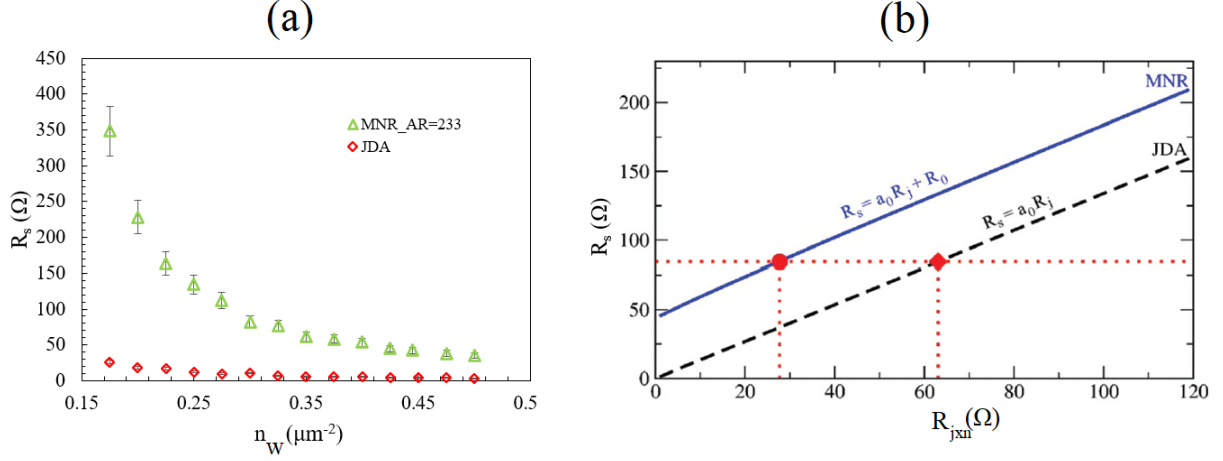
Figure 2.7: (a) The impact of varying n_w on the R_s for Ag NWNs with dimensions of 30×30 μm and nanowires of 7 μm in length using two distinct voltage-nodal approaches: JDA and MNR. For the case of the MNR simulation, the diameter of the nanowires is fixed at 30 nm where we can obtain the AR ~ 233. Each data point represents the average sheet resistance taken over an ensemble containing 10 random NWNs and the error bars represent the standard deviations. The junction resistance was fixed at R_{jxn} = 30 Ω, and ρ = 19.2 nΩm. (b) The influence that the junction resistance has on the sheet resistance of random NWNs treated in accordance with JDA and MNR. Both models predict that the sheet resistance increases linearly with the junction resistance but they are offset due to the contribution of inner wire resistances that JDA does not account for. The red horizontal dashed line indicates an experimental sheet resistance value measured in laboratory. If that particular NWN sample was treated in accordance with MNR or JDA, the models would consider different junction resistance contributions which are reflected/marked by the vertical dashed lines. Linear functions were fitted to the numerical results in which the slope (a_0) and the intercept (R_0) of the functional $R_s(R_j)$ = $a_0 R_j + R_0$ can be determined for both models, MNR and JDA. Note that in this figure $R_j \equiv R_{jxn}$. Other parameters relevant to this result are the nanowire resistivity of ρ = 22.6 nΩm, the diameter of the nanowires d_w = 50 nm, the wire density of n_w = 0.28 μm^{-2} and the wire lengths of L_w = 6.7 μm. Panel (b) is reproduced from Ref. [144] with permission from the Royal Society of Chemistry.

Figure 2.7 (b) shows the computed R_s as a function of the R_{jxn} for JDA (dashed line in black) and MNR (blue solid line). This result can be found in [144]. Note that in that figure notation, $R_j \equiv R_{jxn}$. It can be observed that the sheet resistance increases linearly with R_j for both descriptions (JDA and MNR). The two models are not identical in every respect; for example, JDA accounts only for the junction resistances of the NWNs, as a result, R_s will only consider this contribution in the form of $R_s = a_0 R_j$, in which the slope a_0 can be determined numerically. The latter carries information about the nanowire density

and effective information about the NWN connectivity. MNR, however, incorporates the inner resistances of the wires, as a result, R_s needs to account for two main contributions coming from the junction and inner resistances, i.e., $R_s = a_0 R_j + R_0$, where a_0 is the slope and R_0 is the resistance intercept that the network would have if all interwire resistances were set at $R_j = 0$. Hence, the discrepancy in R_0 between the JDA and MNR models compensates for the effect of the R_{in} on the total sheet resistance, and it is solely governed by the network's design, material properties, and connection. It is important to discuss this result to establish the quantitative difference between the JDA and MNR models which will be adopted intermittently in this thesis. Emphasis will be given to MNR due to its enhanced quantitative features due to the possibility of incorporating materials' properties by means of inner resistances. We worked mostly with random NWNs made of metallic nanowires, i.e., Ag, Au, Al, and Cu, in which distinct material information can be included in the model by altering the resistivity value ρ.

2.4 Optical Modelling of Random Nanowire Networks

After introducing the electro-model used to describe the electrical resistance properties of random NWNs, we proceed in introducing the optical model that will allow us to compute the optical transmission of the studied systems. Levels of transparency in thin films have a direct relation with its optical transmission, which can be intuitively understood as how much light the film enables to be transmitted. How much light can pass through the NWN depends strongly on the nanowire density and the reflective properties of the materials used for the nanowires. Therefore, a number of different strategies for correlating the NWN density with their optical performance have been presented. Some of these approaches are semi-empirical in nature and did not take into consideration the nanowire dimensions; instead, they relied on extrapolating bulk percolation behaviour to derive the sheet resistance (R_s) and optical transmittance (T_{op}) of NWNs [102,166]. Other works combining experimentation

and theoretical analysis to relate the electro-optical characteristics of NWNs such as in Equation (1.1) [126] have been successful in establishing overall trends between R_s and T_{op}, but these predictions can be highly dependent on nanofabrication specs and instrumentation settings. The applicability of these models can be rather restricted; more specifically, they might rely on diameter- and wavelength-dependent coefficient values, or they might only apply to networks that are in the percolation regime, i.e., networks that are relatively sparse with $T_{op} > 90\%$ [167]. One of the goals of this study is to establish an experimental-free computational method that will allow one to extract the optical characteristics of NWNs regardless of their geometry, shape, and wavelength of incident light.

To gain a grasp of the optical characteristics of a NWN, one must first analyse what percentage of its surface area is covered by the nanowires. If the amount of light that is blocked by a single nanowire is comparable to its geometric cross-section extension, then the amount of light that is blocked by a whole NWN is roughly equal to its AF (area fraction) given by the area covered by the nanowires divided by the total area in which the network is deposited. An effective way of computing a NWN AF is given by the following expression [84, 97, 98, 166]

$$AF = n_w\, L_w\, d_w \tag{2.7}$$

in which n_w is the number of nanowires per unit area, d_w is the diameter of the nanowires, and L_w is the length of the nanowires. In addition, the quantity of light that is obstructed by a single nanowire can be characterised by its extinction efficiency coefficient denoted by the $Q_{ext} = \sigma_{ext}/A$, where σ_{ext} is the extinction cross-section and A is the nanowire cross-section area projected onto a plane perpendicular to the incident beam. Thus, the amount of light that is blocked by a NWN film is thus $AF \times Q_{ext}$ and the attenuation in optical transmittance will obey the Beer-Lambert law given by [84, 97, 98, 166]

$$\%T_{op} = \exp\{-AF \times Q_{ext}\}. \tag{2.8}$$

From the equation above, the determination of the AF can be done effectively via Equation (2.7) or it can be computed in detail by inspecting the area coverage outlined by a given NWN geometry using image processing techniques. The calculation of Q_{ext} however needs a robust theory that accounts for the interaction of light with matter. In this thesis, the MLST [107] and the FEM methodology coupled with Maxwell's equations employed in COMSOL Multiphysics® software [110] were adopted to carry out the calculations necessary for determining the extinction optical properties in nanowires. Within the framework of the MLST formalism [107], optical characteristics are derived from the effective analytical solutions to Maxwell's equations, which take into account the scattering of electromagnetic radiation by nanoparticles. One of the shortcomings of the MLST approach is that its accurate solution is limited to only highly symmetrical geometries such as cylinders, spheres, and spheroids [168], for which independent radial and angular dependencies of solutions according to the object's coordinate systems can be written. The book written by Bohren and Huffman provides a comprehensive analysis of the precise electromagnetic wave solution required for MLST [107]. To calculate the extinction efficiency coefficients, we examined the Mie electromagnetic wave scattering solution that was presented for a uniform infinite cylinder implemented in the MatScat software and created by Schäfer [109, 169]. The outcome of this analysis is the $Q_{ext} = Q_{sca} + Q_{abs}$, in which Q_{abs}, Q_{sca}, and Q_{ext} are the absorption, scattering, and extinction efficiency factors, respectively. The COMSOL Multiphysics® interface modelling software [110] is an alternate tool for simulating the optical transmission of nanoparticles with unusual forms such as curved nanowires or nanowires of square cross-section shapes. We were able to solve Maxwell's differential equations in both 2D and 3D space domains by modelling the dispersed electric field of the particle subjected to light using COMSOL Multiphysics® software [110] at either the nano or microscales. The FEM analysis was carried out using the "electromagnetic waves" and the "frequency domain" interfaces that are accessible in the RF module within COMSOL Multiphysics® software [110]. In the next sub-sections, we will detail the background of both methods (MLST and FEM) used

in this thesis to determine the Q_{ext} of distinct nanowire systems which consequently allowed us to quantify T_{op} in conjunction with in-house programming codes that output R_s values. This is the first step towards coupling electro-optical degrees of freedom in NWN systems.

2.4.1   Mie Light Scattering Theory (MLST)

MLST [170] can be used to predict scattering cross sections for single spherical or infinite cylindrical particles irradiated by a plane wave [107]. The size parameter $\mathcal{X} = 2\pi R_{radius}/\lambda$ characterizes the scattered field, where R_{radius} and λ denote the particle's radius and the wavelength in the surrounding medium, respectively. The relative refractive index $m_{idx} = n_s/n_l$ describes the ratio of the refractive index of the scattering particle and surrounding medium. It is worth noting that the complex refractive index can be defined by both real and imaginary parts as such $\epsilon = \tilde{n} + i\tilde{k}$ in which the real component of a refractive index is the ratio of the speed of light in free space to the phase velocity of an electromagnetic wave in the medium, and the imaginary part is associated to the absorption coefficient [107, 171]. Figure 2.8 gives the refractive index of the target four materials of this thesis (Ag, Au, Al, and Cu) as a function of wavelength ranging from 200 nm to 1200 nm [172–174]. As it can be seen, almost all materials own similar imaginary indices (blue line) within the visible light wavelength (delimited by the vertical black dashed lines) except Al which inherits higher absorption coefficients. Furthermore, comparing the refractive indices of Au with Cu, one may conclude that they will behave similarly under identical situations as they follow the same trend. Another interesting feature is the fact that Ag exhibits relatively low $\tilde{n}$ values within the visible wavelength region (~ 400 nm to 700 nm). Because our focus is on the visible wavelength region, we will concentrate on quantifying materials' properties and identifying the best materials' performance for TCE applications within this spectral wavelength range.
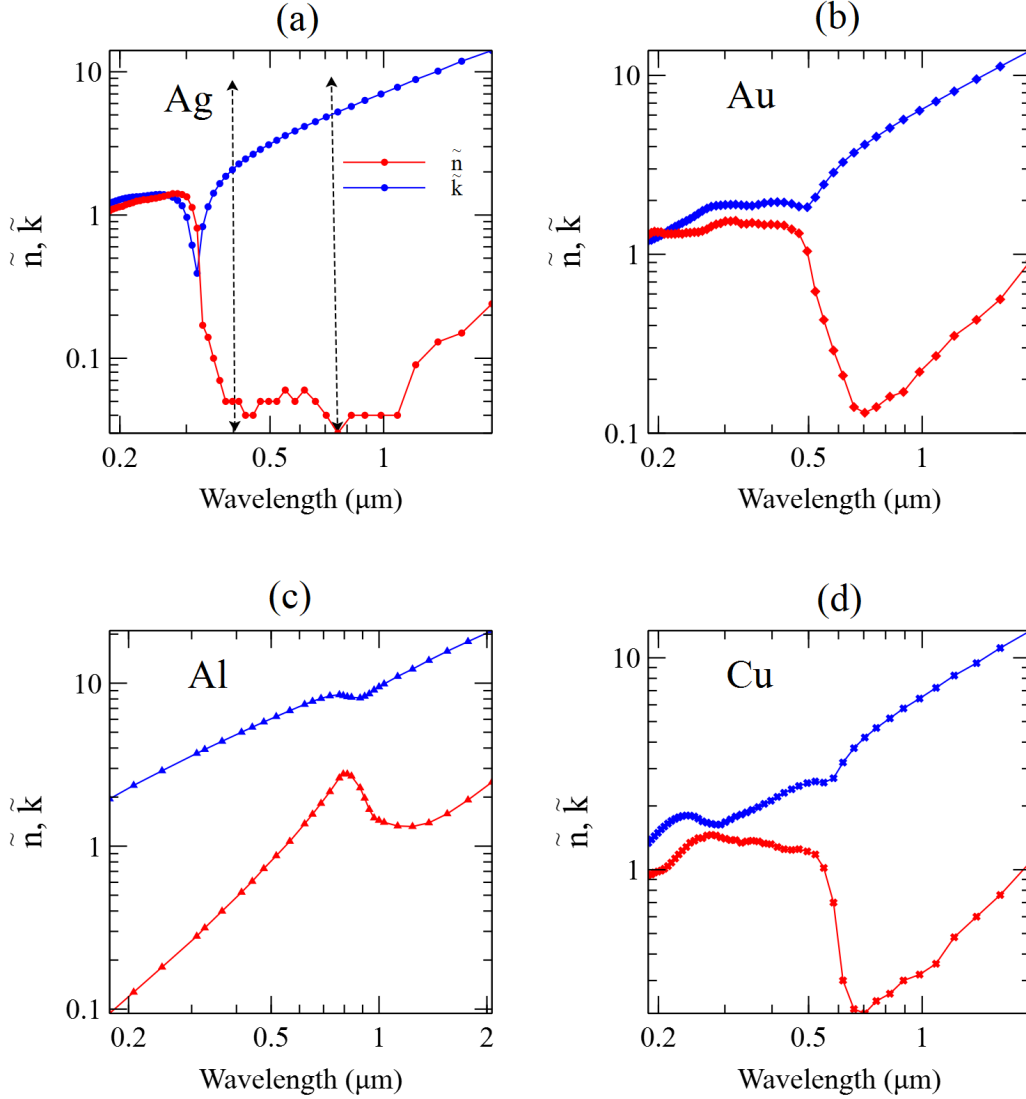
Figure 2.8: Real ($\tilde{n}$, red colour circles) and imaginary ($\tilde{k}$, blue colour circles) components of the refractive index of four materials including (a) Ag [172, 174], (b) Au [172, 174], (c) Al [173, 174], (d) and Cu [172, 174] as a function of wavelength. The vertical dashed lines on panel (a) illustrate the visible wavelength region which is ~ 400 nm to 700 nm.

This thesis aims to calculate the optical transmission of disordered NWNs by accounting for the effects of optical scattering at the nano and microscales. To do so, it is vital to have a firm grasp of the fundamental quantities concerning optical scattering from particles, in particular those with the shape of a cylinder as nanowires have this geometry. The size and composition of the particles and the wavelength of the incoming light all have

impacts on the scattering direction of light. The MLST gives a rigorous framework to explain the interaction of light with nanoparticles, allowing for a mathematical description of the scattering behaviour of light by solid-state particles. According to the MLST, the polarization of the dispersed light from a solid cylinder depends on both the polarization state of the incoming light and the cylinder's orientation. The extinction efficiency factor ($Q_{ext} = \sigma_{ext}/A$) is a fundamental parameter obtained from the MLST to characterise the capacity of a particle to scatter and absorb incoming light. The term refers to the proportion of the total extinction cross-sectional area (σ_{ext}) of a particle in relation to its geometric cross-sectional area (A). The total extinction cross-sectional area (calculated from all the scattered fields off the particles exposed to unpolarized light) is equivalent to the average of the scattering and absorption cross-sectional areas of the particle. In MLST, the polarization of the incoming light is a crucial factor. Light waves can appear either polarized or unpolarized (oscillation of light in all possible directions perpendicular to the direction of travel), depending on the direction of the electric field vector that constitutes the wave. Depending on the size, shape, and direction of the scattering particles, polarized light could interact with them differently, resulting in more intricate scattering patterns and polarization effects. Unpolarized light, on the other hand, is a combination of light waves of various polarizations and phases. It is easier to compute the scattering cross-section for unpolarized light since the scattering patterns are the average across all polarization states. It is also frequently more suitable and relevant to deal with unpolarized light because this is the case in many practical real-world applications [107, 170, 171].

In order to obtain the final form of the optical scattering expressions for the case of an infinite solid cylinder, one needs to write the time-dependent Maxwell's equations in such a way that the field vectors $\overrightarrow{E}$ (electric field) and $\overrightarrow{H}$ (magnetic field) satisfy the vector wave equation in cylindrical coordinate system [107]. Then, we employ appropriate boundary conditions such that $L_w >> d_w$ ($2R_{radius}$) to consider the cylinder to be infinitely long [107, 170, 171]. Consider the case of an infinite cylinder with a radius R_{radius}, on which

an incident plane wave forms an angle ζ with the axis of the cylinder. There are two potential polarizations for the incident beam: I) the electric field polarization plane is perpendicular to the axis of the cylinder, and II) the electric field polarization plane is parallel to the axis of the cylinder [107, 170, 171]. In the next, we are going to introduce the main equations that provide the relevant quantities for our optical description which are Q_{ext} and Q_{sca} associated with solid cylindrical structures being incident by an electromagnetic wave. It is not the scope of this work to re-derive all these equations as their formal derivation can be found in many textbooks and theses [107, 170, 171]. Our intent is just to highlight their main dependencies with the scattering properties of nanowires exposed to light as studied in this thesis.

Case I: The electric field polarization plane is perpendicular to the axis of the cylinder [107, 170, 171].

In this particular case, the efficiency factor of the scattering can be described by the following formula

$$Q_{sca,I} = \frac{2}{\mathcal{X}} \left[|b_{0I}|^2 + 2 \sum_{n=1}^{\infty} (|b_{nI}|^2 + |a_{nI}|^2) \right] \tag{2.9}$$

and the efficiency factor of the extinction can be written as

$$Q_{ext,I} = \frac{2}{\mathcal{X}} Re \left[b_{0I} + 2 \sum_{n=1}^{\infty} b_{nI} \right] \tag{2.10}$$

in which $\mathcal{X} = 2\pi R_{radius}/\lambda$ is the size parameter defined earlier, b_{0I}, b_{nI}, and a_{nI} are the coefficients that require to be defined as a function of the diameter of the cylinder and their relative refractive indices to the surrounding medium as follows:

$$a_{nI} = \frac{C_n V_n - B_n D_n}{W_n V_n + i D_n{}^2}, \; b_{nI} = \frac{W_n B_n + i D_n C_n}{W_n V_n + i D_n{}^2} \tag{2.11}$$

where subscript "I" stands for 'Case I', n is the index that runs the summation over the quantities, and the coefficients C_n, V_n, B_n, W_n, and D_n are described by the following expressions

$$D_n = n\cos(\zeta)\eta J_n(\eta)H_n^{(1)}(\xi)\left(\frac{\xi^2}{\eta^2} - 1\right),$$

$$C_n = n\cos(\zeta)\eta J_n(\eta)J_n(\xi)\left(\frac{\xi^2}{\eta^2} - 1\right),$$

$$B_n = \xi\left[m_{idx}^2\xi J_n'(\eta)J_n(\xi) - \eta J_n(\eta)J_n'(\xi)\right],$$

$$V_n = \xi\left[m_{idx}^2\xi J_n'(\eta)H_n^{(1)}(\xi) - \eta J_n(\eta)H_n'^{(1)}(\xi)\right],$$

$$W_n = i\xi\left[\eta J_n(\eta)H_n'^{(1)}(\xi) - \xi J_n'(\eta)H_n^{(1)}(\xi)\right],$$

$$\xi = \mathcal{X}\sin(\zeta), \qquad \eta = \mathcal{X}\sqrt{m_{idx}^2 - \cos^2(\zeta)}.$$

(2.12)

In the above equations, J_n and $H_n^{(1)}$ are the Riccati-Bessel functions first kind of n-order. The prime character denotes differentiation with regard to the argument that is enclosed in the parentheses. ζ is the angle formed between the incident plane wave with the axis of the cylinder, and η is the dimensionless simplified coefficient. If the incident field is in a direction that is perpendicular to the axis of the cylinder ($\zeta = 90^0$), $a_{nI} = 0$. Thus, b_{nI} will be

$$b_{nI}(\zeta = 90^0) = \frac{J_n(m_{idx}\mathcal{X})J_n'(\mathcal{X}) - m_{idx}J_n'(m_{idx}\mathcal{X})J_n(\mathcal{X})}{J_n(m_{idx}\mathcal{X})H_n'^{(1)}(\mathcal{X}) - m_{idx}J_n'(m_{idx}\mathcal{X})H_n^{(1)}(\mathcal{X})}. \qquad (2.13)$$

Case II: The electric field polarization plane is parallel to the axis of the cylinder. Similarly, the efficiency factor of the scattering for Case II is

$$Q_{sca,II} = \frac{2}{\mathcal{X}}\left[|a_{0II}|^2 + 2\sum_{n=1}^{\infty}(|a_{nII}|^2 + |b_{nII}|^2)\right] \qquad (2.14)$$

and the efficiency factor of the extinction can be written as

$$Q_{ext,II} = \frac{2}{\mathcal{X}}Re\left[a_{0II} + 2\sum_{n=1}^{\infty}a_{nII}\right] \qquad (2.15)$$

with a_{0II}, a_{nII}, and b_{0II} coefficients given as

$$a_{nII} = \frac{-A_n V_n - iC_n D_n}{W_n V_n + iD_n{}^2}, \quad b_{nII} = -i\frac{C_n W_n + A_n D_n}{W_n V_n + iD_n{}^2} \tag{2.16}$$

in which A_n is

$$A_n = i\xi \left[\xi J_n{}'(\eta) J_n(\xi) - \eta J_n(\eta) J'(\xi)\right]. \tag{2.17}$$

The terms V_n, C_n, D_n, and W_n are same as those defined in Equation (2.12).

Ultimately, if the incident beam is unpolarized, the efficiencies are

$$Q_{sca} = \frac{1}{2}(Q_{sca,I} + Q_{sca,II}), \quad Q_{ext} = \frac{1}{2}(Q_{ext,I} + Q_{ext,II}). \tag{2.18}$$

Figure 2.9 depicts a cylinder over the Cartesian coordinate system in which its axis is aligned with the $\hat{z}$-axis. This cylinder is illuminated by an unpolarized incident beam having a wavenumber of $k = 2\pi/\lambda$ propagating along the $\hat{x}$-axis and λ is the wavelength.
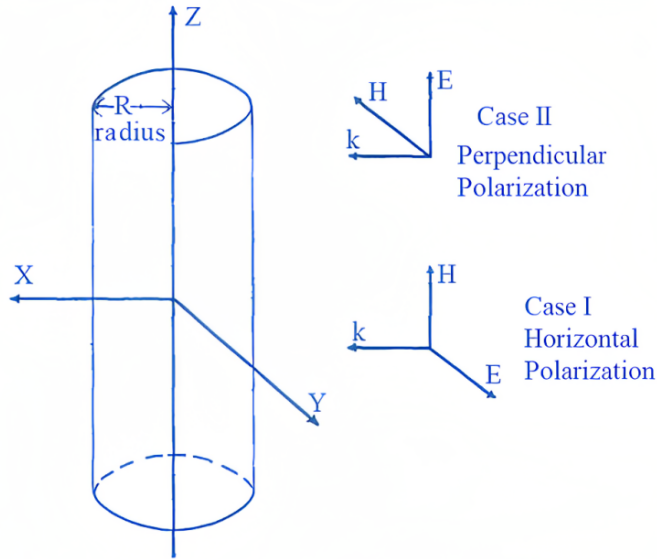
Figure 2.9: A cylinder structure over a Cartesian coordinate system to illustrate the geometry adopted for the cases I and II described in the main text; R_{radius} is the radius of the cylinder, and k is the wavenumber. $\vec{E}$ and $\vec{H}$ are the electric and magnetic vector fields, respectively.

51

The description above is a brief overview of the MLST for an infinite cylinder and it can be found coded in a MATLAB package named MatScat developed by Schäfer [109, 169]. We installed MatScat and ran for distinct nanowire diameters, material composition, and incident wavelength to determine Q_{ext} required to compute the optical transmission of NWNs as in Equation (2.8). The AF in the equation is determined by our in-house codes that can compute the coverage area of a NWN based on the pixel information of a computer-generated NWN image. By combining R_s and $\%T_{op}$ in a plot, we can obtain the FOM of NWN systems as done in earlier studies [84, 98] with great agreement with experimental trends. We considered the Q_{ext} taken from MatScat as the standard for the extinction values used in our simulations. Nonetheless, besides MatScat, we also set another modelling scheme to obtain Q_{ext} values that gave us more flexibility in establishing other conditions for our studied systems which go beyond the idealized infinite cylinder case, e.g., nanowires of squared cross-section shapes or finite nanowires. We set up a COMSOL Multiphysics® [110] model to characterize light scattering due to a solid cylinder (and other object shapes) that also provided Q_{ext} values for our FOM simulations. The setup for the COMSOL Multiphysics® [110] model is based on finite element method (FEM) and some of its key settings are explained below. All criteria and settings for the COMSOL [110] model were done considering that there should always be a match between the numbers outputted by MatScat and the COMSOL [110] software when infinite and uniform structures were investigated.

2.4.2 Optical Simulation Applying Finite Element Method

In this research, we used the MLST implemented in MatScat software [108] and the FEM technique introduced in COMSOL Multiphysics® software [110] to characterise the spectral properties of individual nanowires. This section explains the process involved in the construction of the nanowire model with incident light using COMSOL Multiphysics® software [110]. In order to numerically solve Maxwell's equations in the frequency domain, a FEM analysis was created. This analysis made use of the "electromagnetic waves" and "fre-

quency domain" interfaces that are accessible by the RF module in COMSOL software [110]. The infinite cylinder was modelled in COMSOL [110] by placing a 2D circular disc in the xy-plane. This disc was designed to be illuminated by a plane wave that travelled in a direction normal to the object and had two incident excitation modes, which are depicted in Figure 2.10: the transverse magnetic (TM) mode and the transverse electric mode (TE). In our setup, the direction of the electromagnetic wave was along the $\hat{y}$-axis, and its polarizations were aligned with the $\hat{x}$- and $\hat{z}$-axes. By averaging the two perpendicular electric field polarizations, the optical extinction coefficients were derived. Nanowires with diameters of 30 nm and 50 nm have been created in order to generate a model of the 2D circular disc. To simulate confined and non-reflecting infinite domains, the perfectly matched layer (PML) was given the required amount of thickness. Mesh computing was used to discretize both the object's surface (in 2D) and its volume (in 3D). The latter was accomplished via the use of 'physics-controlled mesh refining' even though we meet the custom setting for elements' size by progressively shifting the mesh from normal to extremely fine. This method was carried out so that the meshed geometry would be suitable for spectral identification. The skewness measure revealed that the lowest and average element quality of our mesh were 0.5647 and 0.8303, respectively. We solved Maxwell's wave equations numerically with regard to the distributed electric field as

$$\nabla \times \mu_r^{-1}(\nabla \times \vec{E}) - k_0^2 \left(\epsilon_r - \frac{j\sigma_{cond}}{\omega\epsilon_0} \right) \vec{E} = 0, \quad k_0 = \frac{2\pi f}{c}. \tag{2.19}$$
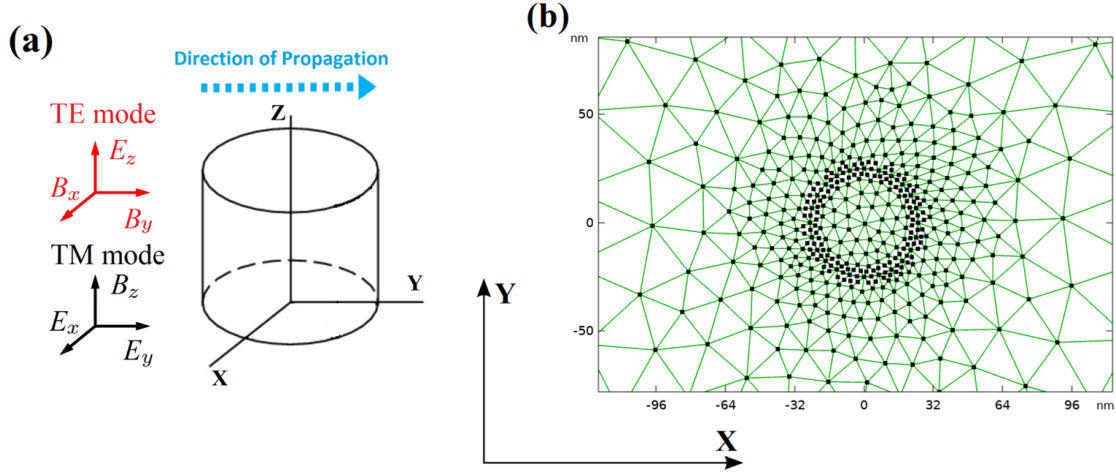
Figure 2.10: (a) A single nanowire is shown schematically as a cylinder when the incident electric field impinges on the object's surface. The excitation rays were perpendicular to the surface and travelled along the $\hat{y}$-axis. The cylinder symbolises a nanowire with light travelling in the $\hat{y}$ direction and two orthogonal polarizations: TM and TE, which represent transverse magnetic and transverse electric polarized waves, respectively. (b) A 2D circular disc was built to model the circular cross-section of an infinite cylinder. The circle represents the cylinder's cross-section (top view). The meshing components are represented by the green line segments and dots that are distributed across the space. Reproduced from Ref. [97] with permission from the Royal Society of Chemistry.

In the above equation, ϵ_r and μ_r are the relative permittivity and permeability, respectively. In addition, ϵ_0, σ_{cond}, $\vec{E}$, ω, f, and c describe the vacuum permittivity, electrical conductivity, electric field, angular frequency, wave's frequency, and the speed of light, respectively. $\nabla\times$ is the "curl operator", and j is the imaginary number. The total extinction cross-section can be calculated as $\sigma_{ext} = \sigma_{sca} + \sigma_{abs}$ where σ_{ext}, σ_{sca}, and σ_{abs} stand for the extinction, scattering, and absorption cross-sections (in units of meter for 2D and in square meters for the 3D modelling), respectively. Their explicit definitions are given as [175, 176]

$$\sigma_{abs} = \frac{W_{abs}}{P_{inc}}, \qquad \sigma_{sca} = \frac{W_{sca}}{P_{inc}} \qquad (2.20)$$

in which the absorbed energy rate is denoted by W_{abs} and the dispersed energy rate is denoted by W_{sca} and both are in units of W (Watts). The quantity P_{inc} represents the incident irradiance, which can be calculated based on the energy flux of the incident wave

54

in units of Wm^{-2}. The rate at which the nanowire absorbs energy, as shown in Equation (2.20), can be outlined by the integration of the energy loss, denoted by Q_{loss}, over the volume element dV. The following relationship can be used to interpret this integration

$$W_{abs} = \iiint Q_{loss} dV = \frac{1}{2} \iiint Re\left\{J_{tot}\, E^* + j\omega B\, H^*\right\} dV, \ \ J_{tot} = \sigma_{cond} E + j\omega D \qquad (2.21)$$

in which J_{tot} is the total current density, the electric displacement field is given by D, and the magnetic field is denoted by $B(H)$ (strength). The symbol " $*$ " in the superscript implies a conjugate gradient and $Re\{\cdots\}$ takes the real part of the term. The Gauss Divergence Theorem states that the amount of a vector field passing through a closed surface is related to the amount of divergence of the vector field within the enclosed volume. Hence, W_{sca} can be given by

$$W_{sca} = \oiint Re\{(\vec{E}_{sca} \times \vec{H}^*_{sca}) \cdot \hat{n}\, dS\}. \qquad (2.22)$$

In the integration of the enclosed surface shown above, $\hat{n}$ is the surface normal unit vector pointing outward, dS is the surface integral element, and "sca" is the associated scattering label. Due to the fact that we used plane waves, the flux of the relevant Poynting vector is approximated as ($\hat{k}$ represents the direction of the incident wave)

$$P_{inc} = \frac{1}{2c\epsilon_0}\left|E_{inc}{}^2\right|\hat{k} \qquad (2.23)$$

in which E_{inc} is the incident electric field. To acquire the optical efficiency values, $Q = \sigma/A$ (Q_{ext}, Q_{sca}, and Q_{abs}), the cross-sections (σ_{ext}, σ_{sca}, and σ_{abs}) for each contribution are divided by the nanowire's respective cross-sectional area (A). For the 2D circular disc model, the cross-sectional area is represented by a line segment that has the same length as the disk's diameter. In the case of the 3D cylinder model, the cross-sectional region is reflected by a rectangle defined by the length and the diameter of the 3D nanowire (see Figure 2.11). Using a 3D model to study straight nanowires also gave us the possibility of studying curved

nanowires. As illustrated in Figure 2.11, it is crucial to examine the cross-sectional area of a nanowire which is bent in three dimensions by subtracting the area that is contained inside two concentric semicircles.

$$A = \iint_0^\pi r_{radial}\, dr d\theta = \pi \int_{r_{radius}}^{R_{radius}} r\, dr = \frac{\pi}{2}(R_{radius}^2 - r_{radius}^2)$$
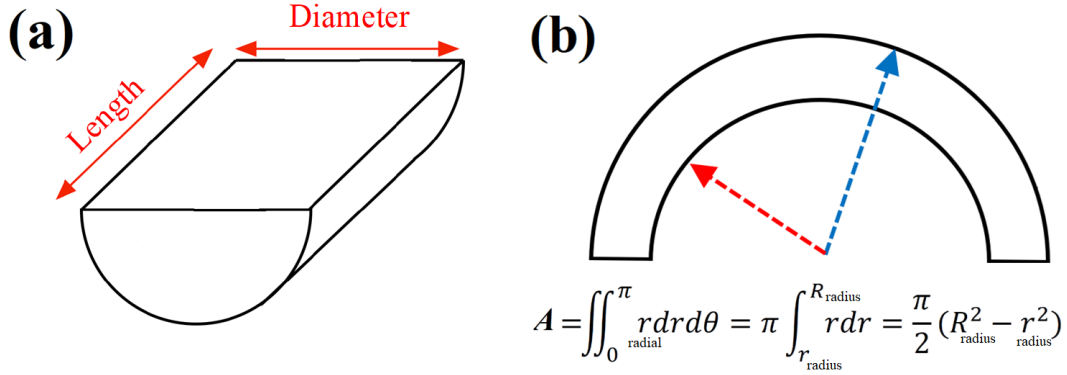
Figure 2.11: Cross-section view of (a) a straight nanowire and (b) a curved nanowire. (a) Surface area of a finite cylinder (rod) that envelops an area which is rectangular with A = Length × Diameter. (b) Cross-sectional view of a bent nanowire (side view). The area of the cross-section, denoted by A, can be calculated by integrating the surface integral element probing radial (r_{radial}) and angular (θ) degrees of freedom. θ is integrated within the range of $[0, \pi]$, and the radial element is integrated from the inner radius (shown by the red arrow, r_{radius}) all the way out to the outer radius (indicated by the blue arrow, R_{radius}). Reproduced from Ref. [97] with permission from the Royal Society of Chemistry.

Figure 2.12 (a-c) illustrates the absorption, scattering, and extinction efficiency coefficients that were calculated using COMSOL Multiphysics® software [110] for the 2D modelling approach. The findings are presented for four different materials, namely Ag, Au, Al, and Cu, shaped as a cylinder of diameter of 30 nm. The comparatively high Q_{ext} values demonstrated by Al within the shown wavelength suggest that Al may provide weaker transparencies in contrast to the other materials. As a result, Al is less desirable for use in applications requiring transparent conductors because of these relatively high Q_{ext} values. These findings are in excellent agreement with those produced via MatScat [108], as we will discuss further in Chapter 3. This figure also shows a comparison between the 2D and 3D modelling schemes applied to describe the efficiency coefficients of an Ag cylindrical nanowire shaped in a straight or bent fashion (see Figure 2.12 (d)). The dimensions of the nanowire (diameter

and length) were set to be d_w = 50 nm and L_w = 7 μm. Assessing the efficiency coefficients of an infinite Ag cylinder captured by the 2D circular disc model [blue lines on panels (a-d)] and a finite nanowire captured by the 3D rod model [magenta and black lines on panel (d)], reveals that they both have a similar trend; however, the 3D rod model (straight and curved) exhibits peaks above 600 nm wavelengths. Curved and straight Ag nanowires display comparable Q_{ext} behaviour, with the exception that the peaks are displaced. One needs to keep this in mind while evaluating the optical characteristics of curved and straight nanowires, especially for wavelength ranges greater than 600 nm. The interaction between light and a nanowire can result in the generation of a plasmon, which is a collective oscillation of free electrons in the metal. The phenomenon of resonance takes place when the frequency of the incident light aligns with the natural frequency of the oscillating electrons of the nanowire, resulting in a heightened absorption or scattering of light by the nanowire. The interaction between light and a nanowire results in the emergence of plasmons. Plasmons can be stimulated by the incoming light and exhibit resonance at distinct frequencies [177]. Subsequently, the plasmon has the capability to emit energy through the dispersion of light. The extent of scattering emanating from the nanowire is significantly influenced by the dimensions and configuration of the nanowire, in conjunction with the wavelength and polarization of the incoming light. The scattering spectrum of a thin nanowire exhibits a sequence of distinct resonance peaks. The resonances manifest due to the Fabry-Pérot cavity-like behaviour of plasmons within the nanowire. The Fabry-Pérot cavity is a system where light undergoes multiple reflections between two mirrors, resulting in constructive/destructive interference and the emergence of resonant modes. Plasmons have the ability to undergo reflection in a back-and-forth manner between the two extremities of a nanowire. This phenomenon results in constructive/destructive interference and the consequent emergence of resonance peaks in the scattering spectrum. The characteristics of the resonance peaks are contingent upon the dimensions, cross-sectional area, and constitutive properties of the nanowire. Through the manipulation of these parameters, it is feasible to customise the scattering spectrum and

fabricate nanowires possessing distinct optical characteristics that can be utilized in diverse applications such as photonics, sensing, and imaging. The phenomenon of scattering from thin nanowires is intricate and heavily reliant on the interplay between the geometry of the nanowire and plasmon resonances [178]. The plasmon resonances are observed in the form of sharp peaks in our investigation as shown in Figure 2.12 (d).
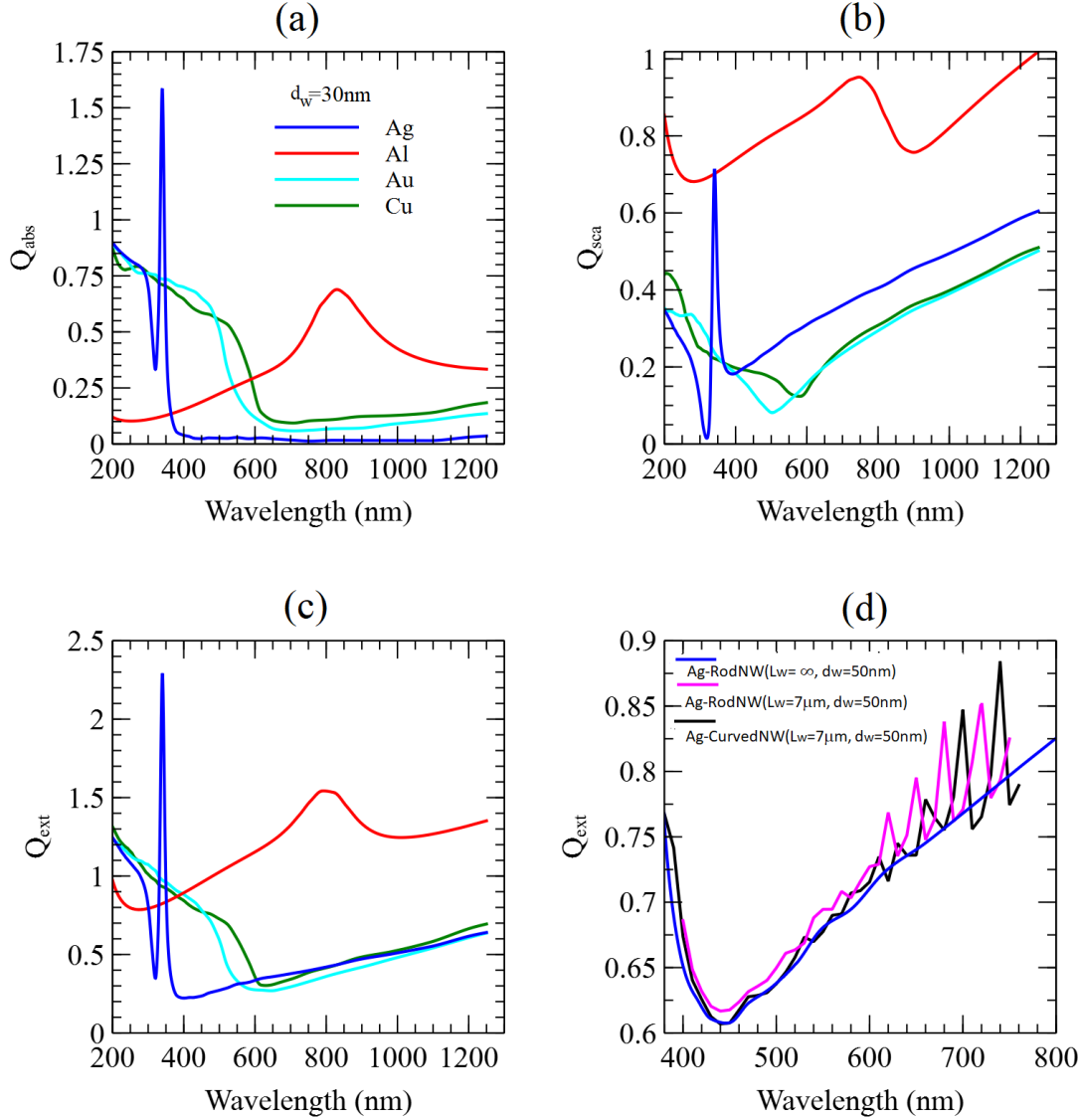
Figure 2.12: (a) Absorption, (b) scattering, and (c) extinction efficiency coefficients computed employing COMSOL Multiphysics® software [110] for different materials (Ag, Al, Au, Cu) for nanowires with cylindrical shapes of diameters of 30 nm. The wavelength spanned between 200 nm and 1250 nm. These outcomes were determined using the 2D circular disc model. (d) Extinction efficiency values as a function of wavelength ranging from 350 nm to 750 nm of an Ag single nanowire obtained using COMSOL Multiphysics® software [110]. The magenta, black, and blue lines refer to straight-finite, curved-finite, and infinite nanowires, respectively. In this case, the nanowires have the same diameter of 50 nm and length of 7 μm for both straight or curved (arc length) configurations. These figures were re-plotted according to the calculations and results depicted in our publication [97].
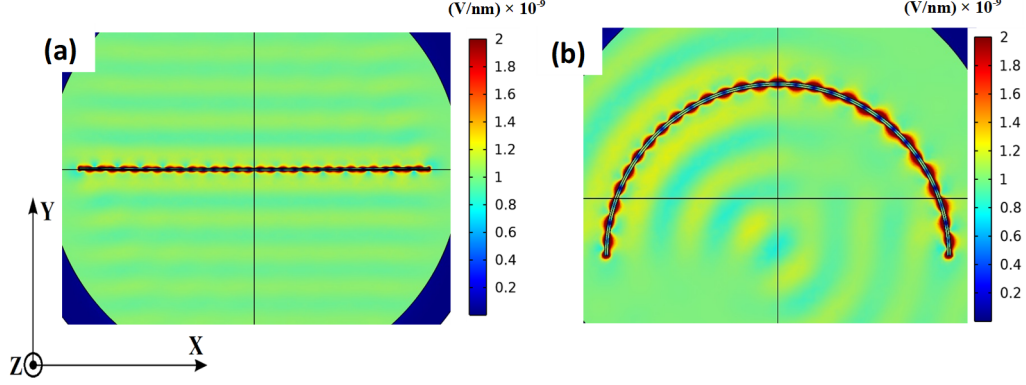
Figure 2.13: Electric field intensity colour map around an Ag (a) straight-finite and (b) curved-finite nanowire or nanorod. The geometrical features of the nanowire are the diameter of d_w = 50 nm and the finite arc/straight length of L_w = 7 μm. The wave of the electric field, in this case, travels along the $\hat{z}$-axis, and it has two different polarizations along the $\hat{x}$-axis and the $\hat{y}$-axis. The electric field strength present on each panel is quantified in the colour bar. Colour maps illustrate the illumination of an Ag (a) straight-finite nanowire by a 680 nm light wave and by a (b) curved-finite nanowire 700 nm light wave. These wavelength values correspond to Q_{ext} peaks found in Figure 2.12 (d). Reproduced from Ref. [97] with permission from the Royal Society of Chemistry.

Figure 2.13 depicts the optical characterizations of the 3D straight-finite and curved-finite Ag nanowires. The figure displays the simulated electric field intensity surrounding the Ag nanowire at the wavelengths of 680 nm (straight) and 700 nm (curved), respectively. Each of these wavelengths coincides with the peaks in the Q_{ext} plot seen in Figure 2.12 (d). Oscillations in the electric field intensity surrounding the wires are observed and caused by the localised surface plasmon resonance which can be detected at certain ratios of the wavelength of the incident light (λ) and the aspect ratio of the object AR, i.e., λ/AR [178–181].

Now that the main theoretical background is covered, Chapter 3 will examine the tunability of the electrical and optical properties of standard random NWNs. The chapter will focus on the examination of the trade-off between two distinct network configurations: a randomly dispersed nanowire structure and an alternative structure that integrates an additional grid pattern to enhance light transmission. Furthermore, Chapter 3 delves into an investigation of how the geometric characteristics of nanowires, such as their curvature and

orientation, can impact the electrical and optical features of these irregular networks.

2.5 Note on Computational Resources

Some of the computational scripts designed in-house to obtain the results achieved in this work were run on high-performance workstations available at the University of Calgary (ARC), and the Digital Research Alliance of Canada. MatScat package [108] and other supporting MATLAB/Python libraries were successfully installed in our workstations from which serial jobs were submitted to run in the background/queues for the required calculation walltime. We also utilized the CAD Compute Cluster within the CMC Microsystems [182] to perform COMSOL calculations. On average, our jobs required 16 hours to execute a complete optical scattering simulation of a nanowire in a 2D environment using COMSOL Multiphysics® software [110] as will be described in Chapter 3. A typical 2D job utilized two nodes and a total of 32 cores, with an average memory of 2584 MB. Furthermore, on average, our jobs required ~3.5 hours to execute an electrothermal computational analysis in a 3D setting in COMSOL Multiphysics® software [110] as will be described in Chapter 4. For some of these tasks, our jobs used two nodes and a total of 32 cores, with an average memory of 4907 MB.

Chapter 3

Exploring The Tunability of Electrical and Optical Properties of Random Nanowire Networks

Preamble

This chapter is based on Esteki et al. "Tuning the electro-optical properties of nanowire networks" published in Nanoscale [97].

3.1 Introduction

Conductive and transparent metallic nanowire networks are seen as possible replacements for ITO in upcoming flexible next-generation technologies owing to their outstanding opto-electronic characteristics and inexpensive production costs. Such systems rely heavily on the geometrical, physical, and intrinsic features of the nanowire materials, as well as the arrangement of the device. Prior to construction, it is vital to simulate and quantify the optical and electrical responses of the device using detailed computational analysis. In this chapter, we provide a computational toolset that uses the electro-optical characteristics of several de-

vice layouts, including conventional random NWNs and transparent mesh pattern layouts. Nanowires of Al, Au, Cu, and Ag are the materials of interest for transparent conducting electrodes in this research. We have investigated a range of adjustable factors, such as network area percentage, length-to-diameter aspect ratio, and nanowires angular orientations, under a variety of device designs. In addition, the optical extinction efficiency factors of each material are evaluated using two distinct methods: MLST [107–109] and FEM in COMSOL Multiphysics® software [110]. We analysed a variety of nanowire network architectures and estimated their relative FOM (optical transmittance versus sheet resistance), from which conclusions may be drawn on the design of next-generation transparent conductor devices. Following that, we will discuss the estimated and computed outcomes in accordance with the theoretical explanation presented in Chapter 2. The findings of the study that is carried out throughout this thesis are reported and published in this citation [97].

Many of today's electrical and optoelectronic gadgets demand the use of transparent conducting films as one of their layered parts [28, 90]. Particularly, TCEs composed of metallic NWNs [183] are a viable replacement for the most widely used ITO [184], which has been leading the planar display technology in recent years. However, the significant cost and restricted availability of indium, as well as ITO's brittle character and costly production procedure (through vapour phase sputtering [185]), have motivated scientists to explore other materials [29,72,90]. Metallic NWNs have exhibited mechanical deformability, minimal manufacturing costs, excellent optical transmission, and outstanding electrical/thermal conductivity [29,30,186]. Other technologies in which NWNs have shown remarkable operational efficiency include flexible displays and touchscreens [85], solar cells [89], wearable sensors [87], thin-film heaters [86], neural interfaces [88], and neuromorphic computing [54, 163] just to mention a few. According to Bae et al. [111], TCEs are required to have a high optical transmittance, which is normally ~ 90%, while the electrical sheet resistance is dependent on the operation and function of the device. These technologies, which range from touchscreens, and flexible displays up to solar cells, often function with unique resistance values that may be

as low as $1\,\Omega/\square$ or as high as $500\,\Omega/\square$ [111]. Thus, it is crucial to fine-tune these two parameters (transmittance and resistance) when engineering TCE devices for a particular purpose. Diverse materials, including conductive polymers [76], carbon nanotubes [74], graphene [92], ultra-thin metal films [129], and metallic nanowires [28, 187], have been evaluated as TCEs with the primary objective of determining the optimal trade-off between electrical conduction and optical transmittance [73]. Consequently, a FOM quantification is commonly used in which T_{op} versus R_s for various raw materials, intrinsic physical properties, and device designs [55, 90, 188] are produced to evaluate the performance of the device as a transparent conductive medium. Recent computational and experimental research has focused on FOM patterns to establish the best design of metallic NWNs as TCEs [84, 96, 98, 189, 190]. The electro-optical characteristics of these networks are affected by a number of design factors, including structural ones such as nanowire aspect ratio (AR_O) [96, 167], which is defined as the nanowire length (L_w) divided by the nanowire diameter (d_w), network density (n_w), which is quantified by the number of nanowires per unit of area, nanowire orientation [191], wire persistence lengths or curvature effects [192–194], and network area fraction (AF). In addition, electro-optical characteristics encompass junction resistances between nanowires (R_{jxn}), inner nanowire resistances given as $R_{in} = \rho L_w/A$ with A being the cross-sectional area of the cylinder and ρ being the resistivity, and optical extinction coefficients (Q_{ext}). Ultimately, geometrical aspects associated with device design, such as electrode shapes [100] and the incorporation of transparent grid patterns [104], together impact the percolative characteristic of the system's conduction and its light transmission. For example, it has been established, for instance, that the connection between R_s and AF is nonlinear and inverse; as the AF ratio rises, R_s will decrease, indicating that the increase in area coverage enhances electrical transport by creating extra parallel routes across the device [96]. If the wire density is increased at a given nanowire AR_O, R_s will decrease nonlinearly, with the resistance of a dense NWN moving from a percolative to bulk-like behaviour regime and saturating at a constant resistance value that relies on the bulk material characteristics and

film dimensions [190, 195]. Concurrently, this rise in density lowers optical transparency as a consequence of the increase in area coverage when more nanowires are introduced per unit of area. Wire density, however, is not the only factor that might influence the electro-optical properties of NWNs [189]. Such a multidimensional parameter phase space has prompted researchers to design optimal parameter configurations and settings to provide the best FOM trade-off between the greatest feasible transparency and an adjustable sheet resistance range acceptable for a certain TCE technology [163, 188].

RF emissions are also worth investigating as they may not only create malfunctions and limit the operational life of the device but can also have a negative impact on human health [196]. EMI SE (electromagnetic interference shielding effectiveness) must thus be considered while fabricating TCE films [104, 150, 197]. ITO films, for example, are stated to have a $R_s \sim 10$ $\Omega/\square$ and an optical transmittance of $\sim 90\%$, while Ag NWNs have a $R_s \sim 20$ $\Omega/\square$ and optical transmittance of $\sim 91\%$ [198]. In the frequency range of 0.5 – 3.0 GHz, ITO is reported to display EMI SE of 14 decibels (dB) @ 84.1% transmittance, while Ag NWNs exhibit EMI SE of 13.5 dB @ 90.3% transmittance [199]. In this chapter, we carried out a detailed computational investigation of randomly distributed and grid-patterned NWNs and evaluated their FOM for a number of metallic nanowire materials, including Ag, Al, and Au NWNs. Additionally, the contribution of nanowire alignment to the network's electrical conductance is investigated. The optical transmittance computations are performed utilizing the MLST [107, 170] and FEM with the COMSOL Multiphysics® software [110], and the sheet resistance is calculated with the simplified MNA [101, 144, 162] for a resistive circuit network as described in Chapter 2. All the details about the electrical and optical computations are laid out in Chapter 2. We have discovered that an optimal compromise between optical transmittance and sheet resistance can be achieved by manipulating the grid-pattern architecture of the networks, the density, the nanowire orientation, material parameters as well as $AR_\bigcirc$, and AF. In addition, we have investigated hybrid network architectures comprised of straight and curved nanowires represented as a

semicircle and analysed the influence of curvature on the overall conductance behaviour of the film. This study will contribute to the growth of cutting-edge TCE devices constructed out of metallic NWNs with optimum electro-optical capabilities by recommending materials and device layouts that can be customised for each kind of device.

3.2   Electro-Optical Modelling

To encapsulate the combined electrical and optical features of unique NWN systems, we have devised a computational approach that separately analyzes electrical resistance and optical transmission. The Monte Carlo approach is used to generate a random NWN as the initial step in the simulation process. Line segments that resemble cylindrical nanowires are randomly arranged in a squared area region. Inter nanowire connections are characterised by overlapping line segments, and all junctions are recognised prior to the electrical conduction simulations to assess network connectivity. The whole network structure is visualized as a resistive circuit network that has a number of voltage nodal points as well as inner and junction resistances. A two-terminal source/drain electrode configuration coupled to the network is assumed, and Ohm's law paired with Kirchhoff circuit rules is used to calculate the network sheet resistance as detailed in Chapter 2.

The optical property calculations are carried out employing two methodologies: (1) MLST [107] and (2) FEM with COMSOL Multiphysics® software [110]. MLST derives optical characteristics using accurate analytical solutions to Maxwell's equations that account for the scattering of electromagnetic radiation by particles [107]. One of the constraints of the MLST approach is that its accurate solution is limited to extremely symmetrical geometries, such as cylinders, spheres, and spheroids [168], for which one may write independent radial and angular dependency of solutions based on the object's coordinate systems. The book by Bohren and Huffman [107] provides a full discussion of the detailed electromagnetic wave solution for MLST, which is also briefly given in Chapter 2. In this work, we examined the

recommended Mie electromagnetic wave scattering solution for an infinite uniform cylinder as implemented in the MatScat program [109] to calculate the extinction efficiency coefficients given by $Q_{ext} = Q_{sca} + Q_{abs}$ in which Q_{ext}, Q_{sca}, and Q_{abs} are the extinction, scattering, and absorption coefficients, respectively.

COMSOL Multiphysics® interface modelling [110] provides an alternate method for calculating the optical transmission of particles having irregular forms, such as curved nanowires. We utilized COMSOL Multiphysics® software [110] to simulate the dispersed electric field off of the objects at nano and microscales by solving Maxwell's differential equations in 2D and 3D space domains. The "electromagnetic waves" and "frequency domain" interfaces of the RF module were used for the FEM study. MatScat [108] calculated optical efficiencies that served as our standard approach for reproducing experimental FOM trends, as shown in previous publications [84, 98]. In this manner, criteria for COMSOL Multiphysics® modelling [110] were determined using MatScat outcomes for uniform and infinite structures as a reference. For example, we have created an infinite cylinder model in COMSOL Multiphysics® software [110] by constructing a 2D circular disc reflecting the cross-section of a cylindrical nanowire enveloped by an outer circular disc that is the PML to truncate the physical domain in an infinite space medium. The simulation region was sufficiently partitioned into a physics-controlled meshing, and the interior disc material was chosen to match the known characteristics of the nanowire of interest, with air as the surrounding medium. The total effective optical response is determined by the influence of a background electromagnetic wave ($E_0 = 1$ Vm^{-1}) on the surface of the nanowire when the wavelength of the plane wave is modulated from ~300 to 1200 nm (or ~350 to 750 nm in the case of 3D curved and straight nanowires, see Figure 2.12 (d)). We utilized Johnson and Christy's [172, 174] integrated wavelength-dependent permittivity parameters in COMSOL Multiphysics® software [110] material database. To calculate the absorption, scattering, and extinction coefficients, suitable boundary conditions such as perfect electric conductors (PECs) and scattering boundary conditions, as well as surface and volume integrations, as

specified in Chapter 2, were needed. The direction of the target was adjusted such that the major axis of an infinite cylinder is perpendicular to the evolution of the electromagnetic field. Similar to MatScat [108], we have computed and averaged both orthogonal polarizations of the incident beam, one with an electric field perpendicular to the cylinder axis while the other parallel to it. Q_{ext} is strongly affected by a number of variables, including the diameter of the nanowire, the wavelength of the incoming beam, and the nanowire material's complex refractive index. Here, we determined the maximum light transmission, which represents the extinction efficiency factors at normal light incidence to the TCE film. The resulting extinction efficiency coefficients are taken as input data for the Beer-Lambert theorem [166] given in Equation (2.8) to analyze T_{op}.

To calculate the EMI SE of the NWNs, one can take into account the contribution from the total of three EMI losses: (1) microwave absorption (SE_A), (2) microwave reflection (SE_R), and (3) multiple reflections (SE_{MR}) [200]. The following equation can be used to estimate an independent frequency relationship (greater than 30 MHz) between EMI SE and R_s [147, 148, 200]:

$$\text{EMI SE} = 20 \log_{10}\left(1 + \frac{Z_0}{2R_s}\right) \tag{3.1}$$

in which $Z_0 = 376.7\ \Omega$ is the free space wave impedance. This equation demonstrates how the sheet resistance influences the EMI SE performance, highlighting the need of characterising the electrical characteristics of TCE films to satisfy the requirements of certain technological applications.

3.3 Results and Discussion

3.3.1 Nanowire Network Characterization

Herein, we demonstrate network configurations that were modelled in order to obtain numerically the FOM for many NWN devices and materials, including Al, Ag, and Au. To modify the electrical and optical responses of NWNs, we altered the percolation onset and the nanowires' inherent properties. Figure 3.1 displays schematics of the NWN systems studied in this section: (a) standard random NWNs, (b) random NWNs with a transparent grid pattern, (c) NWNs built of oriented nanowires by establishing their maximum angle with the horizontal axis at a given value θ_{max}, and (d) NWNs formed of oriented nanowires with the transparent grid-pattern. In addition, the impacts of the presence of curved nanowires in NWNs will be explored. Experimental micrographs of NWNs reveal the existence of curved or even L-shaped (kinked) wires, hence hybrid NWNs are created to represent more realistic physical systems [99, 201]. The NWNs have dimensions of 30×30 µm, indicating that the source and drain electrodes are separated by 30 µm. The aspect ratios ($AR_O = L_w/d_w$) of the nanowires studied range from 100 to 228. We performed simulations to calculate FOM for all system scenarios presented in Figure 3.1 for metallic nanowire materials. The nanowires' angular confinement with relative to the horizontal $\hat{x}$-axis was set between $\theta_{max} = \pm36^o$ and $\theta_{max} = \pm75^o$. We ran simulations by adjusting all physical parameters, comprising NWN density and area fraction, nanowire length and diameter. The mean sheet resistance and its standard deviation have been determined for a collection of NWNs with a fixed density and 10 random spatial configuration trials. We designated the applicable resistivity values of $\rho = 19.26$ nΩm, $\rho = 16.85$ nΩm, and $\rho = 25$ nΩm for Ag [98, 163], Al [81], and Au [202, 203], respectively. Variations in material properties and fabrication techniques can result in significant fluctuations in the resistance of junctions within NWNs. The range of reported values for junction resistance is typically between $1 - 200\,\Omega$ for metallic systems [81, 83, 84, 163, 202]. Furthermore, it is expected that the incorporation of junction resistance will lead to a linear

rise in the total sheet resistance of the network [144]. Thus, we set this value to R_{jxn} = 50 Ω for the findings reported in this section.
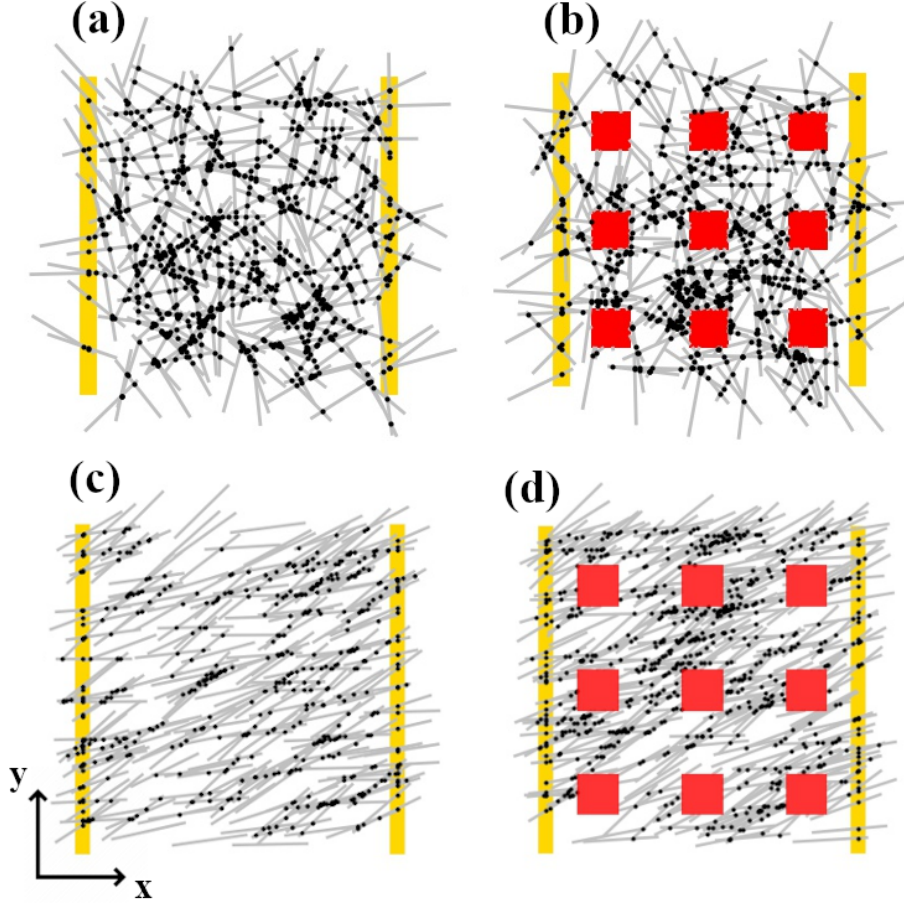
Figure 3.1: Diagrams of the four NWN systems examined in this study. In each panel, the grey lines indicate nanowires and the black circles depict their contact locations. The golden objects denote metallic electrodes to which a current source (not visible) is linked. The device dimension is 30×30 μm and all nanowires are made of a fixed length of L_w = 7 μm. (a) Standard random NWN with wire density of n_w = 0.3 nanowires per μm². (b) A 3×3 transparent grid shown with red squares is patterned over a random NWN with wire density of n_w = 0.3 nanowires per μm². This method aims to increase the transparency of the films. Each square is 4×4 μm in dimension. To clarify, the red squares mark regions in the NWN in which there are no nanowires, i.e., these are empty spaces. (c) A random NWN consisting of n_w = 0.4 nanowires per μm² with angular constraints. Each nanowire is randomly distributed throughout the device's surface; however, their orientation is limited by a maximum angle (in this example θ_{max} = ±45º) relative to the horizontal axis. (d) NWN combining the same structural features as in panel (c) and the same transparent grid pattern as in panel (b). Reproduced from Ref. [97] with permission from the Royal Society of Chemistry.

Optical Q_{ext} for metallic nanowires consisting of four distinct materials (Ag, Al, Au,

and Cu) with diameters of d_w = 30 nm and d_w = 50 nm were computed as a function of the light wavelength (λ) in the range of 300 − 1200 nm using both the MLST and FEM approaches and depicted in Figure 3.2. Q_{ext} was calculated for an infinite cylinder using two separate light scattering techniques, MatScat and FEM, with the latter accessible in the RF module of COMSOL Multiphysics® software. Figure 3.2 (a-d) indicates that the two approaches provide comparable results over the whole spectrum of wavelengths and cylinder sizes. Local electric field enhancement is material-dependent, with Al nanowire exhibiting the most powerful electric field scattering distributions at longer wavelengths. The computation of FOM for NWN TCEs is based on the combination of this coefficient and the numerically calculated AF of the NWNs, which yields the optical transmission through Equation (2.8). We utilized the Q_{ext} value at λ = 546 nm (taken from Figure 3.2) to quantify the optical transmission of every system examined in this study.
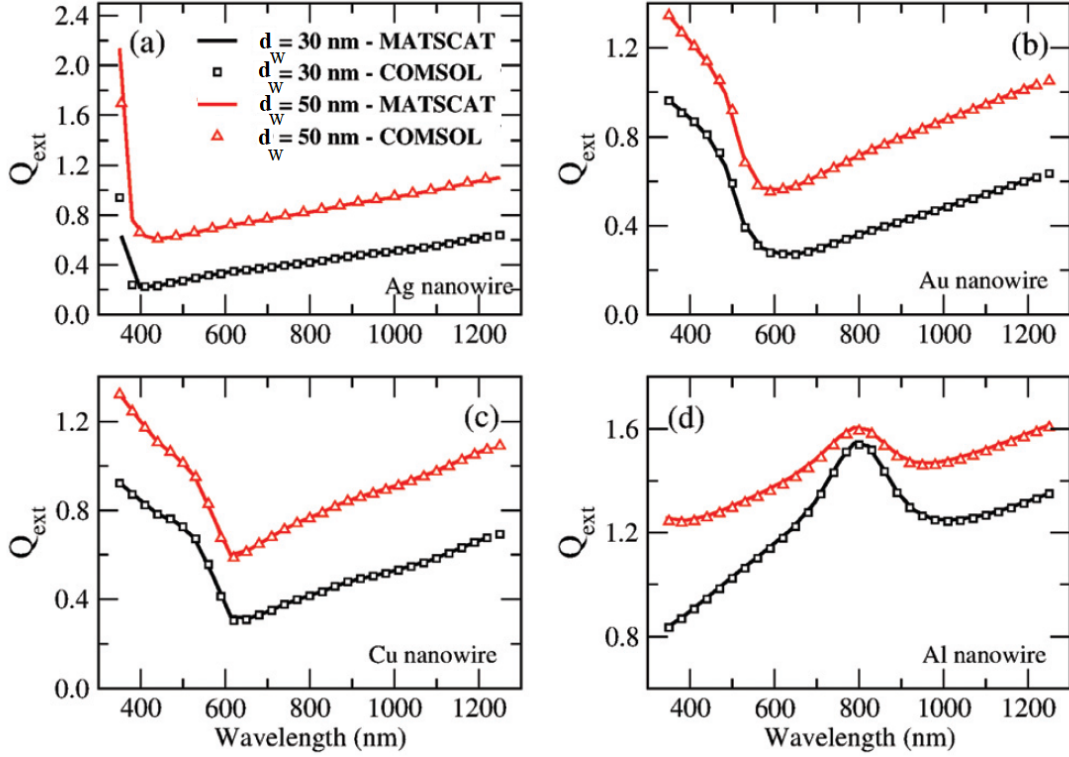
Figure 3.2: Q_{ext} of an individual nanowire calculated as a function of light wavelength varying from 300 to 1200 nm. The average of the two perpendicular electric field polarizations was used to determine all Q_{ext} values. Each panel displays the findings for a certain metallic material: (a) Ag, (b) Au, (c) Cu, and (d) Al. The legend presented in panel (a) applies to all remaining panels. All panels display findings for nanowires with two diameters, d_w = 30 nm (black symbols and lines) and d_w = 50 nm (red symbols and lines). MatScat [108, 109] (full lines) and COMSOL Multiphysics® software were utilized to conduct simulations [110]. Reproduced from Ref. [97] with permission from the Royal Society of Chemistry.

3.3.2 Electro-Optical Analysis of Metallic Nanowire Networks

The investigation of FOM for a range of materials and the impacts caused by either the nature of the materials or the structural aspects of the TCE NWN devices turns out to be a challenging optimization problem that can be carried out efficiently with computational simulations such as the ones conducted here. It is a trade-off analysis in which high transparencies necessitate decreasing area fraction while low sheet resistance necessitates the inverse.
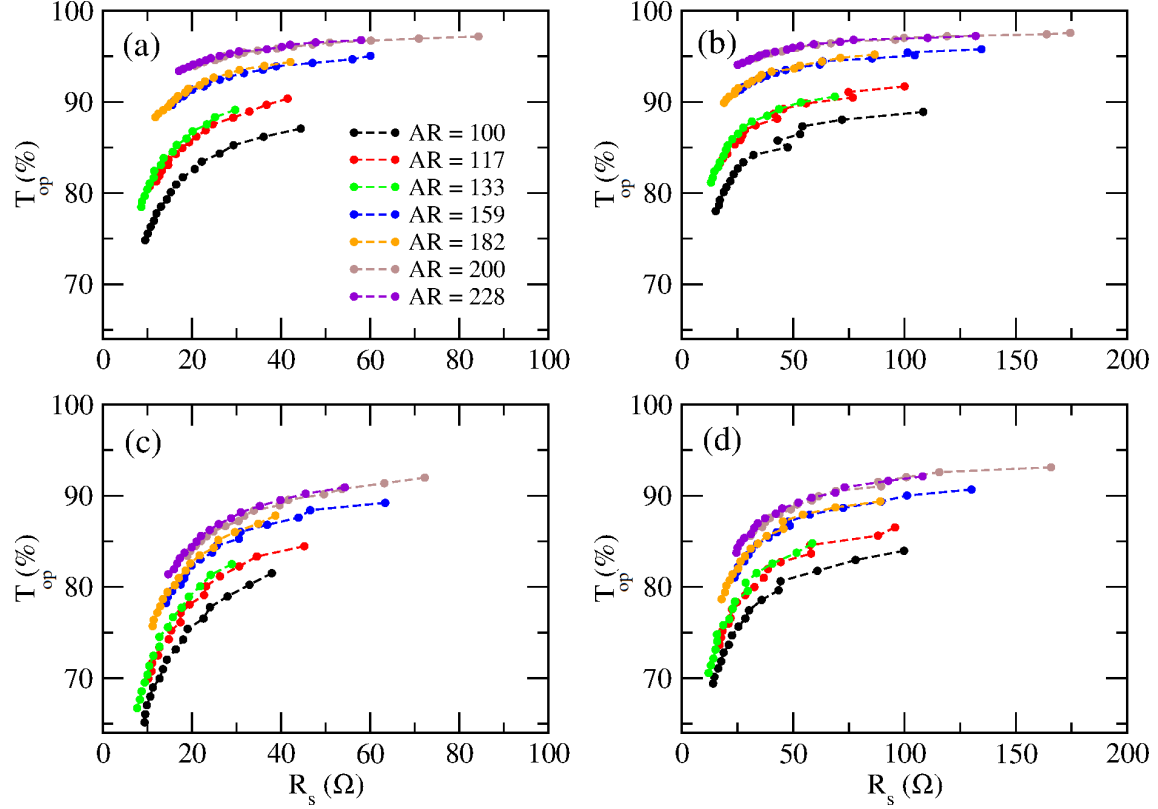
Figure 3.3: Results of various nanowire aspect ratios (here, AR≡AR$_O$) in terms of average optical transmittance expressed as a percentage T_{op} versus average R_s. Each data point is averaged across 10 random NWN samples with a particular density n_w. All systems are 30×30 μm in dimensions. NWN density was increased in increments of 0.025 nanowires per μm^2 from 0.3 up to 0.7. The findings of NWN TCE devices produced using Ag nanowires are shown in the upper panels (a and b), whereas Al nanowires are displayed in the lower panels (c and d). The left panels (a and c) display the FOM for standard random NWNs, while the right panels (b and d) display the FOM for transparent grid-pattern NWNs. The latter was generated with a 3×3 transparent grid as depicted in Figure 3.1. Reproduced from Ref. [97] with permission from the Royal Society of Chemistry.

Figure 3.3 displays mean $R_s \times T_{op}$ throughout AR$_O$ range of $100 - 228$ for varied NWN densities. Figure 3.3 (a,b) shows, respectively, the estimated FOM for random Ag NWNs with a standard and transparent grid layout, respectively. Figure 3.3 (c,d) exhibits the FOM for a standard and transparent grid pattern, respectively, produced from a different material, Al NWNs. The data depicted in Figures 3.3 (a) and (c) shows that R_s ranges $\sim 10 - 80$ Ω for both Ag and Al NWNs. However, it is apparent that Ag NWNs exhibit superior performance in terms of optical transmittance compared to Al NWNs. The data depicted in Figures 3.3

(b) and (d), on the other hand, show that the inclusion of a transparent grid pattern improves the optical transmission of the NWNs with a trade-off in sheet resistance with R_s ranging $\sim 25-150$ Ω.

In addition to the transparent grid pattern, imposing an angular limit on the nanowire alignments is another method for managing FOM in NWN devices. The greatest angle at which wires may be orientated with regard to the horizontal axis is regulated in the calculations; nevertheless, the location of the wires remains random. Figure 3.4 is a summary of these outcomes for standard and grid-mesh Ag NWNs with angle restraints. The latter adds a mechanism to tune the resistance range of our NWN devices. The amplification of sheet resistance variations in transparent grid-pattern NWNs is a further characteristic offered by this method. When the nanowire alignment is constrained, a new source of fluctuations in the sheet resistance values is introduced. These fluctuations will be the subject of a subsequent in-depth discussion when we examine the flow of current through the network frame. When compared to the other alignment trials, it was determined that $\theta_{max} = \pm 75^o$ was the dominating alignment angle to produce a greater FOM in terms of higher T_{op} and lower R_s.

Figure 3.5 depicts the FOM for another metal material studied in this research, Au NWN systems. For standard random and transparent grid-pattern Au NWNs of various ARs, the average optical transmittance versus sheet resistance was calculated. The graph also illustrates how the sheet resistance of the devices alters as a function of their AF. Transparent grids have a quantifiable influence on the network coverage area as shown in the figure. The area coverage is reduced by eliminating material from the network that allows light to flow through. By manipulating the AF in our devices, we can select how much transparency gain and sheet resistance loss the TCE devices will endure.
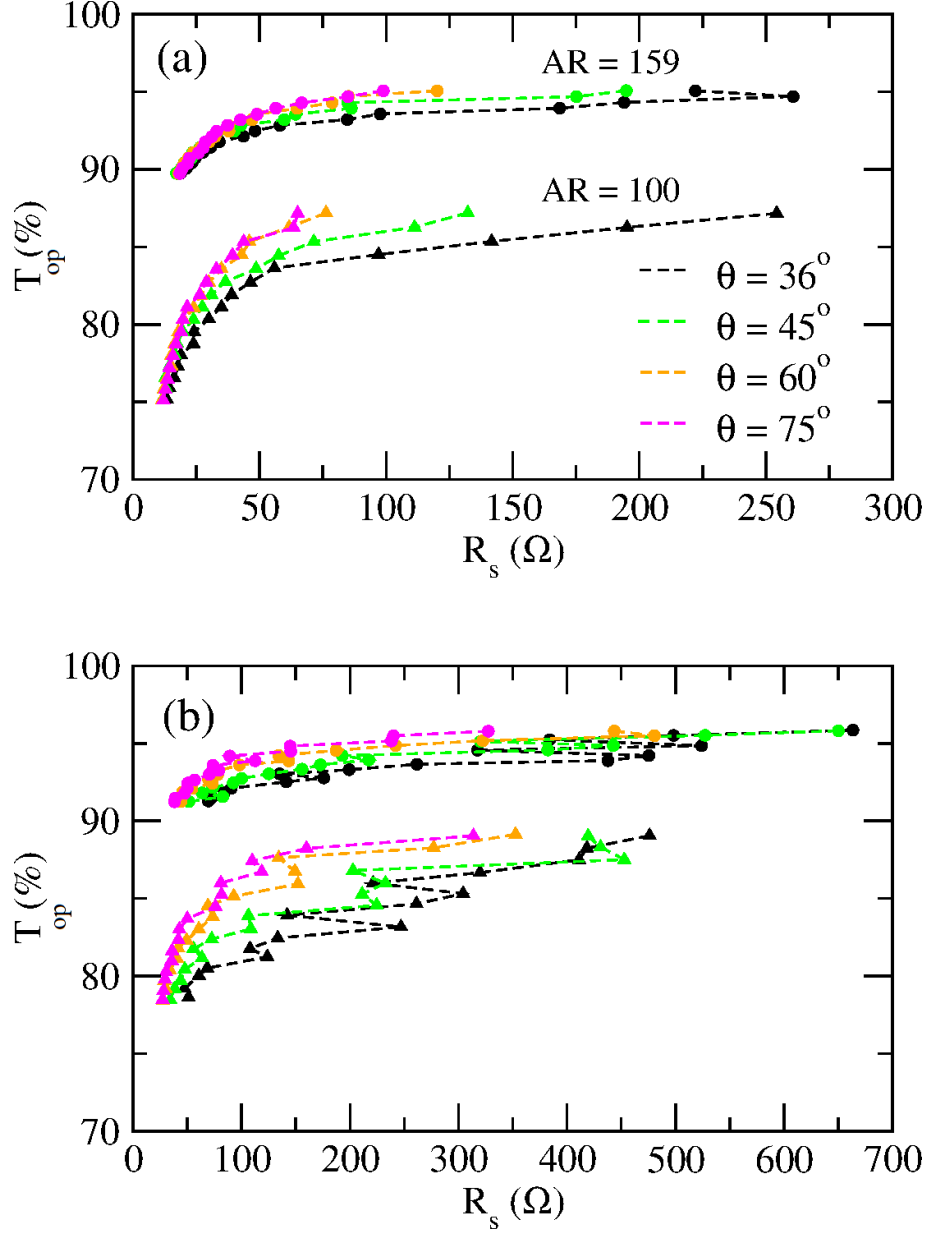
Figure 3.4: Average optical transmittance against sheet resistance of Ag NWN devices with a certain angular orientation of nanowires about the horizontal $\hat{x}$-axis. Two sets of AR are selected and shown in dashed-upper triangle lines and dashed-circle lines for 100 and 159, respectively. The maximum angles are established for both ARs (AR≡AR$_O$) as follows: θ_{max} = ±36°, ± 45°, ± 60°, ± 75°. All systems are 30 × 30 μm in dimensions. Each data point is averaged across 10 random NWN samples. n_w was increased in increments of 0.025 nanowires per μm^2 from 0.3 up to 0.7. Panel (a) displays the findings for standard random Ag NWNs, while panel (b) displays the results for Ag NWNs with a transparent grid pattern. Transparent grid NWNs were constructed using a 3 × 3 transparent grid just as in Figure 3.1. Reproduced from Ref. [97] with permission from the Royal Society of Chemistry.
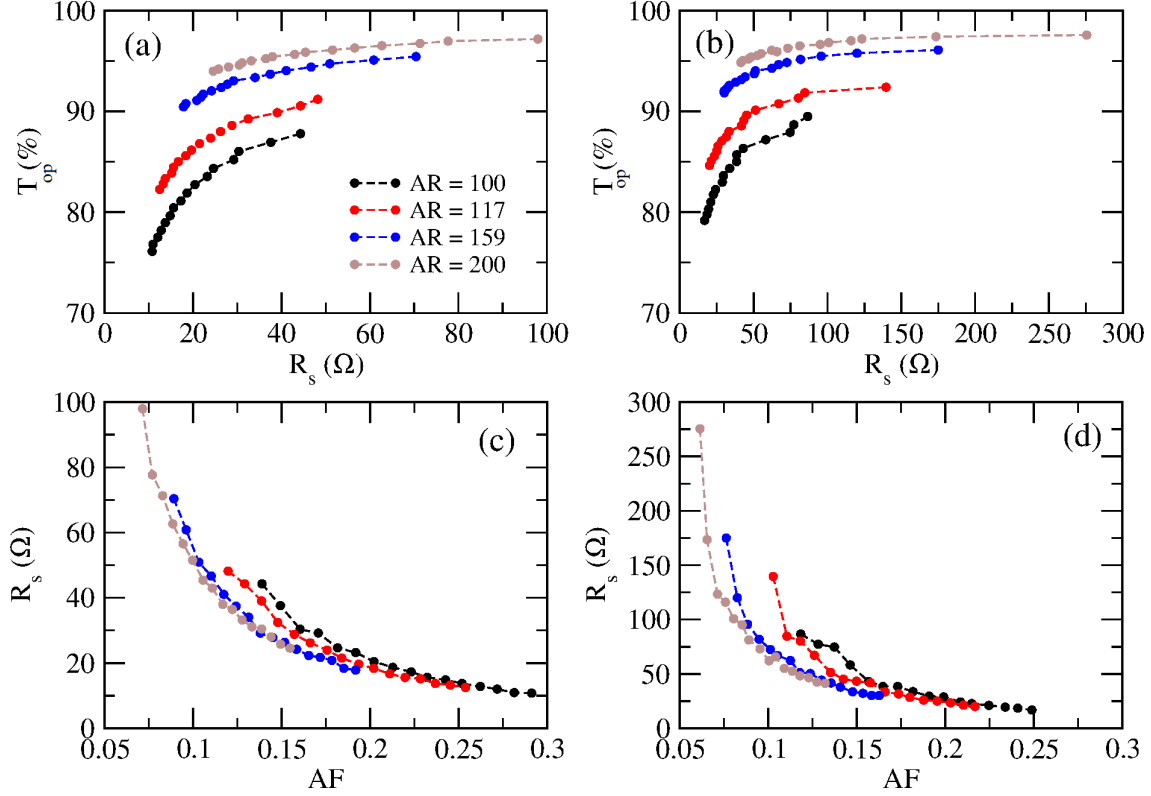
Figure 3.5: Top panels illustrate the FOM of varied nanowire aspect ratios (AR≡AR$_\bigcirc$) in terms of average optical transmittance expressed as a percentage T_{op} versus average R_s in (a) random standard NWNs and (b) transparent grid-pattern NWNs constructed with Au nanowires. Each data point is averaged across 10 random NWN samples with a particular density n_w. All systems are 30×30 μm in dimension. NWN density was increased in increments of 0.025 nanowires per μm^2 from 0.3 up to 0.7. The average R_s against AF are shown in the bottom panels for the identical systems that were investigated in the top panels: (c) for standard random Au NWNs and (d) for transparent grid-pattern Au NWNs. The transparent grid NWNs were constructed using a 3×3 grid just as in Figure 3.1. Reproduced from Ref. [97] with permission from the Royal Society of Chemistry.

All of these FOM results are, without a doubt, dependent on certain simulation parameters being used, such as the resistivity of the material, the resistances of the junctions, the geometrical aspects of the nanowires, the device dimensions and layout, and the optical features, to name just a few. These may be derived through *ab initio* approaches or from the data gained from experiments. We discovered trustworthy parameter sources [81,84,163,163,203], which allowed us to develop a diverse set of results that are pertinent to TCE research and to demonstrate the strength of our computational toolkit by analysing the relationship between

optical transmission and sheet resistance in a wide range of NWN systems.

To visually investigate the conduction mechanism prevailing in the NWNs investigated in this study, a spatial characterisation of electrical current flow across the NWN systems was carried out. This study is performed by numerically calculating the current flow via each nanowire segment on the network and translating this data into current colour maps, as shown in Figure 3.6. Current map results for a random and transparent grid-pattern Ag NWNs are shown in the top panels. The bottom panels depict current maps for a random and transparent grid-pattern Ag NWN with $\theta_{max} = \pm45^o$ for the orientation of the nanowires.
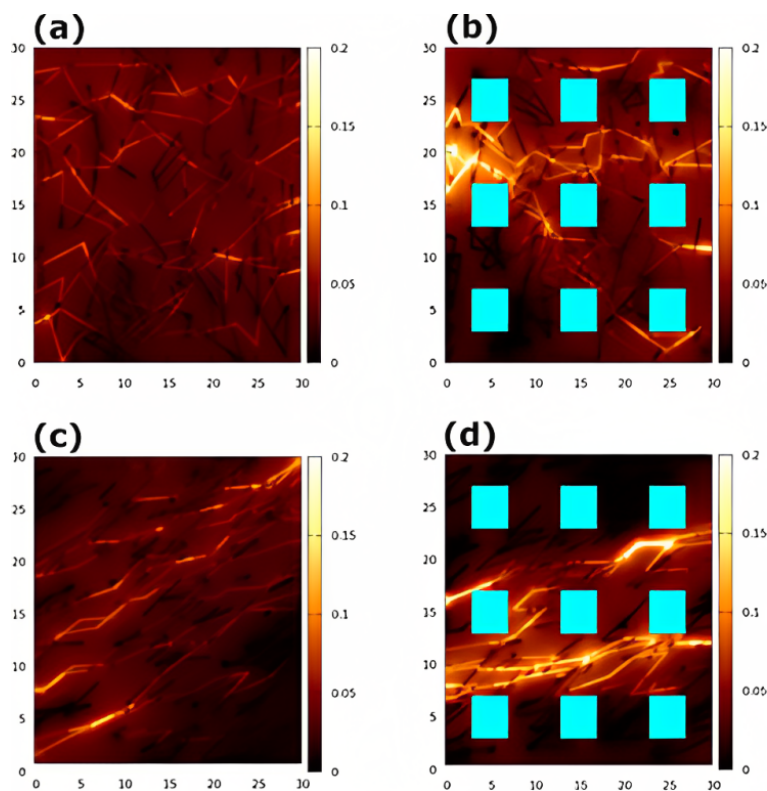
Figure 3.6: Current colour mappings determined for various Ag NWN structures. All systems are 30×30 μm in dimension. All networks have a constant wire density of $n_w = 0.4$ nanowires per μm^2. Colour bars indicate current intensity values in arbitrary units. The top panels (a,b) represent projections for a NWN with a random and transparent grid layout, respectively. The transparent grids are shown by cyan squares. Each square is 4×4 μm in dimension. The bottom panels (c,d) show current projections for a random and transparent grid-pattern Ag NWN, with orientation constraints imposed; in this instance, the maximum alignment of the nanowires relative to the horizontal axis is $\theta_{max} = \pm45^o$. Reproduced from Ref. [97] with permission from the Royal Society of Chemistry.

One may observe that the random NWN has topographically scattered current flow. The installation of transparent grids, which restricts the flow of current across particular network sectors, modifies this tendency. Figure 3.6 (b) depicts a "current hotspot" in the region of the left (source) electrode, which expands out as the current is directed towards the right (drain) electrode. The current will have a preferred orientation to flow when the angular restriction is enforced as shown in Figure 3.6 (c). As seen in Figure 3.6 (d), the transparent grid will partly obstruct this flow, which could result in more pronounced fluctuations in the sheet resistance when comparing samples with different densities. This indicates that the transparent grid and nanowire orientation may be utilized to regulate the network's current flow locally.

Figure 3.7 displays the mean EMI SE $\times n_n$ for AR_O ranges of $100 - 200$ for NWNs made of Ag and Au. Figure 3.7 (a) and (b) illustrate the outcomes for standard and transparent grid-pattern random Ag nanowires, respectively. Likewise, Figure 3.7 (c) and (d) exhibit the EMI SE outcomes for standard and transparent grid-pattern random NWNs, respectively, fabricated from a different material, Au nanowires. As seen in the figure, EMI SE is much larger for standard NWNs than for transparent grid networks; hence, a shielding mechanism is necessary to regulate the transmission of electromagnetic waves across the system.

For the analysis of curvature effects in NWNs, Figure 3.8 depicts the comparison of Ag NWNs made of purely straight nanowires with hybrid NWNs containing a certain concentration of straight and curved nanowires. We began by estimating the average $\langle R_s \rangle$ and $\langle AF \rangle$ of an Ag NWN ensemble with a density of $n_w = 0.4$ μm^{-2} that consisted only of straight wires and no curved ones (see Figure 3.8(a)). n_c denotes the density of curved wires, and in this initial condition, $n_c = 0$. The following panels illustrate $\langle R_s \rangle$ and $\langle AF \rangle$ of an Ag NWN ensemble having a concentration of curved nanowires such that the overall network density is maintained at 0.4 μm^{-2}, i.e., $n_w + n_c = 0.4$ μm^{-2}. The figure also includes images taken from the NWN ensemble as a visual aid. Percolation effects and resistivity trends in curved NWNs have been studied in earlier studies [99, 204] and our findings agree with

78

their predictions showing that the network's sheet resistance rises as the concentration of curved wires increases. Curved wires, on the other hand, can increase optical transparency by reducing their area fraction.
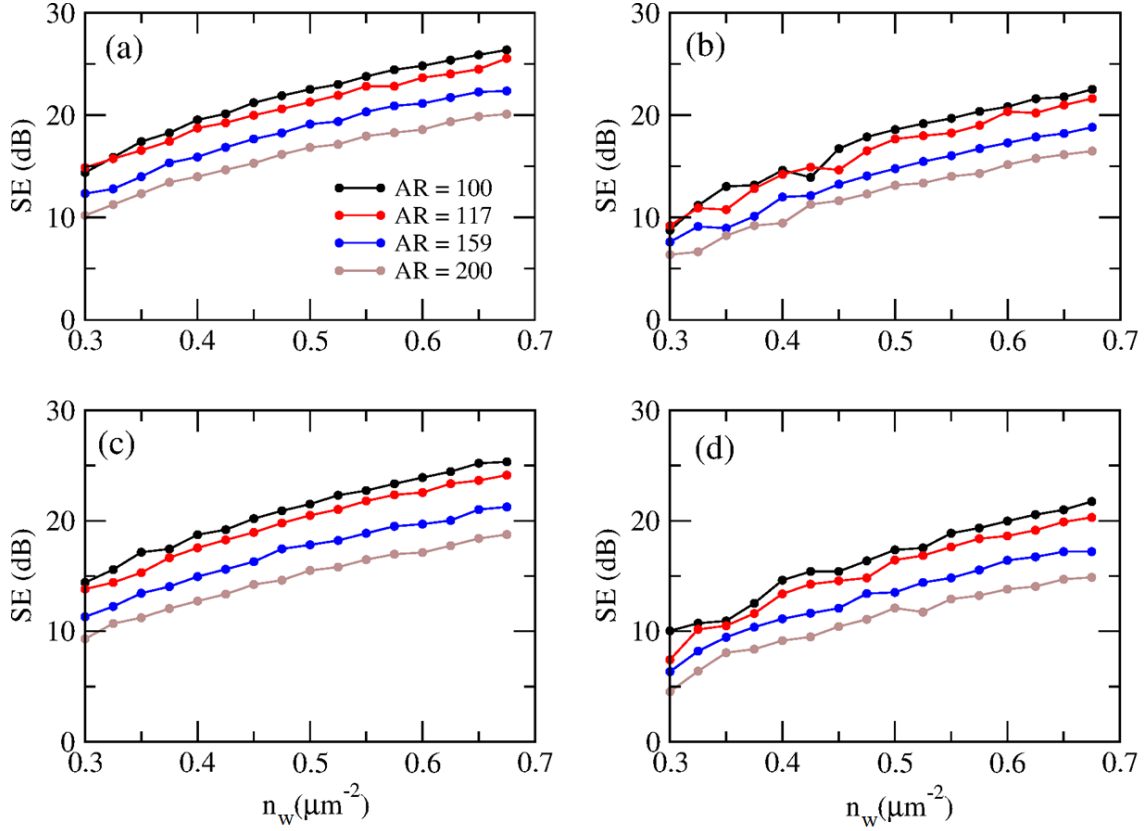
Figure 3.7: Average EMI SE (dB) as a function of density n_w in units of nanowires per μm^2 for various nanowire aspect ratios ($AR \equiv AR_O = 100 - 200$). Each data point is averaged across 10 random NWN samples with a particular density n_w. All systems are 30×30 μm in dimensions. The top panels (a,b) exhibit the results of NWN TCE devices produced from Ag nanowires, while the bottom panels (c,d) display the results of Au nanowires. The EMI SE as a function of density n_w is plotted in the left panels (a,c) for standard random NWNs, while the right panels (b,d) are for transparent grid-pattern NWNs. The transparent grid NWNs were constructed using a 3×3 grid just as in Figure 3.1. Reproduced from Ref. [97] with permission from the Royal Society of Chemistry.

(a)

$n_w = 0.4\ \mu m^{-2},\ n_c = 0$

$\langle R_s \rangle = 36.21 \pm 4.42\ \Omega$

$\langle AF \rangle = 0.11$

(b)

$n_w = 0.35\ \mu m^{-2},\ n_c = 0.05\ \mu m^{-2}$

$\langle R_s \rangle = 43.61 \pm 2.88\ \Omega$

$\langle AF \rangle = 0.10$

(c)

$n_w = 0.3\ \mu m^{-2},\ n_c = 0.1\ \mu m^{-2}$

$\langle R_s \rangle = 63.74 \pm 7.32\ \Omega$

$\langle AF \rangle = 0.09$

(d)

$n_w = 0.2\ \mu m^{-2},\ n_c = 0.2\ \mu m^{-2}$

$\langle R_s \rangle = 175.19 \pm 42.34\ \Omega$

$\langle AF \rangle = 0.06$
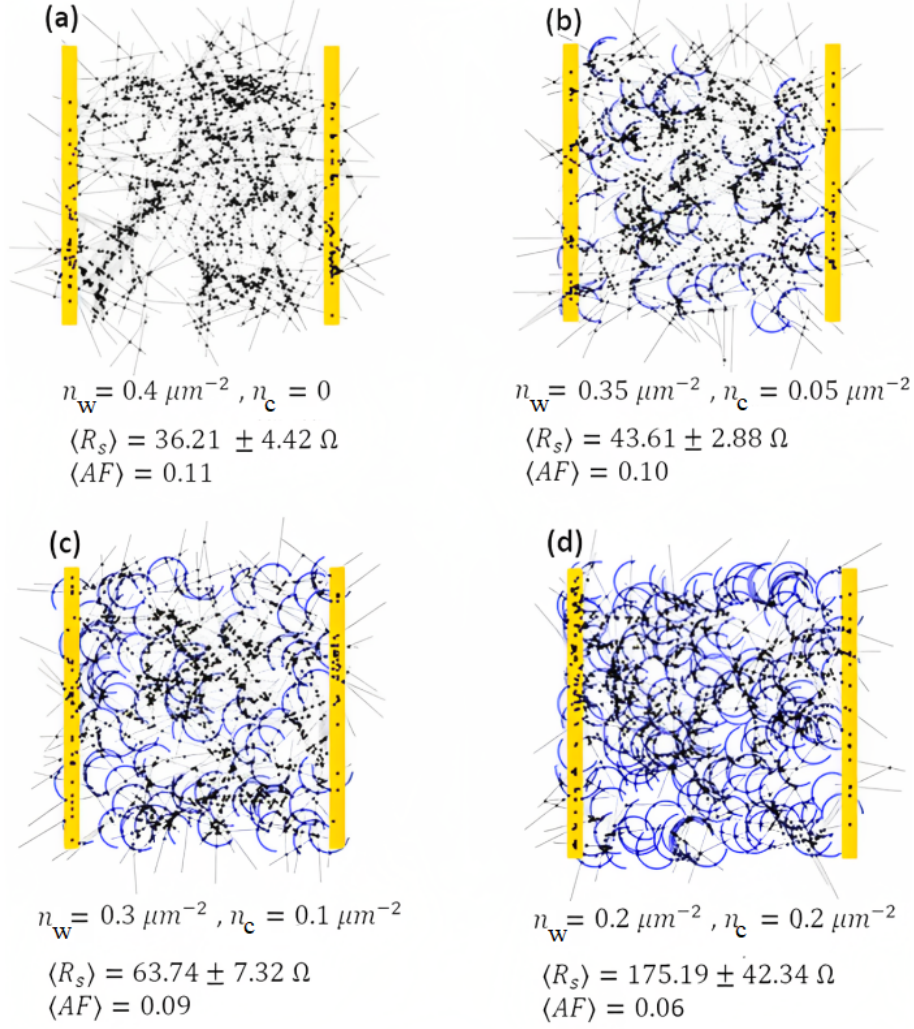
Figure 3.8: Purely straight and hybridised straight/curved Ag NWNs. Grey and blue segments depict nanowires that are either straight or curved, respectively, and black circles indicate where the wires intersect. Golden vertical lines depict metallic electrodes that are connected to a current source (not shown). All systems are 30×30 μm in dimensions. The length of the straight nanowires and the arc length of the curved nanowires are fixed to $L_w = 7$ μm. The network diagrams are only a snapshot of an ensemble of 10 NWNs whose corresponding mean $\langle R_s \rangle$ and $\langle AF \rangle$ are displayed in each panel. The standard deviation associated with R_s is also provided, while the standard deviation associated with AF is on the order of 10^{-4} for all instances investigated. n_w and n_c stand for the densities of straight and curved nanowires, respectively. (a) NWN comprised of only straight Ag nanowires ($n_w = 0.4$ μm^{-2} and $n_c = 0$). (b–d) Ag hybridised NWNs where n_c is increased (n_w decreases) in such a way as to maintain the total density of network constant at 0.4 μm^{-2}. Densities are in units of number of nanowires per μm^2. Reproduced from Ref. [97] with permission from the Royal Society of Chemistry.
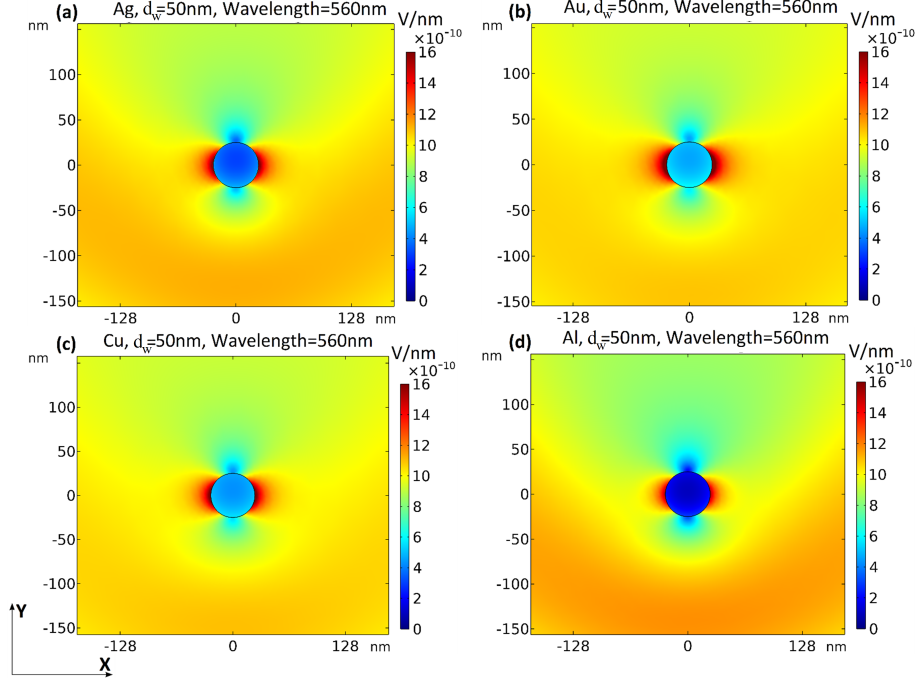
Figure 3.9: Electric field variation across the circular cross-section of a nanowire in the xy plane. The nanowires are composed of (a) Ag, (b) Au, (c) Cu, and (d) Al, and d_w = 50 nm. A λ = 560 nm plane wave with $\hat{y}$-axis propagation and two perpendicular polarizations is used to illuminate the cylinder with its axis aligned along the $\hat{z}$-axis. The strength of the electric field (V/nm) computed by averaging two perpendicular polarizations is shown in the colour bar. Reproduced from Ref. [97] with permission from the Royal Society of Chemistry.

Ultimately, in this analysis, one needs to quantify how much light a solid nanowire cylinder, made of a metallic material, scatters. Figure 3.9 exhibits the electric field scattering planar profiles for λ = 560 nm, which are calculated employing COMSOL Multiphysics® software [110]. We detect an increase in optical attenuation and greater scattering electric field as a consequence of the heterogeneous distribution of the local electric field around the nanowire circular cross-section, except for Al in which this phenomenon results from applied electrical dipole resonance [205]. Depending on the material composition, shape, size, and dielectric environment of the nanowire, this phenomenon can occur when the nanowire is smaller than the wavelength of the incoming light [206]. In the case of the Al nanowire, when an external electric field causes electrons to be displaced in response, the polarization of negative and positive charges on each side of the nanowire results in a zero-field electric

field, which cancels out any external field that could be present within the conductor. The polarizability of the material influences both the dipole moment's orientation and the dipole strength of this dipole moment [207]. COMSOL Multiphysics® software [110] was used to perform further optical cross-section calculations on a 3D finite Ag straight and curved nanowire with d_w = 50 nm and L_w = 7 μm and illustrated in Figure 2.12. According to Figure 2.12 (d), curved and straight Ag nanowires exhibit no substantial difference in optical extinction characteristics. Nonetheless, curved nanowires do impact the network area fraction as demonstrated in Figure 3.8.

3.4   Summary

This chapter concludes with a comprehensive discussion of the electro-optical modelling of metallic NWNs that could be employed as transparent conductors. We have created a robust computational framework to estimate the sheet resistance, optical transmittance, and electromagnetic interference shielding performance of various NWN designs, including random NWNs, transparent grid-patterned networks, and NWNs with monitored angular nanowire orientation. We found that the conduction and optical characteristics of the films can be modified by adjusting the geometrical factors associated with device structure, such as the grid-pattern network, coupled with the relevant network parameters, such as the aspect ratio and area fraction. In particular, the nanowire alignment can be used as a further degree of freedom to alter the device's total current flow and FOM. Two approaches were used to compute the optical response properties: MLST [107–109] and FEM implemented using the RF module (wave optics) in the COMSOL Multiphysics® software [110]. The approaches were established in complete concordance with one another and were able to capture the electromagnetic scattering characteristics of metallic nanowires in their entirety. We have observed a clear trade-off when adopting grid-pattern networks as opposed to standard random networks, whereby optical transmittance is increased at the expense of higher

resistances.

The investigation of EMI SE has revealed that the configuration of the device's structure, specifically the grid-pattern design, is a critical factor in determining the degree of shielding effectiveness. Hence, through the manipulation of the grid-pattern design, the shielding effectiveness of the apparatus can be accurately regulated to fulfil distinct electro-optical prerequisites. To clarify, it is possible to customise the efficacy of electromagnetic interference EMI shielding by modifying the grid-pattern design to attain the intended level of attenuation based on specific electro-optical circumstances. These methodologies will enable us to investigate the electro-optical properties of nanowire materials as thin metallic films as a tunable test platform prior to device manufacturing in the lab.

To conclude, the electro-optical computational methodology used in this work has been employed in past works conducted in the group and its output has been compared with experimental results and other prominent works found in the literature. Sheet resistance values have been compared with experimental results as discussed in [144]; an extensive literature gathering was conducted by Manning et al. [98] and contrasted with the results this computational methodology obtained, with remarkable agreement in terms of orders of magnitude (see also Figure 1.6). Manning et al. also investigated the electro-optical properties of Cu NWNs experimentally and computationally [84]. The same computational tools were adapted to carry on our last works published in [97, 106]. This confirms that the computational tools and models we used to describe the electro-optical responses in NWN systems are consolidated and are capable of providing results comparable with experimental and other computational findings in the literature.

Chapter 4

Thermo-Electro-Optical Properties of Seamless Nanowire Networks

Preamble

This chapter is based on Esteki et al. "Thermo-electro-optical properties of seamless metallic nanowire networks for transparent conductor applications" published in Nanoscale [106].

4.1 Introduction

Besides the standard junction-based NWNs studied in the previous chapter, we adapted our computational framework to investigate the electro-optical (and thermal) properties of another complex network material named seamless NWNs that also exhibit optimum TCE features. A seamless NWN is a structure comprised of nanowires without touching point connections, resulting in a continuous and unbroken network configuration. Its unique characteristics, including high conductivity and surface area-to-volume ratios, make it a prospective contender for a wide variety of nanotechnology applications. Using in-house computational implementations and an electrothermal model developed in COMSOL Multiphysics® software [110], we have done in-depth computational research to examine the thermo-electro-

optical properties of seamless NWNs and comprehend their geometrical characteristics in this chapter. Using Ohm's law in conjunction with Kirchhoff's circuit laws, sheet resistance calculations were carried out for a random planar resistor network that map the connectivity of the seamless NWN and compared to those produced using COMSOL Multiphysics® software [110]. Ag, Au, Al, and Cu nanowires are the materials of choice in this study for evaluating the transparent conduction performance of these systems. We have investigated a vast array of tuning factors, such as the network area fraction (AF), the width-to-depth aspect ratio ($AR_\blacksquare = W_w/D_w$), and the length of the nanowire segment. As will be introduced later, note that the cross-section surface shape of nanowires in seamless NWNs can also be squared/rectangular, for this reason, the AR subscript has been changed accordingly. We produced FOM (optical transmittance/temperature versus sheet resistance) and temperature profile distributions to characterise the performance of real-world transparent conductors idealised with seamless NWNs. Our investigation focused on the thermo-electro-optical responses of the seamless NWNs and the examination of many regulating parameters based on system design considerations in order to shed light on how to improve the electrical transport, optical qualities, and thermal management of these technologies.

As mentioned before, TCEs are critical elements of a variety of thermo- [208, 209] and optoelectronic [120] devices. NWNs comprised of metal nanowires have attracted significant interest due to their excellent electrical/thermal conductivities, optical transmission, and mechanical strength [65, 66, 73]. Much research has been conducted on random percolative NWNs generated with diverse metal nanowire materials [28, 29, 66, 73, 186, 187]; nonetheless, the contact between individual nanowires increases the equivalent network sheet resistance (R_s) [78, 83, 84, 210]. To mitigate the influence of the interwire junction resistances, the literature specifies a number of processing techniques for enhancing the junction conduction qualities, such as plasmonic welding [211, 212], mechanical pressing [77, 213, 214], and thermal annealing [215, 216]. Despite intensive efforts, the improvement potential of junction resistances is limited, and there is no standard for improving junction resistance

levels [83]. One option is to totally change the network architecture over the standard random NWN while retaining the connection and functionality that serve as the foundation of any percolative complex system. Lately, continuous metal networks, also known as nano-based crack templates with seamless connections [217], have been presented as a viable replacement to standard random NWNs. Metallic seamless NWNs are commonly manufactured using lithographic methods such as phase shift lithography [218, 219], crackle lithography [220, 221], nanoimprint lithography [219, 222], soft lithography [219, 223], and photolithography [219, 224]. Compared to standard disordered NWNs, nano-cracked seamless networks offer a few distinct benefits [122]. The transparency and sheet resistance of seamless NWNs can be modulated through multiple factors. Several factors can be considered to modify the electrical properties of a wire mesh, such as adjusting the wire width, varying the thickness of the metal employed, manipulating the mesh geometry, and utilising metals with distinct resistance values. For example, Figure 4.1 (a) presents a seamless NWN made of silicon nanowires for high-performance photodetector applications [81, 220]. In Figure 4.1 (b), we see a cutaway of the seamless NWN analysed herein that was created in a computer simulation. The inset provides information on the geometry of the nanowire segments assumed to have a rectangular cross-section, defined by their depth (D_w) and width (W_w). Subsequent sections will delve deeper into the technical aspects and specifications of these networks.
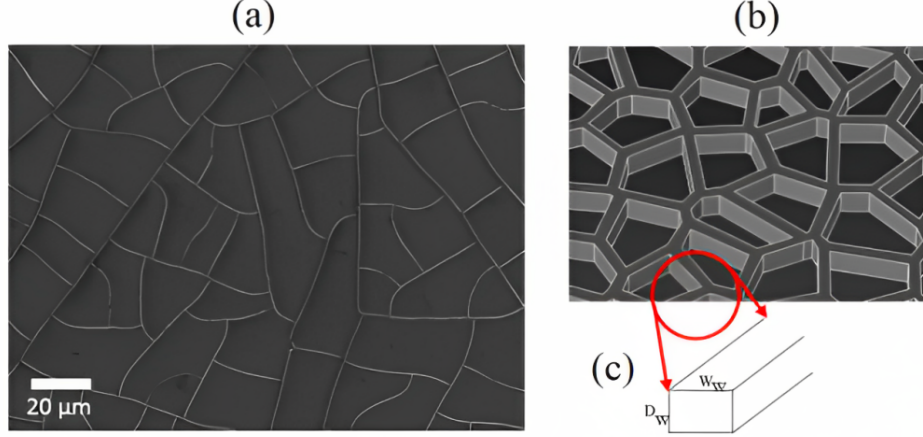
Figure 4.1: (a) An experimental SEM image of a silicon seamless NWN [81]. (b) A NWN structure created from a Voronoi diagram imported into the COMSOL Multiphysics® software simulations for this investigation. The nanowire segment has a rectangular cross-section with the dimensions D_w and W_w reflecting the channel's depth and width, respectively (see inset on panel (c)). Panels (b,c) were reproduced from Ref. [106] with permission from the Royal Society of Chemistry.

These seamless characteristics typically boost the active percolative route fraction of the network, hence decreasing the sheet resistance and enhancing the light transmittance by allowing light to enter the empty regions between the created cracks or voids. The optimal sheet resistance and optical transmittance values for TCE-based designs have been documented in the literature to be $R_s \sim 10~\Omega/\square$ and $T_{op} \sim 90\%$ in the visible wavelength range [198]. However, it should be noted that the range of sheet resistance values is dependent on the specific application for which the TCE will be utilized [97,111]. Thermo-electro-optical efficiency of cracked seamless NWNs is dependent on a number of design variables, such as the network material's geometry, the length of the nanowires (L_w), the network density (n_w) defined as the number of nanowires per unit of area, the network area fraction (AF), and the aspect ratio ($AR_\blacksquare$) defined as the width (W_w) divided by the depth (D_w) of the channel cross-sectional structure [84,97,98,121,143,163]. Note that for a standard NWN, $AR_\bigcirc = L_w/d_w$ can be expressed as the ratio of nanowire length (L_w) to diameter (d_w) as defined in Chapter 3. However, for a seamless NWN, $AR_\blacksquare = W_w/D_w$ can be defined as the ratio of nanowire width

(W_w) to its depth (D_w) considering a rectangular shaped nanowire channel. Other intrinsic properties relevant to this study, the thermal conductivity (k_{cond}) and emissivity (ϵ_{radi}) as well as heat transfer (h_{conv}) coefficients are crucial to characterize thermal transport throughout the network [128, 225, 226]. The R_s relies on the contact resistance between the network material and the device terminals as well as the inner nanowire resistances determined by $R_{in} = \rho L_w / A$, where A is the channel cross-sectional area, L_w is the channel length segment, and ρ is the material resistivity [96–98]. The optical transmittance of seamless NWNs is also dependent on the network AF and the corresponding optical extinction efficiency Q_{ext} as defined in Equation (2.8). It is challenging to verify the collective influence of such a high-dimensional variable phase space on the thermo-electro-optical characteristics of extremely disordered materials since one cannot depend on translation/rotational symmetry principles and nonlinear phenomena typically do play a role. It is known that the AF acts as a geometrical correlation parameter between the electrical resistance and the optical transmission of the material, resulting in a trade-off nonlinear relationship [96, 98]. So, a FOM assessment, often shown as a T_{op} against R_s graph, is necessary for characterising the impact of geometrical factors and inherent raw material qualities on measuring the electro-optical efficiency of NWNs. Ag, Au, Cu, and Al have all been studied in relation to their FOM of typical random NWNs, with Ag being shown to exhibit superior performance across a range of n_w and AF [29, 97, 187, 227].

In addition to their use in applications requiring an electro-optical response, metallic NWNs are also put to use as transparent heaters in places like displays and smart windows, where defogging or temperature management is crucial [55]. As a result, high-voltage and high-temperature settings pose challenges to the thermal stability of metallic NWNs [86]. An ideal NWN is that it should exhibit a uniform temperature profile throughout the network while being resistant to thermal shocks caused by high heating rates that could otherwise disrupt the system's electrothermal processing and equilibrium temperature [55, 129]. Because of the high temperatures concentrated at certain points in the wire segments, a network

can fail if the temperature distribution is not sufficiently uniform. Thus, it is crucial to forecast device performance by calculating the local current density and thermal pathways by evaluating the spatial electrical and thermal processes across the network. The spatial pattern of self-heating and hotspot clustering in complex materials can be captured using a number of existing high-resolution imaging techniques, such as thermoreflectance [129, 141] and electrical mapping [140]; however, such measurements are restricted to evaluating the local average temperatures of the networks. The localised temperature distribution of individual nanowire channels is therefore very challenging to obtain experimentally at nanometer precision [127–129, 141, 228]. Zeng et al. [128] conducted a study on the electrothermal properties of nanoscale systems by analyzing the current density and temperature distributions in continuous nano-crack networks made of Ag. The results of their study revealed significant temperature differences within the network, which could potentially lead to the failure of a junction due to electronic migration processes that are heat-assisted. While seamless networks of nano-cracks have been widely studied through experimentation [127–129, 228–233], progress in the theoretical and computational aspects of this field has been limited. This is due to several computational challenges, such as the need to explore a large parameter phase space, integrate the device with other circuit components, and customize raw materials for specific applications [122, 128, 234].

In this chapter, we outline the findings of an extensive computational study into the thermo-electro-optical characteristics of template-based metallic networks incorporating seamless junctions formed from a variety of materials such as Ag, Au, Al, and Cu. We developed a FOM analysis by tuning a wide range of variables relating to the geometrical aspects of the systems, such as the D_w, W_w, and L_w of the nanochannels, as well as the n_w, the nanochannel AR$_\blacksquare$ = W_w/D_w, and the AF, to establish the electro-optical properties of such networks. Nanowire segments with randomly linked ends are what we call "nanochannels" in a seamless NWN, where they form a percolative complex network. Calculations of optical extinction efficiency are performed using FEM in COMSOL Multiphysics® [110], whereas R_s values for

resistive circuit networks are produced employing the simplified MNA [97, 101, 144, 162] as described in Chapter 2. Our computational methodology demonstrates that template-based metallic nanowire networks outperform standard random NWNs in terms of electro-optical performance. COMSOL Multiphysics® software [110] was used to create electrothermal computations to evaluate the current density and temperature profile distributions with nanoscale precision at various voltage levels. Current density hotspots have been detected in some portions of the network, primarily at sufficiently acute/thin nanowire junctions, where mobile electrons are squandering energy. When we apply a bias voltage to these networks, our thermoelectric model reveals that the resulting spatial temperature distribution follows a Weibull distribution, implying widespread electrical involvement from all segment channels. It is critical to understand and forecast the possibility of melting/failure of metallic materials (Ag, Au, Al, Cu) in an electrical operation, hence we have evaluated maximum temperature values for several seamless network scenarios made of target metallic components.

4.2   Methodology

We used a two-step procedure to model the thermo-electro-optical characteristics of metallic seamless NWNs. To begin, we analyzed the network's electro-optical performance by creating a computational toolset that concurrently produces electrical sheet resistance and optical transmission data. In this stage, we developed custom scripts in Python [159] with the help of relevant network-based packages and tools including Shapely [235], Networkx [236], and Scipy [237] to represent the spatial structure of the disordered seamless NWNs. This is mostly a computational study, however, the design of the examined seamless NWNs is driven by the experimental works of Sheerin et al. [81, 220] and several other discoveries focusing on seamless or patterned network materials [129, 230, 238–240]. For computational studies, a virtual representation of a NWN can be created by means of applying image processing techniques to NWN micrograph images, which enables the extraction of nodal,

connectivity, and segment information [144]. This information is then used to construct a mathematical graph that accurately represents the NWN in a virtual form. The same connectivity and graph labelling can be applied to planar seamless NWNs. Several works [81, 128,241] have analysed experimental images of seamless NWNs, and one can visually identify that the topology of these networks can be emulated using a tile pattern similar to Voronoi diagrams. Although image processing approaches are useful for generating precise geometries of NWN-based systems, their sample size limitations prevent them from being used in studies based on ensemble analysis and the calculation of average and standard deviation values. We improved the generation of virtual seamless NWNs by taking into account the fact that their network topology is a Voronoi tessellation with a random distribution of centre points as shown in Figure 4.2. The Voronoi diagrams are a spatial partitioning technique that utilises the proximity of points to divide space into regions. This method has proven to be a useful tool for representing the structural intricacies of diverse complex systems, including biological cells [242] and fractured soils [243]. Voronoi cells, which are constituted by geometric configurations of points, are circumscribed by Voronoi edges, a set of line segments that establish the limits between neighbouring cells. Voronoi diagrams possess the ability to not only depict the arrangement of points but also the interconnections among them, thereby rendering them a potent tool for generating intricate network systems. By utilizing Voronoi diagrams, researchers can gain insights into the properties of these systems and better understand their connectivity and spatial features. In this fashion, Voronoi cells can be interpreted as plane-partition polygon objects with channel-like line segments arbitrarily dispersed inside a device surface area (see Figure 4.2).
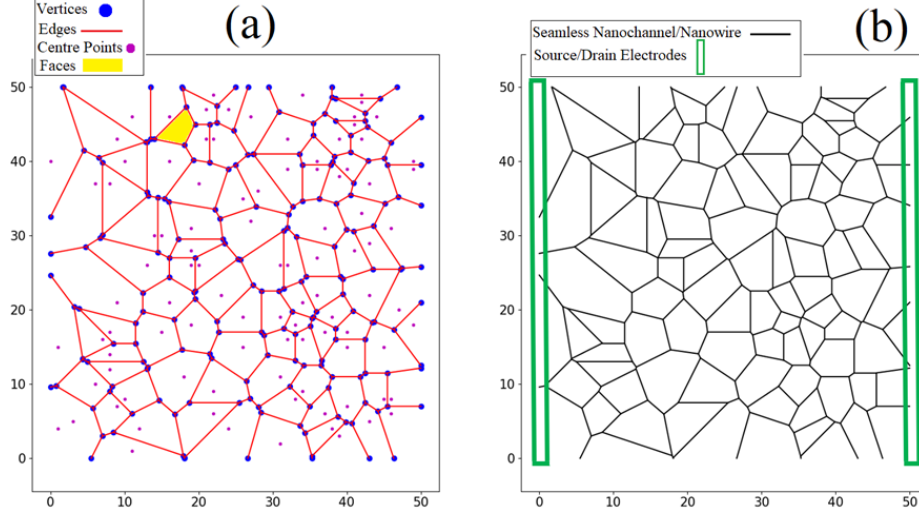
Figure 4.2: (a) Planar Voronoi graph created by our computer scripts. The graph consists of purple dots which represent Voronoi center points that are randomly placed over a certain area. The blue dots indicate the vertices that connect multiple line segments, also known as edges or ridges, shown as red lines. In the main text, a ridge is referred to as a conducting nanochannel or a nanowire segment. The closed polygons or cells are also known as regions or faces; we coloured one of them yellow for the sake of visualization. (b) The Voronoi diagram in (a) is transformed into a seamless NWN device in which the internal Voronoi pattern is coupled to source/drain electrodes (vertical green rectangles). This transformation creates a NWN mapped from a Voronoi diagram. The black line segments are interconnected seamless nanochannels or nanowire segments. The device size is 50×50 μm, the density of the network is set to $n_w = 0.05$ nanowire segments per μm^2, and the nanowire segments have a mean length of $\langle L_w \rangle = 7$ μm. Reproduced from Ref. [106] with permission from the Royal Society of Chemistry.

As seamless NWNs lack interwire contact junctions, the sheet resistance of the device is determined by extrinsic and intrinsic factors such as geometrical features, the resistances of the individual nanochannels (R_{in}) and the interfaces between the nanochannels and the two-terminal source and drain electrodes (R_c or contact resistances). $R_{in} = \rho L / A$ provides the resistances of the inner nanochannels, and R_c can be approximated as $\langle R_{in} \rangle$ if one assumes that the contact resistance is not sufficiently different from the already existing metallic inner resistances of the network. While contact resistances between the seamless NWN and the electrodes are prone to variations owing to variables such as the electrode material, the existence of interface defects, and the details of the device fabrication, $R_c \sim \langle R_{in} \rangle$ is to be

expected as we prioritise the use of metallic materials. Characteristics of ascribed resistivity used to simulate metallic elements of seamless networks include ρ_{Ag} = 19.23 nΩm [225], ρ_{Au} = 25 nΩm [244], ρ_{Al} = 62.5 nΩm [245], and ρ_{Cu} = 25.51 nΩm [246]. As a result, the whole network topology is converted into a resistive circuit network with inner/contact resistances that link a complex group of voltage nodal points that constitute a Voronoi diagram. This circuit data is described by Ohm's and Kirchhoff's circuit laws, which can be numerically calculated for each voltage node to obtain the network's total sheet resistance R_s. Earlier publications in the group [101, 142–144, 163] and previous chapters in this thesis provide the crucial details and mathematical explanations of our technique employed in this research. The optical response parameters are obtained through a simulation of the dispersed electric field around a nanoscale object in a 2D space domain by solving Maxwell's differential equations. This is accomplished using FEM in COMSOL. The main outcome of our COMSOL Multiphysics® modelling [110] is the estimation of the optical efficiency coefficients described as $Q_{ext} = Q_{abs} + Q_{sca}$ in which Q_{ext}, Q_{sca}, and Q_{abs} are the extinction, scattering, and absorption coefficient efficiencies, respectively. The optical COMSOL Multiphysics® [110] analysis in this chapter was based on our previous work [97] (see Chapter 3) that estimated the optical spectra of a cylinder cross-section of a nanowire under direct light incidence. The results obtained from this analysis were compared to those obtained using MLST for an infinite cylinder [107, 108]. MLST and our optical COMSOL Multiphysics® [110] simulation were found to agree quite well (see Figure 3.2). In this analysis, we focus on seamless NWNs, which differ from conventional cylinders in that their cross-section is of squared or rectangular shape. Thus, we have used the same method to calculate the total effective optical spectra of this targeted study, which is an object with a squared/rectangular surface area in a channel-like nanowire form. Chapter 2 contains detailed information on the COMSOL Multiphysics® [110] modelling configurations, including the background electromagnetic wave, PECs, scattering boundary conditions, and meshing of the object. Additionally, it provides relevant information on Maxwell's electromagnetic wave equations that

need to be solved to perform the simulation. In this optical modelling study, the refractive index information for various materials such as Ag, Au, Al, and Cu, has been used. The refractive index information is wavelength-dependent and has been taken from Johnson and Christy [172] built in COMSOL Multiphysics® software [110] material database [110]. The surface of a nanochannel placed within a PML and surrounded by air is illuminated by a perpendicularly incident linearly polarized plane wave. The electromagnetic responses in 2D were computed using the RF module of COMSOL Multiphysics® software [110]. The incident light is assumed to be a plane wave propagating in space with two orthogonal electromagnetic wave polarizations. It is essential to point out that one distinction between the seamless NWNs in this chapter and the standard random NWNs in the previous chapter is that the seamless networks' nanochannel segments are square-shaped (not cylindrical). Segments of nanochannels are envisioned to be generated cuboids on a surface. The full-wave electromagnetic solutions were computed over the wavelength ranging from 150 to 1200 nm for square-shaped nanochannels with side lengths of D_w = 30 nm and D_w = 50 nm. The optical Q_{ext} is inserted into the Equation (2.8) to calculate the optical transmission of a seamless NWN. In Equation (2.8), Q_{ext} is the optical extinction efficiency factor obtained by COMSOL Multiphysics® [110] simulations and AF is the area fraction of a seamless film. AF represents the proportion of the film's surface area that is covered by the nanochannels and can be calculated using a mean-field approach by $AF = n_w \times \langle L_w \rangle \times W_w$, where n_w is the density of nanochannels, L_w is the average length of the nanochannels, and W_w represents the width of the nanochannels. However, because we know the pixel and segment-wise length information after we image-generate the seamless NWNs, we were able to compute the accurate area fraction coverage, preventing its overestimation. Thus, a FOM is created by averaging the electrical sheet resistance and the optical transmission of a collection of seamless NWNs with known and regulated geometrical features (such as nanochannel density, nanochannel aspect ratio, etc.).

As a second stage in our simulations, we delved at a more comprehensive 3D model of

Joule heating in a seamless NWN composed of Ag, Au, Al, and Cu. The variation in current density throughout the network is the reason for local heat transfer, and our study aims to better understand this mechanism. Using the COMSOL Multiphysics® software [110] with the "electric current" (EC) and "heat transfer in solid" (HT) modules coupled, we derived the thermo-electrical characteristics of the complex seamless NWNs. An initial 2D Voronoi diagram was constructed in DXF Voronoi pattern generator software [247], and then all of its points and dimensions were imported into SOLIDWORKS 2020 CAD design software [182] to be used in the development of the 3D random metallic seamless films. With a given AR■ $= W_w/D_w$, we get a 3D Voronoi network as shown in Figure 4.1 (b). The seamless 3D NWN structure is imported into COMSOL Multiphysics® software [110], where the software's meshing boundary conditions and physical laws are utilized to construct an electrothermal model. To ensure that the network remains stable and not suspended, a 3D PET substrate is designed and used as the base for constructing the seamless network. The model incorporates a two-terminal configuration with electrodes built from the same metallic material as the seamless NWN architecture so that a DC bias voltage can be applied to electrically probe the network. By elevating the applied bias voltage, it is anticipated that the seamless NWN structure will produce Joule heating induced by the current. Then, heat transfer equations are solved by taking into account the principal intrinsic parameters that govern heat transfer mechanisms in solids, such as the thermal conductivity (k_{cond}), the convection (h_{conv}), and the emissivity (ϵ_{radi}) coefficients of all components included in the model, along with the contact thermal conductance set in place between the seamless NWN and the substrate. It has been noted by earlier works that the heat transport equations take into consideration three mechanisms [128, 129]: (i) heat conduction between the seamless film and the substrate, (ii) heat convection between the seamless film and the ambient air at room temperature, and (iii) heat radiation released from the seamless film to the environment. Therefore, it is possible to express the power balance equation for a solid object as follows [55, 128, 129, 248]

$$
\begin{cases}
mc_p \frac{dT}{dt} = Q_{Joule} - (Q_{conv} + Q_{radi}) \\[2mm]
Q_{Joule} = \sigma_{cond}|\nabla V|^2 + \nabla \cdot k_{cond}\nabla T \\[2mm]
Q_{conv} = A h_{conv}(T - T_{amb}) \\[2mm]
Q_{radi} = A\delta\epsilon_{radi}(T^4 - T_{amb}^4)
\end{cases}
\tag{4.1}
$$

in which T denotes the temperature with T_{amb} referring to the ambient temperature. m and c_p are the mass and specific heat at constant pressure of the material (Ag, Au, Al, Cu) forming the NWN, respectively, t represents the time, and $\delta = 5.67 \times 10^{-8}$ Wm^{-2}K^{-4} is the Stefan Boltzmann constant [55]. The terms 'cond', 'conv', and 'radi' are used as individual subscripts to denote the modes of heat transfer: conduction, convection, and radiation, respectively. The symbols used to represent different physical quantities are as follows: σ_{cond} represents electrical conductivity, V represents voltage and A stands for the area over which heat is transferred. The terms Q_i show the power contributions associated with each mode of heat transfer, $i = cond, conv, radi$. Additionally, there is a term Q_{Joule} which indicates the power associated with Joule heating, which is the conversion of electrical energy into heat energy within a conductor. Note we adjusted the emissivity coefficients to zero for the duration of our simulation since we detected no discernible influence on the overall results. All the parameters that are utilized in our COMSOL Multiphysics® electro-thermal model are reported in Table 4.1.

Table 4.1: Electro-thermal coefficients employed in our COMSOL Multiphysics® simulations for several seamless NWN materials made of Ag, Au, Al, and Cu. k_{cond} and σ_{cond} are the thermal and electrical conductivity, respectively.

Material	k_{cond} (Wm^{-1}K^{-1})	σ_{cond} (Sm^{-1})
Ag [225]	325	5.20×10^7
Au [244]	200	4.00×10^7
Al [245]	120	1.60×10^7
Cu [246]	65	3.90×10^7

The thermal properties of metallic nanostructures are influenced by a range of factors,

such as intrinsic material and geometric characteristics as well as environmental conditions. Therefore, to establish a reference point for heat transfer convection between the NWN and the environment, the benchmark value for free convection of air [249], $h_{conv-air}$ = 10 Wm^{-2}K^{-1} was selected [250]. Furthermore, the contact thermal resistance, which is the inverse of contact thermal conductance, between the NWN and the substrate was set to 10^{-8} Wm^{-2}K^{-1} [251]. In our approach, we considered the effect of temperature on both thermal conductivity and electrical resistivity, while applying different voltages. To incorporate these effects, we used the Wiedemann-Franz law [131] relationship; this law states that the ratio of electronic thermal conductivity to electrical conductivity in a metal is directly proportional to the temperature. Further details on this relationship will be discussed in the following sections.

The present study employs a semi-classical (phenomenological) methodology to describe the electro-optical-thermal characteristics of Voronoi-based seamless NWNs made of metallic materials. Despite the complex nature of these materials, which consist of multiple nanowire segments linked in a Voronoi fashion, we were able to investigate their collective behaviour as networks at the microscale level (50×50 μm). Moreover, considering that the fabrication process of such networks usually does not rely on high-precision instrumentation methods to achieve precise nanoscale architectures, their structure may also contain numerous imperfections and defects impacting the charge carriers' trajectories. Under these conditions, we can assume that the elastic mean free path is smaller than the dimensions of the network device in which many elastic scattering events can occur while the electrons propagate through its structure. This is the case in which the charge carriers travel diffusively through the network and at elevated temperatures in which the phase coherence length is sufficiently small typically. Our methodology, however, carriers a semi-classical aspect in which nanoscale effects can be incorporated in an effective way by not using conductivity values estimated from the classical Drude model; we take these values from measurements done in nanowires whose values deviate from the classical Drude model, giving a semi-classical (and phenomenologi-

97

cal) aspect to our description. This is how we included, in an effective way, effects associated with the characteristic nanoscale dimensions of the individual nanowires. Yet, it is important to stress that the NWNs here studied are also complex systems in the microscales as all nanowires integrate to form complex interconnects that propagate currents in their intricated network frame.

4.3 Results and Discussion

4.3.1 Spatial, Electrical, and Optical Characterization

This study uses Voronoi diagrams, as shown in Figure 4.2, to describe the spatial organisation of NWN topologies that are seamless. Polygons constructed according to the Voronoi pattern criteria enclose a random distribution of centres (purple circles) as shown in Figure 4.2 (a). Figure 4.2 (b) depicts this conceptualization, in which the ridges of the polygons are regarded to be nanowire segments that join together to create a random seamless NWN structure. The size of the NWN devices under study are 50×50 μm, and the source and drain electrodes, shown as green rectangles in Figure 4.2 (b), are spaced 50 μm apart to allow for electrical interrogation of the network. The rectangular or square cross-sectional area of a nanowire can be utilized to calculate the $AR_\blacksquare = W_w/D_w$, a metric that can be used to uniquely identify a seamless NWN. It is important to keep in mind that our seamless NWNs are created inside a set device area, such as 50×50 μm, which describes common sizes for such devices. As a consequence, the average ridge length of the network shortens as the number of polygon centres grows. Figure 4.3 displays the outcomes of statistical analysis and topological characterisation done on an ensemble of computer-generated seamless Voronoi NWNs. For a set of 1000 Voronoi NWN samples produced with 500 centres, histograms of perimeter, ridge lengths, and polygon area were obtained. Each Voronoi sample was limited to a square with dimensions of 50×50 μm. To describe the electrical properties of finite-size Voronoi networks, we can use these histograms to learn about their typical length and area scales.

It is important to note that the y-axes of the histograms are labelled as 'density', indicating that the probability density function at each bin is normalized to one upon integration. In line with previous studies, we confirmed that the distribution of polygon areas is well described by a two-parameter Gamma distribution [252, 253]:

$$f(x, \alpha, \beta) = \frac{\beta^\alpha x^{\alpha-1} e^{-\beta x}}{\Gamma(\alpha)} \tag{4.2}$$

in which x is a random variable, $\Gamma(...)$ is the Gamma function, α is the shape parameter, and β is the inverse of the scale parameter. Through nonlinear curve fitting analysis, we obtained the values of α and β for the two-parameter Gamma distribution in Figure 4.3 (c) to be $\alpha = 3.66$ and $\beta = 0.7$. Figure 4.3 (d) illustrates how the average ridge length fluctuates as a function of the number of centres employed to construct the Voronoi NWNs. Since our seamless Voronoi networks are finite, their average ridge length decreases as more centre points are dispersed across the 50×50 μm region, and this will influence the computed resistance and optical transmission values, as we shall illustrate in the subsequent sections. The trend in Figure 4.3 (d) (red dashed line) is a fitted power law $N_c = C\langle L \rangle^\gamma$, where N_c corresponds to the number of centres, $C = 1800$ and $\gamma = -1.95$.
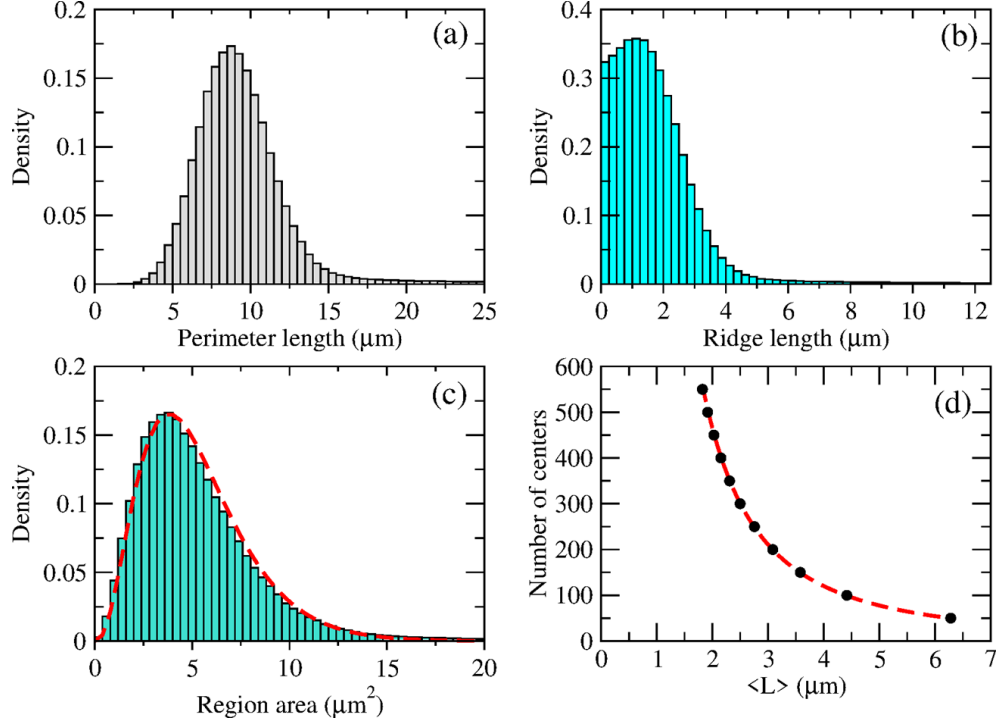
Figure 4.3: A spatial characterisation was performed on an ensemble of Voronoi NWNs, each of which had a randomly generated centre point from which the ridges/polygons were produced. Panels (a,b,c) exhibit histograms of perimeter length, ridge length, and region area, respectively, for 1000 Voronoi NWNs produced with 500 randomly distributed centres. All Voronoi diagrams were constructed inside a squared area of 50×50 μm in size. The y-axes of the histograms are expressed in terms of 'density', which indicates that the integration over the probability density function at the bin is normalized to one. Panel (d) shows the variation in the number of Voronoi center points (N_c) with respect to the average ridge length, $\langle L \rangle$. Dashed lines on panels (c,d) relate to fittings of: (c) a Gamma distribution as given in Equation (4.2) in the main text and (d) a power law given by $N_c = C \langle L \rangle^{\gamma}$. The fitting parameters are α = 3.66 (Gamma distribution shape parameter), β = 0.7 (Gamma distribution inverse scale parameter), and the power law parameters are C = 1800 and γ = -1.95. Reproduced from Ref. [106] with permission from the Royal Society of Chemistry.

First, we must determine the optical extinction coefficient efficiency, Q_{ext}, which defines the intrinsic optical characteristics of the nanowires forming the networks, before we can demonstrate the FOM trade-offs in seamless NWNs. The spectral extinction data for four types of nanowire materials made of Ag, Au, Al, and Cu were generated using COMSOL Multiphysics® software [110] and shown in Figure 4.4. The incident wavelengths were varied between 200 nm to 1250 nm, and the orientation of the nanowires was adjusted so that the main axis of the square-shaped nanowires was perpendicular to the direction of the incident

wave. We have calculated and determined the average values of two perpendicular polarizations of the incident beam. One polarization had an electric field oriented perpendicularly to the axis of the square-shaped nanowire, while the other polarization had an electric field parallel to the same axis. The curves are distinguished by length scales and cross-sectional regions that are distinct: the cross-sectional area of square-shaped nanowires is given by $A_\blacksquare = W_w{}^2 = D_w{}^2$, while that of circular (cylindrical) nanowires is given by $A_\bigcirc = \pi(d_w/2)^2$, where d_w is the diameter of the circle. To study the light-scattering effects resulting from an increase in the thickness of the nanowires, we maintained two pertinent length scales ($D_w = W_w$ and d_w) at a fixed value of 30 nm and 50 nm. By doing so, we obtained optical extinction efficiencies that allowed us to visualize the impact of widening the thickness of the nanowires. The dimensionless optical extinction efficiencies over the whole range of interest not only exhibit different behaviours largely owing to the alteration of the raw materials but also varies with regard to length scales and nanowire form. In general, square-shaped nanowires exhibit greater optical extinction efficiency than cylindrical ones. This characteristic will have significant implications when computing the optical transmission of seamless NWNs.
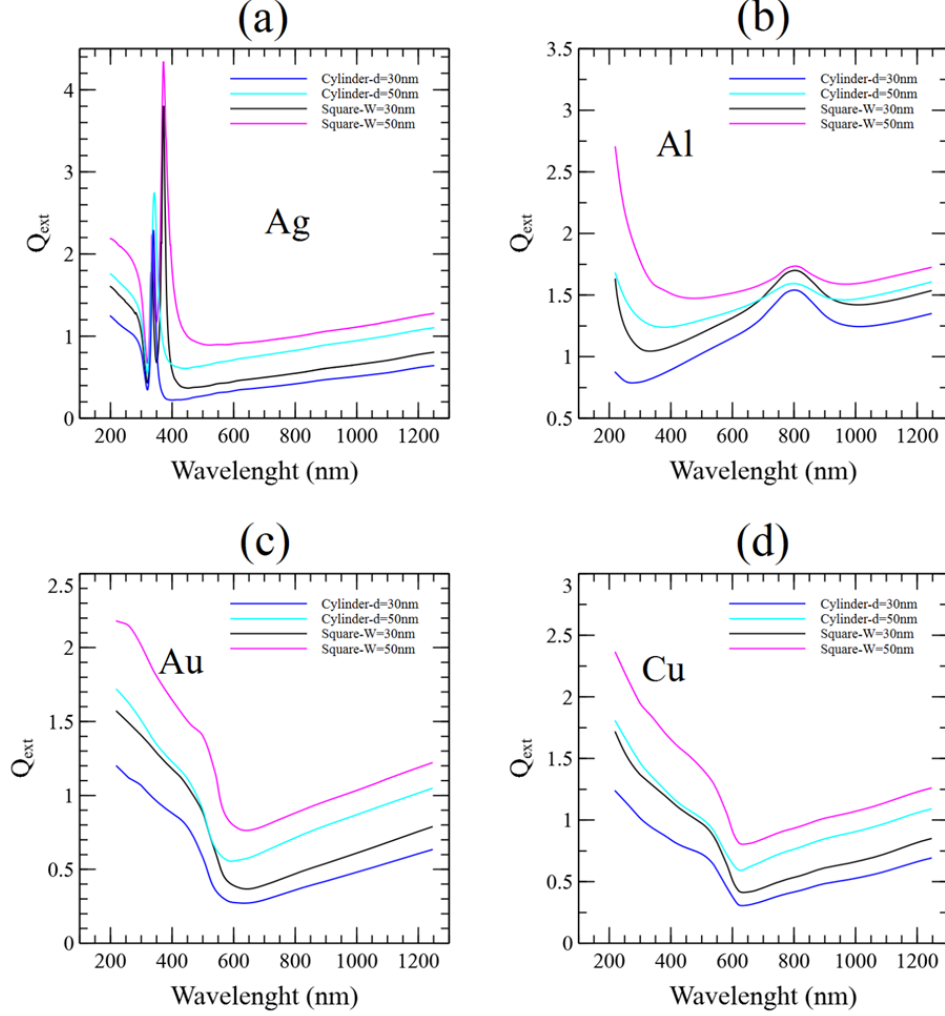
Figure 4.4: Wavelength dependent optical extinction efficiency factors (Q_{ext}) over the wavelength range of 200 nm to 1250 nm obtained for distinct metallic materials: (a) Ag, (b) Al, (c) Au, and (d) Cu. These outcomes were calculated using COMSOL Multiphysics® software [110] with the electromagnetic wave's propagation along the $\hat{y}$-axis, and its polarizations are along the $\hat{x}$- and $\hat{z}$-axis. Nanowires of different cross-sectional geometries were modelled: a square-shaped nanowire of width $W_w = D_w = 30$ nm and 50 nm (shown as W or D without subscript "w"), and a cylindrical nanowire of diameter $d_w = 30$ nm and 50 nm (shown as d without subscript "w"). Reproduced from Ref. [106] with permission from the Royal Society of Chemistry.

We used COMSOL Multiphysics® software [110] to calculate the planar profiles of electric field scattering, which are displayed in Figure 4.5. The calculations were carried out for a square-shaped nanowire made of different metals and exposed to a light wave with a wavelength of $\lambda = 550$ nm propagating along the $\hat{y}$-axis. Two normal polarizations were con-

sidered, one along the $\hat{x}$-axis and the other along the $\hat{z}$-axis. The squared edges undoubtedly contribute to the nanowire's electric field dispersion. Because the electric field is proportional to the charge density, nanochannels with sharp vertices exhibit powerful electric fields at the tips, indicating high charge densities. As a result of the inhomogeneous distribution of the local electric field surrounding the nanowire square cross-section, we observe an enhancement in optical dispersion and a stronger scattering electric field, except for Al [205], which is formed via induced electric dipole resonance. The electric field within an Al nanowire is negligible due to the polarization of positive and negative charges on opposite sides of the nanochannel in response to the external electric field. This polarization creates an internal field that counteracts the external one inside the conductor. The strength of this dipole moment and its generation is influenced by the material's polarizability, as well as the shape, size, and dielectric environment of the nanowire [254]. Furthermore, a comparison of the relative electric field strengths between square and circular nanowire cross-sections shows a field enhancement of around 1.2. This enhancement helps explain why the calculated optical extinction efficiencies for squared-shape nanowires are considerably higher [255] as shown in Figure 4.4. In summary, the electric field intensity distribution surrounding a square cross-section, referred to as a square nanochannel, exhibits higher values when compared to a circular cross-section, referred to as a cylinder nanowire, for nanomaterial structures composed of Ag, Au, Al, and Cu.
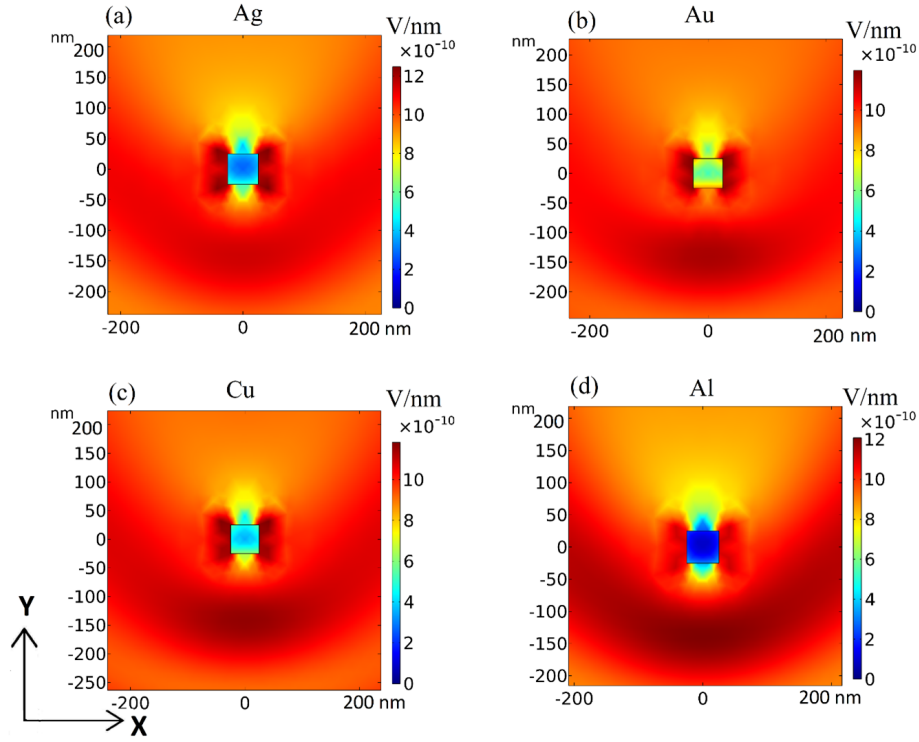
Figure 4.5: Electric field distribution around a square cross-section in the xy plane of a nanowire made of four different materials Ag, Au, Cu, and Al, each having equal edge sizes of $D_w = W_w = 50$ nm. The square geometry is illuminated by a plane wave of $\lambda = 550$ nm wavelength, with the direction of propagation along the $\hat{y}$-axis and two normal polarizations along the $\hat{x}$- and $\hat{z}$-axis. The colour bar in the figure represents the electric field intensity (in V/nm) simulated in COMSOL Multiphysics® software [110] based on the average of two electric field polarizations perpendicular to each other. Reproduced from Ref. [106] with permission from the Royal Society of Chemistry.

Figure 4.6 demonstrates the optical transmission versus sheet resistance trade-off for seamless NWNs produced as Voronoi diagrams. Each point on the panel was computed for a given number of centre points randomly dispersed throughout a $50 \times 50\,\mu\mathrm{m}$ surface area, and this result was produced for an ensemble of seamless NWNs comprising 50 samples. The value of N_c was varied from 25 to 300 in steps of 25, with a descending order of resistance values. Two materials, Ag and Al, were analyzed to compare their FOM. The Voronoi networks were transformed into a weighted mathematical graph consisting of voltage nodes and edges, with the weights representing the inner wire resistances. To overcome the dependency on the contact resistances, the extended electrodes shown in Figure 4.2 (b) were

designated to the node in the Voronoi structure that was the farthest to the left (source) and the node that was the farthest to the right (drain). To determine the overall sheet resistance of a network, the "resistance distance" associated with the graph is calculated. The optical transmittance is determined using Equation (2.8), where the value of Q_{ext} is obtained from Figure 4.4 and is adjusted to the visible wavelength of 550 nm. The area fraction is obtained from the top-view Voronoi images generated by the computer simulation. Our analysis shows the estimated trends in terms of design variables. Seamless networks made of materials with less resistance and greater cross-sectional areas are ideal candidates for electrical conductors. For example, square-shaped Ag NWNs with a width of W_w = 50 nm reveal resistances of $\langle R_s \rangle < 250$ Ω. They also exhibit relatively high optical transmission, with the lowest estimated at $\approx 97\%$ Reducing the width of the Ag squared nanowires to W_w = 30 nm boosts the optical transmission to $\approx 99\%$. Al seamless NWNs branch at greater resistance ranges and weaker optical transmission values than Ag seamless NWNs due to the material's high resistivity and high extinction features. Our model, however, still predicts optical transmissions over 90% for all analysed parameters, providing quantitative confirmation that seamless NWNs are excellent candidates for transparent conductor applications.
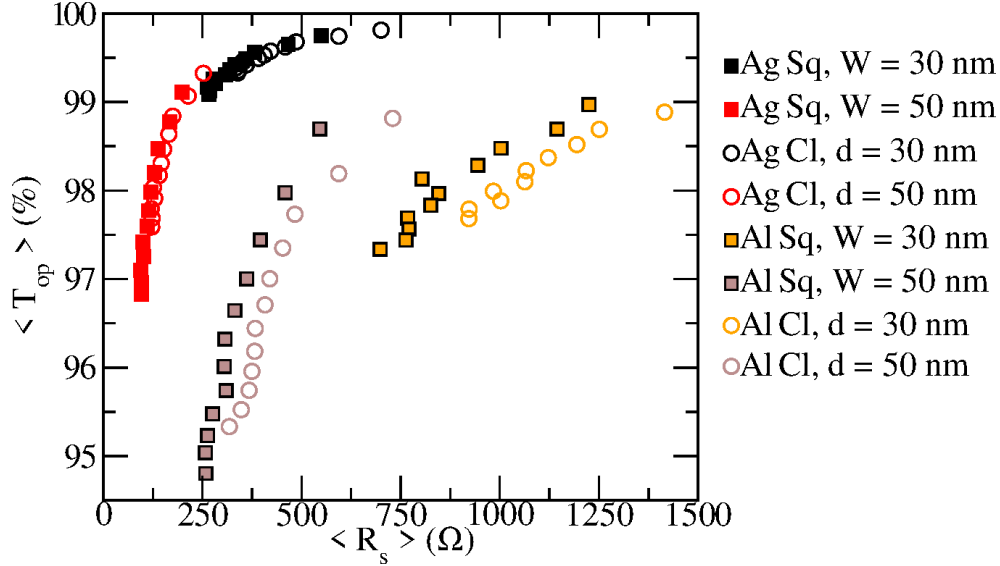
Figure 4.6: FOM for ensembles of Voronoi seamless NWNs of various geometries and materials that relate the average optical transmission to the average sheet resistance. The averages were calculated using 50 Voronoi NWN samples as an ensemble for Ag and Al nanomaterials. The Voronoi ridges have either a square (Sq, filled square symbols) or a circular cross-section (Cl, hollow circular symbols). As shown in the legend, 30 and 50 nm were two distinctive ridge width dimensions that were examined. For cylindrical ridges with circular cross-sectional areas, the dimension relates to their diameter indicated by d (equivalent to previous notation as d_w) and the dimension for squared shape ridges has their depth equals to the width given by $D = W$ (equivalent to previous notation as D_w and W_w). Reproduced from Ref. [106] with permission from the Royal Society of Chemistry.

One may question, however, how seamless NWNs compare to junction-based random NWNs deposited on a surface in terms of overall performance. The latter is distinguished by a connectivity profile of interwire junctions that provide additional resistance to the overall sheet resistance. Furthermore, a portion of the wire segment in a NWN-based junction can act as a "dead end" and does not participate in the conduction process, but it does add to the total area fraction. Because of fundamental design differences in connection and nodal structure, seamless and junction-based NWNs cannot be compared directly. As a result of their transversal interwire connections, junction-based NWNs have a 3D connectivity profile. Nonetheless, qualitative comparisons can be based entirely on the normal orders of magnitude that their sheet resistances and optical transmissions can achieve. Figure 4.7 compares the electro-optical performance of two distinct NWNs, seamless and standard

junction-based. The figure illustrates the T_{op} versus R_s results for an Ag NWN device with dimensions of $20 \times 20\,\mu m$. The NWN insets correspond to snapshots of two comparable NWNs (junction-based in green and seamless in red) in terms of area fraction with nanowire's average length $\langle L \rangle$ = 4.6 μm, for the sake of visualization. For all tested examples shown in the figure, we tried to generate standard and seamless NWNs with similar geometric arrangements despite their different connection characteristics. The standard NWNs consist of cylindrical nanowires with a set diameter of d_w = 50 nm, while the seamless NWNs are comprised of Voronoi templates with square-shaped ridges of a defined depth D_w = 50 nm. Even though the projected transmittance shown in Figure 4.7 is higher for seamless NWNs due to their relatively low AF, it is worth reminding that the estimated Q_{ext} for seamless square-shaped nanowires tends to be larger than those with circular cross-sections (see Figure 4.4). Pike and Seager [151] have provided a criterion for determining the critical density of randomly oriented 2D sticks to percolate. The criterion states that a connection can be established between two sticks if their centers are within a distance L_w of each other, where L_w is the length of the sticks, and their relative direction is such that they intersect. Based on this criterion, they have derived an equation to calculate the critical density of a percolative stick network according to Equation (2.1). Hence, a standard NWN must meet this criterion for a complex system to efficiently percolate but, in a seamless NWN, there are no such constraints since the system template is already designed to percolate the electrodes. This is an additional perk of seamless NWNs compared to the standard NWNs. We can conclude that the simulation technique used in this study is effective at capturing the essential characteristics of the systems' electrical and optical responses and our simulated findings coincide with the observations provided by Kumar et al. [121] for comparison between seamless and conventional NWNs.
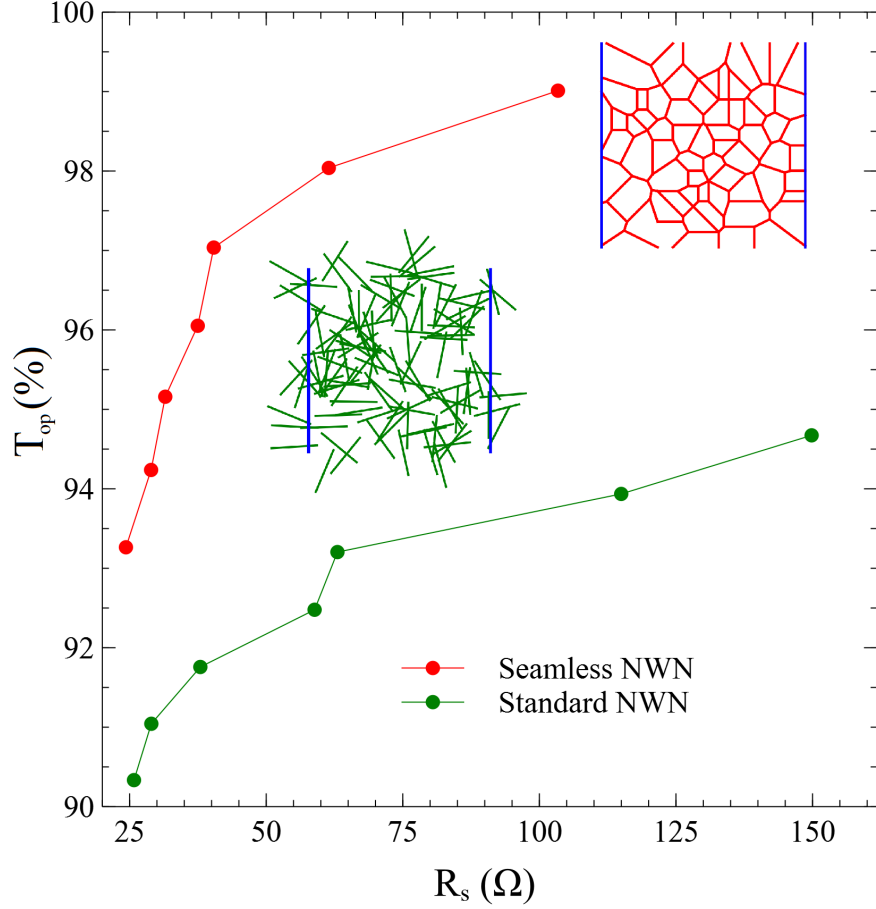
Figure 4.7: T_{op} versus R_s of seamless and standard (junction-based) NWNs made of Ag. The diameter of cylindrical nanowires for the standard NWNs is d_w = 50 nm and the depth of the nanochannel for seamless NWNs is D_w = 50 nm. The widths of the seamless NWNs are varied from W_w = 50 nm to W_w = 350 nm to alter the AF of the standard NWNs and to obtain the selection of points shown on the plot. All systems are $20 \times 20\,\mu$m in size. Each data point represents the mean of 10 samples of random spatial configurations. The junction resistance (R_{jxn}) between two nanowires in standard NWNs and the contact resistance with the source/drain electrodes (R_c) are all set to $R_c = R_{jxn}$ = 10 Ω [83]. The NWN insets correspond to snapshots of two comparable NWNs (junction-based in green and seamless in red) of nanowire's average length $\langle L \rangle$ = 4.6 μm. Reproduced from Ref. [106] with permission from the Royal Society of Chemistry.

4.3.2 Electro-Thermal Characterization

In this section, we compare the numerical findings obtained using in-house scripts to those derived utilising electro-thermal steady-state modelling in COMSOL Multiphysics® software [110]. With the help of COMSOL Multiphysics® software [110], we can investigate

additional physical quantities including temperature, electrostatic potential, and current density profiles. In this manner, the connection between the network's topology and its electric and thermal characteristics can be studied in detail. To verify that our COMSOL Multiphysics® [110] seamless NWN simulation complies with our in-house scripts that supply electrical characteristics, we estimated the sheet resistance trend at constant $AR_\blacksquare$ while altering AF, and vice versa, and compared the two techniques. This comparison is displayed in Figure 4.8, where the agreement between the two computing methods is evident.
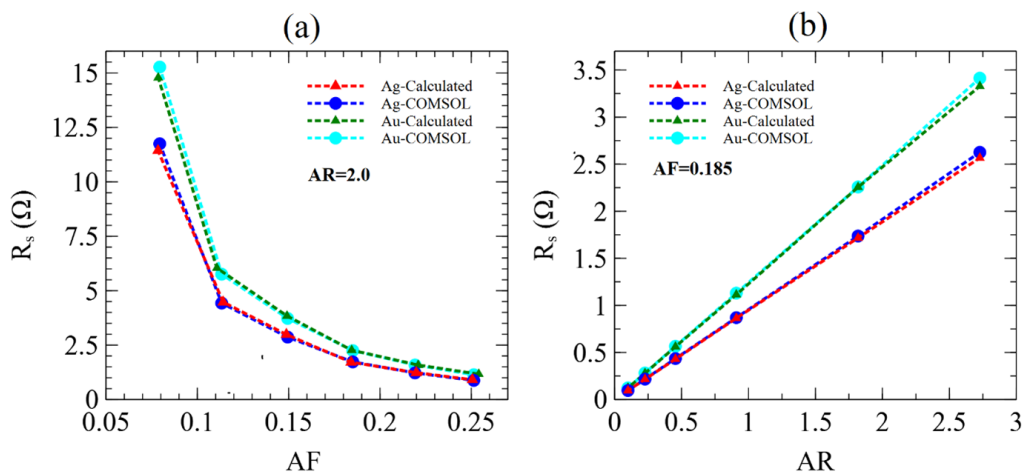
Figure 4.8: Sheet resistance (R_s) for seamless Voronoi NWNs systematically determined by (a) altering AF while maintaining AR (here $AR \equiv AR_\blacksquare = W_w/D_w$) constant, and (b) vice versa. The values were calculated using two different computational techniques: COMSOL Multiphysics® software [110] (circular symbols, designated as "COMSOL") and our own scripts based on Kirchhoff's circuit rules and circuit networks (triangular symbols, tagged as "Calculated"). Each system is $50 \times 50\,\mu m$ in size, and two different raw materials – Ag and Au – were explored. The estimated average values for the sheet resistances applying our scripts are based upon an ensemble of 10 randomly chosen spatial Voronoi configurations, but for the COMSOL Multiphysics® [110] findings, each data point was associated with a single imported CAD (computer-aided design) file. Reproduced from Ref. [106] with permission from the Royal Society of Chemistry.

Table 4.1 provides the electrical and thermal conductivity characteristics for both methods. Note that Figure 4.8 (b) demonstrates a seemingly counter-intuitive increase in sheet resistance with an increasing aspect ratio of nanowires. It is essential to point out, however, that building Voronoi networks to feed the COMSOL Multiphysics® software [110] has its

limitations, especially for Voronoi networks of limited sizes, which are the focus of this study. Figure 4.8 (b) conceals the fact that even with borders set at $50 \times 50\,\mu$m, the density (number of ridges per unit of area) of the Voronoi networks does not remain constant. Since the resulting seamless Voronoi networks get sparser in terms of ridge number and lengths, the sheet resistance similarly increases with the aspect ratio (here is $AR_\blacksquare = W_w/D_w$).

To study the effect of Joule heating and, ultimately, to map how the local current density and temperature gradient profiles in the seamless NWNs distribute under various operated voltages, we conducted the thermal characterization in conjunction with the electrical analysis utilising Wiedemann-law Franz's relationship [130, 131] that relates electrical and thermal conductivity as depicted in Figure 4.9. The Wiedemann-Franz law [130, 131] is a physical principle that describes the relationship between the thermal conductivity and electrical conductivity of certain nanoscale metal materials. Specifically, the law states that the ratio of a metal's thermal conductivity (k_{cond}) to its electrical conductivity (σ_{cond}) is proportional to the temperature (T) of the metal, and this proportionality is given by the Lorenz number ($\mathcal{L}$) and can be written as $k_{cond}/\sigma_{cond} = \mathcal{L}T$. In other words, $\mathcal{L}$ is a constant of proportionality that relates the two conductivities at a given temperature. The Lorenz number is a fundamental constant of physics that has been experimentally determined for various metals [131] and is found to be $\mathcal{L} = 2.44 \times 10^{-8}$ WΩK^{-2} [130, 131].
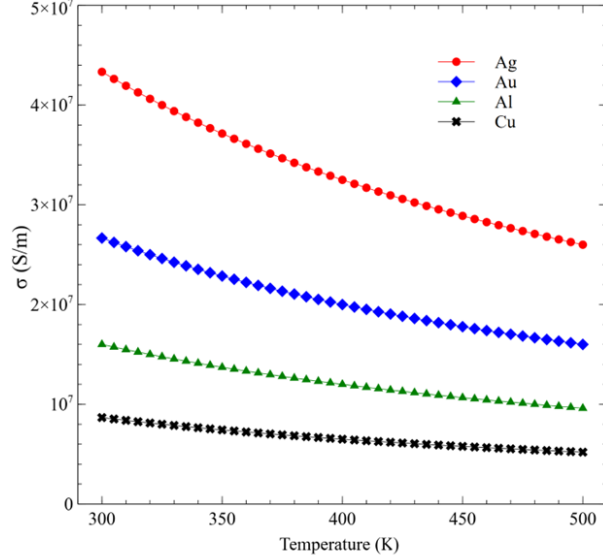
Figure 4.9: Temperature-dependent change in electrical conductivity for four metals, Ag, Au, Al, and Cu, while the thermal conductivity remains constant at the reported values in Table 4.1 for each nanowire material. The plot demonstrates how the Wiedemann-Franz law [130, 131] applies to these metals, as the ratio of thermal conductivity to electrical conductivity (Lorenz number) is proportional to the temperature for each metal as predicted by the law. Reproduced from Ref. [106] with permission from the Royal Society of Chemistry.

Figure 4.10 (a) depicts the spatial snapshot of a Voronoi diagram prepared for electrothermal modelling in COMSOL Multiphysics® software [110]. As mentioned earlier, the aspect ratio and area fraction of the networks could also be adjusted to examine the impact of network geometry on the film's response. The simulated spatial electrostatic potential is shown in Figure 4.10 (b). Electrodes having an induced voltage differential of 1.6 V are shown by the vertical lines at the network's ends. Ag nanoridges were laid down in a $50 \times 50\,\mu\text{m}$ tessellation pattern according to the Voronoi method. From 0 V (ground, left) to 1.6 V (right), the electrostatic potential is shown to increase fairly linearly along the length of the device. By adjusting the sourced voltage from 0.1 V to 4.6 V in increments of 0.5 V, the sheet resistance and average network temperature were analysed. Figure 4.11 upper panels (a,b) illustrate the sheet resistance versus applied voltage for Ag and Au seamless NWNs, respectively, with fixed $\text{AR}_\blacksquare$ = 2.0 and varied AF = 0.08 to 0.25, whereas the lower panels (c,d) illustrate the findings for fixed AF = 0.185 and varying $\text{AR}_\blacksquare$ = 0.1 to 3.0. These

111

findings are the output of a COMSOL Multiphysics® [110] calculation. Furthermore, Figure 4.12 displays the calculated sheet resistance versus applied voltage for various $AR_\blacksquare$ and AF associated with additional seamless network materials, such as Al and Cu, using the same model.
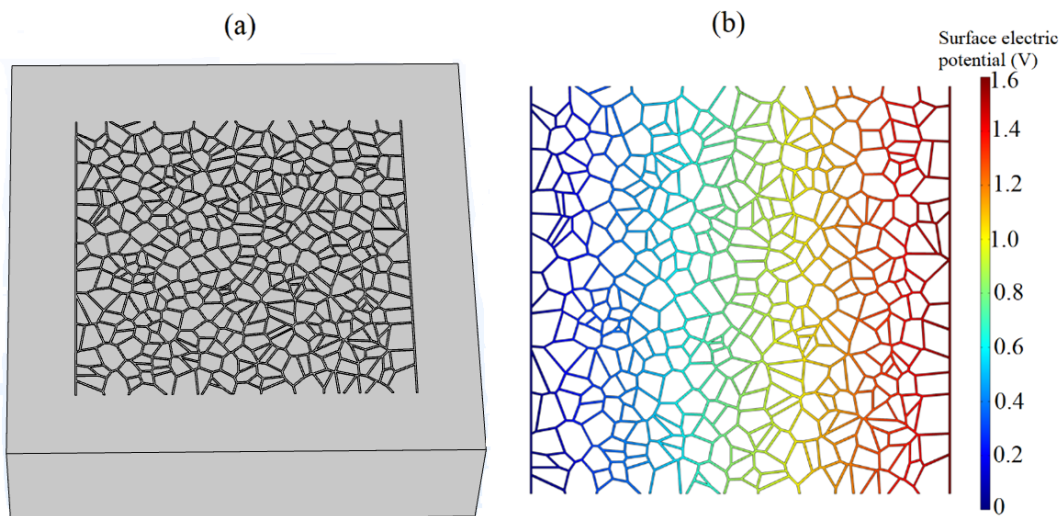
Figure 4.10: (a) COMSOL Multiphysics® software-generated [110] schematic illustration of a seamless conductive NWN model. A $50 \times 50\,\mu m$ sized Voronoi diagram is placed on a substrate (grey cuboid). (b) Calculated surface electrostatic potential with a bias voltage drop of 1.6 V established on the same seamless NWN seen in (a) with the setting that the ridges are formed of Ag material. The colour gradient illustrates a gradual increase in electric potential from the left side (represented by the dark blue colour) to the right side (represented by the red colour) of the device. This progression is determined by the nominal terminals of the device, which are represented by vertical lines located at either end of the device. The left terminal is designated as "ground", while the right terminal is designated as "source". Reproduced from Ref. [106] with permission from the Royal Society of Chemistry.

Comparing Figures 4.11 and 4.12 reveals that the sheet resistance is both thermally and electrically material-dependent under identical network design and supply voltage. Al sheet resistances range lower values (maximum values ~ 40 Ω) than Cu NWNs (maximum values ~ 80 Ω) throughout the same range of applied bias voltage, even though Cu's electrical conductivity is designed to be 2.5 times larger than that of Al (see Table 4.1). This is because Al has a thermal conductivity of around 1.8 times greater than Cu, therefore Cu seamless NWNs have a higher sheet resistance [256]. Figures 4.11 and 4.12 illustrate that

the sheet resistance (R_s) can be modified in nanostructured seamless films by a number of means, including the material's intrinsic properties, such as its k_{cond} and σ_{cond}.
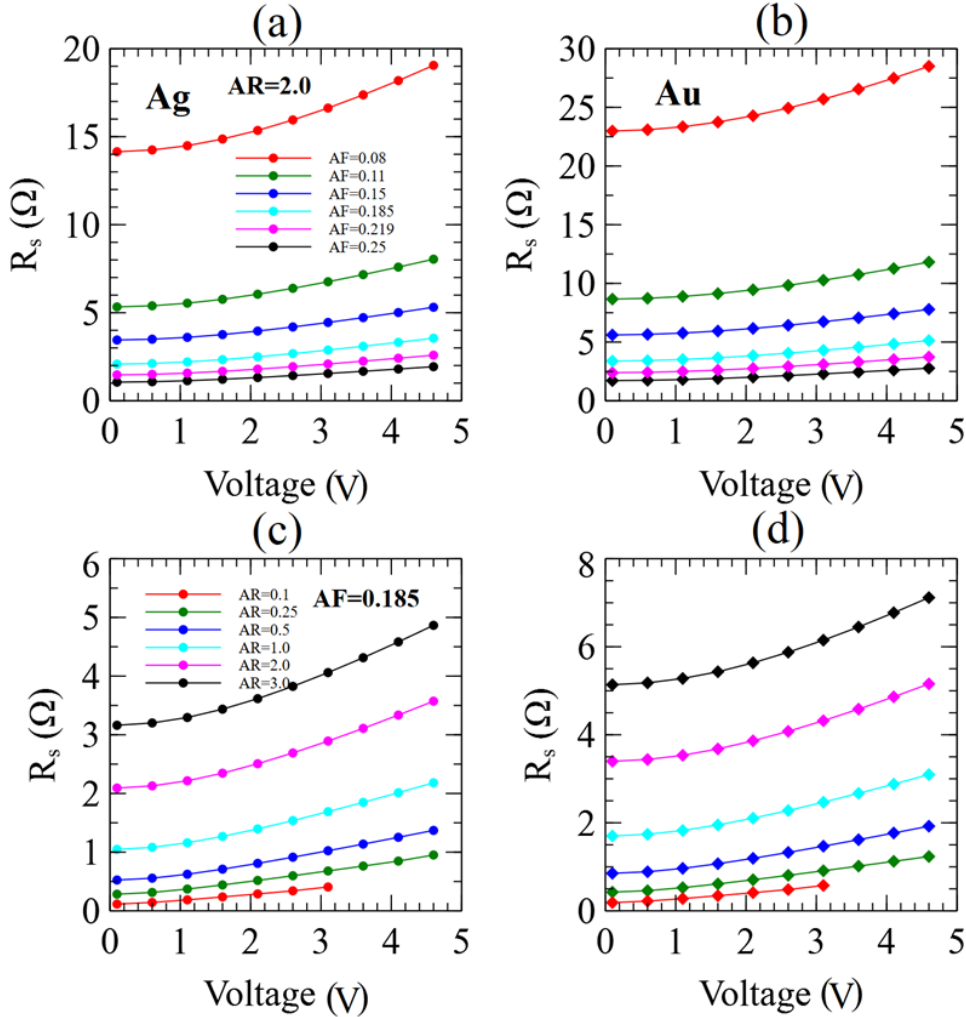
Figure 4.11: Estimated R_s versus supplied voltage obtained with COMSOL Multiphysics® software [110] for seamless NWN systems. All seamless NWNs are $50 \times 50\,\mu m$ in size. Every data point refers to a single imported seamless NWN CAD file for COMSOL Multiphysics® simulation [110]. (Top panels) R_s as a function of applied bias voltage for systems made of (a) Ag and (b) Au NWNs with fixed $AR_\blacksquare$ = 2.0 and various densities and AF values. (Bottom panels) R_s as a function of applied bias voltage for systems made of (c) Ag and (d) Au NWNs with fixed AF = 0.185 and various densities and $AR_\blacksquare$ values (here $AR \equiv AR_\blacksquare = W_w/D_w$). Reproduced from Ref. [106] with permission from the Royal Society of Chemistry.

We show that the average temperature of the NWNs can be adjusted by manipulating the same phase space parameter that affects their electrical characteristics. An electric current runs through a resistor when a voltage drop is placed across it and heat is produced from the

many-particle collisions occurring inside the conductor known as Joule heating. The resistor's temperature rises as a result and, in the case of seamless NWNs made up of many nanoscale resistors, we were able to calculate the average temperature rise over the whole network as displayed in Figure 4.13. Figures 4.11 and 4.12 paired with 4.13 illustrate the outcome of the Wiedemann-Franz law which describes how electrical conductivity changes with temperature. The Wiedemann-Franz law predicts a reduction in electrical conductivity as a function of temperature, assuming that thermal conductivity remains invariant (see Figure 4.9) [130–132, 248]. This is also a way of simulating Joule heating, the phenomenon in which current flow produces thermal energy in an electrical conductor. When current flows through a wire, a part of the electrical energy is converted into heat energy due to some resistance experienced by it, hence, heating the wire. Microscopically, this means that heat is generated when the conduction electrons transfer energy to the conductor's atoms/ions by means of collisions. In our COMSOL Multiphysics® model [110], we have assumed that the fluctuation in electrical resistivity (which is the inverse of electrical conductivity, $\rho = 1/\sigma_{cond}$) is more significant than the fluctuation in thermal conductivity with temperature changes. This assumption is supported by literature that shows that for a material such as Ag [225], within a temperature range of $50 - 300$ K, $k_{cond}(300\,\text{K})/k_{cond}(50\,\text{K}) \approx 1.6$ while $\rho(300\,\text{K})/\rho(50\,\text{K}) \approx 4.0$ [225, 244–246]. Our models of seamless NWNs exhibit sheet resistances ranging from $R_s \approx 1 - 80$ Ω by altering the NWNs' metallic composition and network/structural characteristics. Figure 4.13 depicts the network average temperature against various supplied bias voltages for seamless NWNs made of Ag, Au, Al, and Cu with AR$_\blacksquare$ = 2.0 and area fractions ranging from AF = 0.08–0.25. This finding demonstrates that with comparable device specifications and network design, Ag and Au provide greater temperature values than Al and Cu. In general, our estimated sheet resistances (see Figures 4.11 and 4.12) and network average temperatures (see Figure 4.13) are responsive to material and network arrangement, and these results are within the same orders of magnitude as earlier published studies [55, 86, 127–129, 140, 241, 257–259].
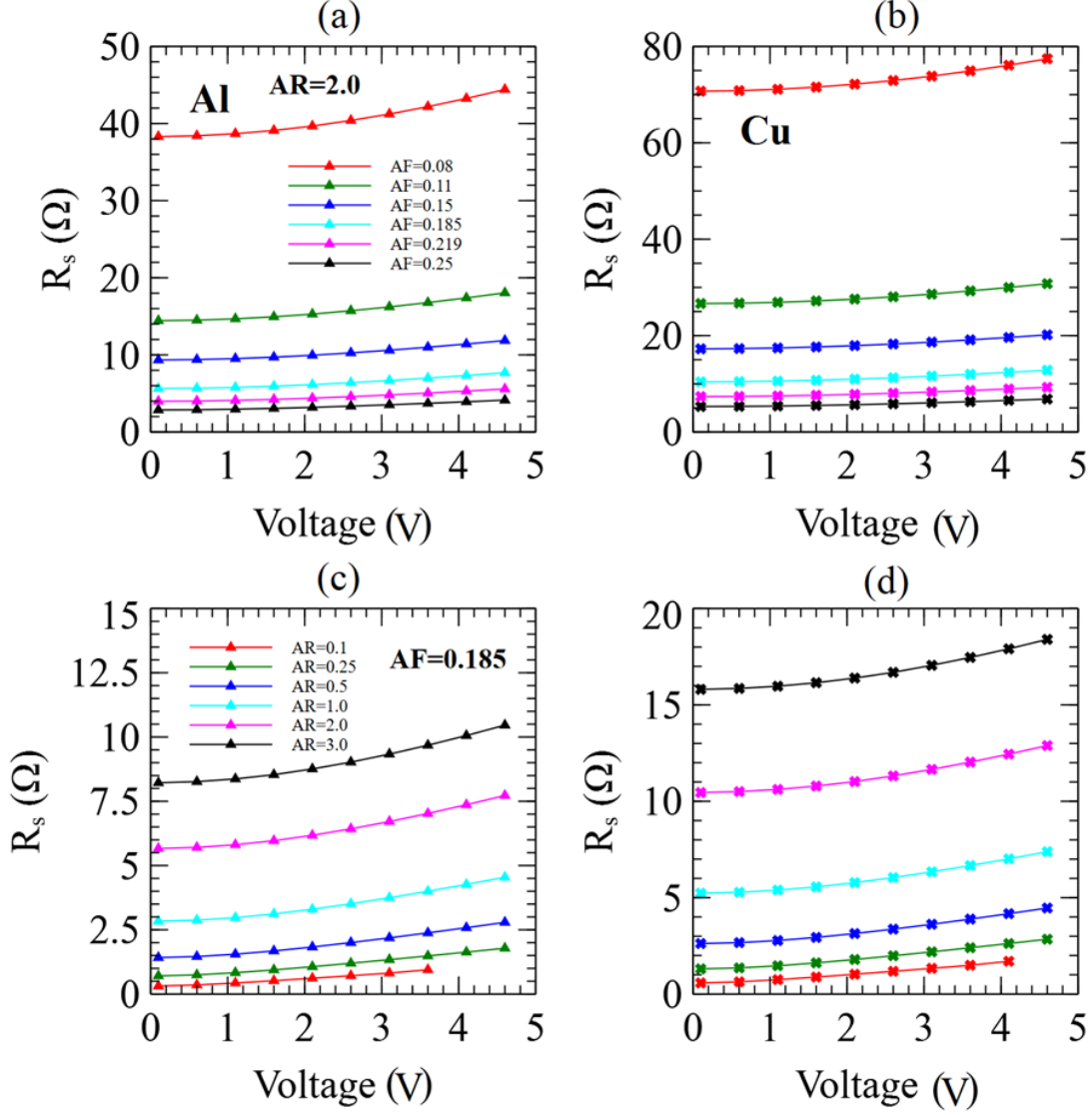
Figure 4.12: R_s versus supplied voltage obtained with COMSOL Multiphysics® software [110]. All seamless NWNs are 50×50 μm in size. Every data point refers to a single imported seamless NWN CAD design for COMSOL Multiphysics® simulation [110]. (Top panels) R_s as a function of applied bias voltage for systems made of (a) Al and (b) Cu NWNs with fixed $AR_\blacksquare = 2.0$ and various densities and AF values. (Bottom panels) R_s as a function of applied bias voltage for systems made of (c) Al and (d) Cu NWNs with fixed AF = 0.185 and various densities and $AR_\blacksquare$ values (here AR is $AR_\blacksquare = W_w/D_w$). Reproduced from Ref. [106] with permission from the Royal Society of Chemistry.

An additional aspect addressed in this chapter that affects the temperature profile distribution within the metallic seamless NWNs and, hence the sheet resistance is the contact

thermal conductance between the seamless NWN and the substrate. An important factor in the transport of heat in nanodevices is the contact/interfacial thermal resistance (the inverse of the contact thermal conductance). An in-depth understanding of nanoscale interfacial heat transport processes is essential for nanoelectronics integration [251, 260, 261]. We altered the contact thermal conductance between the metallic seamless NWN and the substrate, as shown in Figure 4.14, to examine the effect this parameter has on the sheet resistance and the average temperature across the network. In this analysis, we compared calculated findings for a few specially selected case studies, involving AF = 0.185 and 0.25 and voltages of 1.1 V and 2.6 V for Ag and Au seamless NWN nanomaterials, with $AR_\blacksquare$ = 2.0. Due to the variation in nanostructure and material manufacturing, the contact thermal conductance can differ significantly. Therefore, to maintain consistency, we selected the most common range of contact thermal conductance values reported in the literature for metallic nanowires, which is typically within the range of ~ 10^7 to ~ 10^8 Wm^{-2}K^{-1} [251, 260].
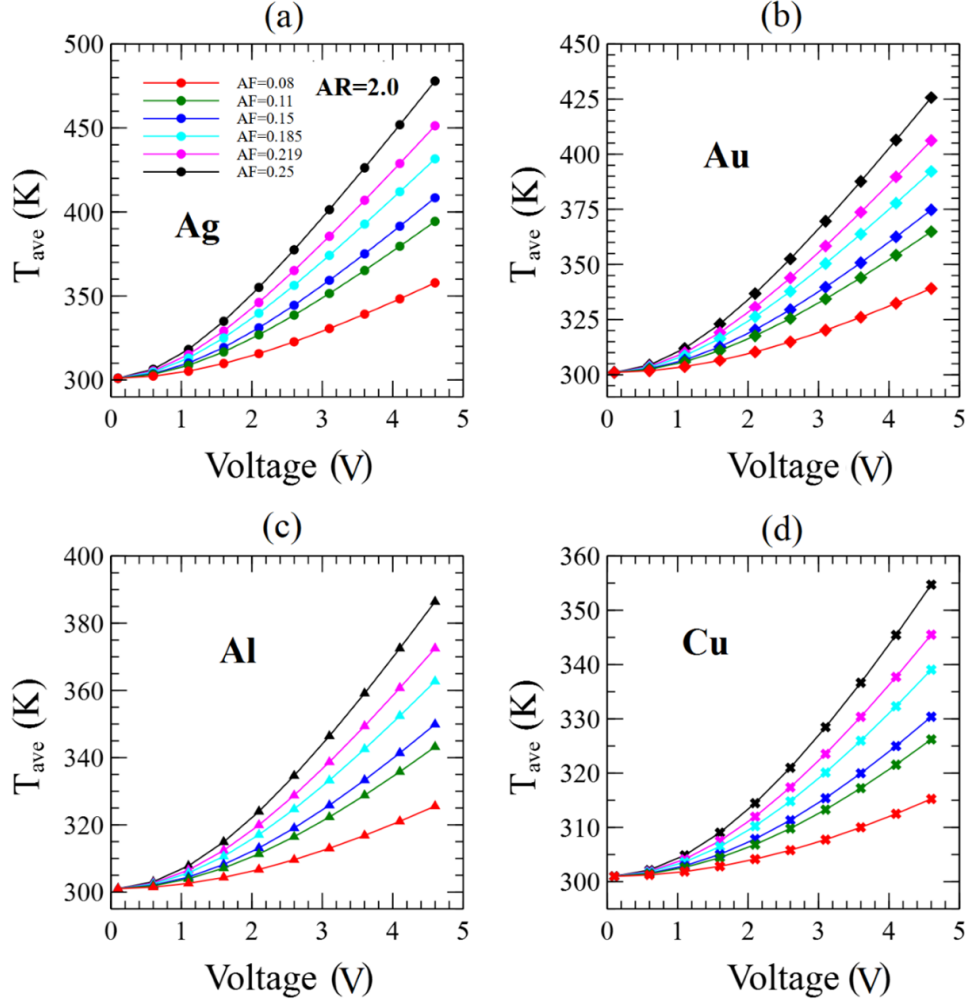
Figure 4.13: Estimated average network temperature (T_{ave}) in Kelvin (K) as a function of supplied voltage (V) for seamless NWNs made of different nanomaterials including (a) Ag, (b) Au, (c) Al, and (d) Cu. All seamless NWNs are $50 \times 50\,\mu m$ in size. Every data point refers to a single imported seamless NWN CAD file for COMSOL Multiphysics® simulation [110]. In all panels, the ridge aspect ratio was fixed at $AR_\blacksquare = 2.0$ and distinct curves refer to different area fraction values as shown on the legend in panel (a) (here $AR \equiv AR_\blacksquare = W_w/D_w$). Reproduced from Ref. [106] with permission from the Royal Society of Chemistry.

Figure 4.14 (a) and (c) illustrates how an increase in contact thermal conductivity leads to a drop in the average network temperature. According to the Wiedemann-Franz equation, it is found that the electrical conductivity increases as the temperature drops. In addition, better thermal coupling between the network and the substrate can be accomplished by raising the contact thermal conductance. Hence, the network could "cool down" due to the

optimised heat exchange. The decreased sheet resistance seen in Figures 4.14 (b) and (d) provides more evidence in favour of this interpretation. We will talk more about how disordered nanomaterials, like seamless NWNs, can display substantial pockets of heat, referred to as hotspots. In light of these results, it is reasonable to assume that the contact thermal conductance can be employed as a further regularization factor for modulating the thermal and electrical properties of seamless NWNs.
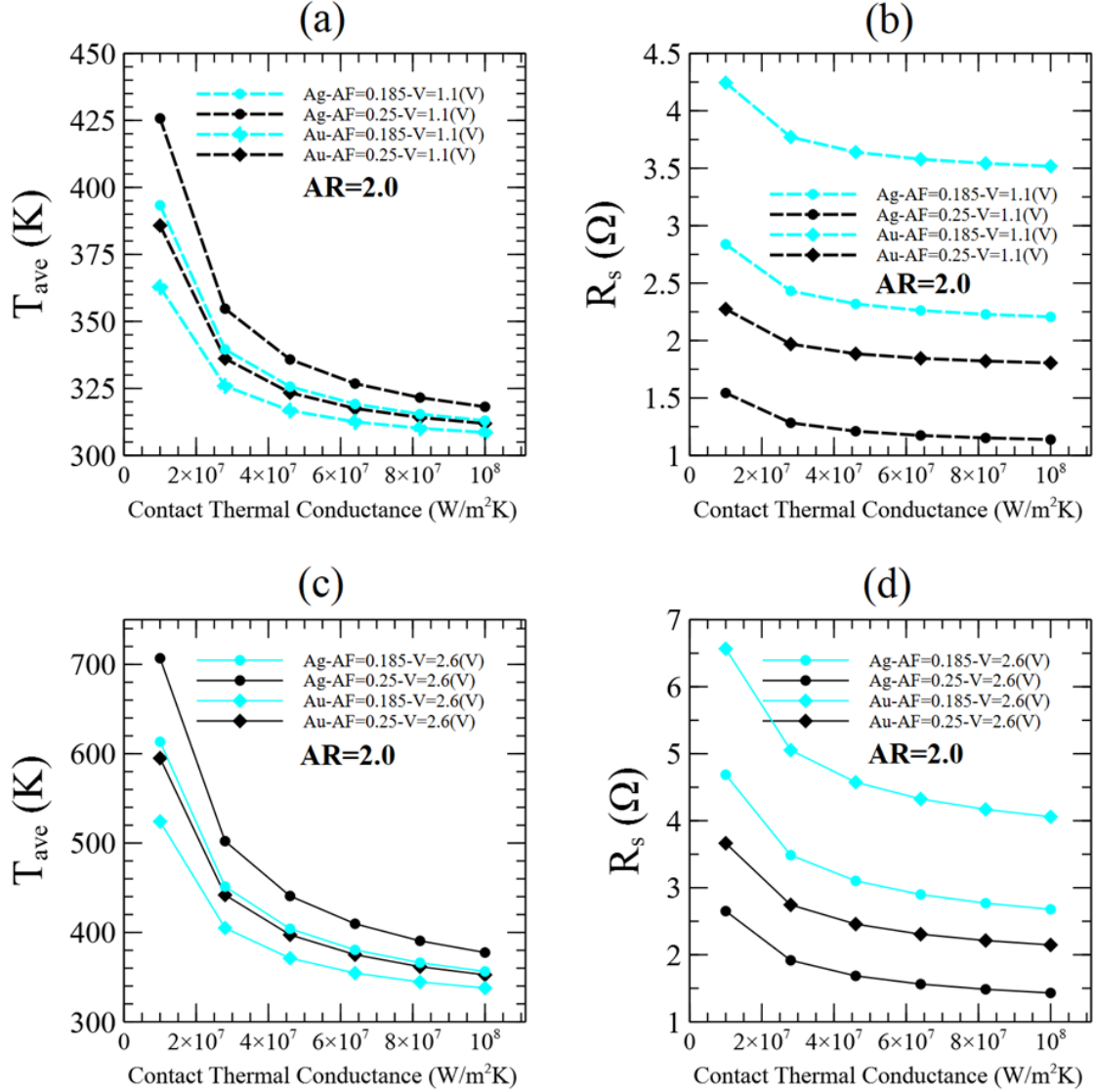
Figure 4.14: Estimated (a) T_{ave} and (b) R_s as a function of contact thermal conductance results for 1.1 V, fixed $AR_\blacksquare$, different area fraction values, and nanomaterials (Ag and Au). Estimated (c) T_{ave} and (d) R_s as a function of contact thermal conductance results for 2.6 V, fixed $AR_\blacksquare$, different area fraction values, and nanomaterials (Ag and Au). All seamless NWNs are $50 \times 50\,\mu m$ in size. Every data point refers to a single imported seamless NWN CAD file for COMSOL Multiphysics® simulation [110]. The regulating factors are comprised of the fixed $AR_\blacksquare = 2.0$, AF = 0.185 and 0.25, and bias voltage 1.1 V, shown by dash lines, and bias voltage 2.6 V, shown by solid lines. The materials chosen here are represented by two distinct symbols: Ag is denoted by circle symbols, while Au is denoted by square symbols (here $AR \equiv AR_\blacksquare = W_w/D_w$). Reproduced from Ref. [106] with permission from the Royal Society of Chemistry.

Seamless NWNs, with their planar percolated structure and undisrupted connection

119

arrangement, allow for a more precise spatial analysis in the form of colour maps that demonstrate the distribution of certain quantities throughout their nanowire segments. The temperature profile and local current density for a seamless NWN were determined using COMSOL Multiphysics® software [110] and are shown in Figure 4.15. The NWN is susceptible to electrical breakdown, which can occur if an active percolative nanowire reaches its threshold melting temperature. This leads to the disruption of current flow and results in a sudden change in the sheet resistance of the network. We performed electrothermal COMSOL Multiphysics® modelling [110], and the red areas in Figure 4.15 represent key nanochannels or junctions that have reached significant current densities or temperatures. Applying a different voltage will result in a different electric current density and temperature profile distribution throughout the network. If we apply a two-terminal electrode arrangement to a heterogeneous percolated metallic network, as shown in Figure 4.15 (a), we observe the characteristic electrostatic potential increase from drain to source. Current flows (conventionally) from source to drain terminals – depicted as vertical lines at the far left and right regions of the device – but the network creates a heterogeneous environment for current/temperature dispersion, which is apparent in Figure 4.15. The concentration of high current densities in the NWN occurs primarily at ridges that are oriented in a nearly horizontal direction or are aligned with the electric field direction established by the voltage difference at the terminals. This is due to the likelihood of these areas having a higher density of active percolative nanowires that can reach their critical melting temperature and cause electrical breakdown. Joule heating can cause melting and rupture in nanoscale ridges that are overwhelmed with current. Figure 4.15 (b) shows the network temperature distribution and demonstrates that "hotter" regions correspond to those with higher current densities (see Figure 4.15 (c)). Using the same model to analyse various seamless NWNs with diverse geometries yields temperature distributions that can be indicative of the presence of critical "hotspots" in the networks as displayed in Figure 4.15 (f).
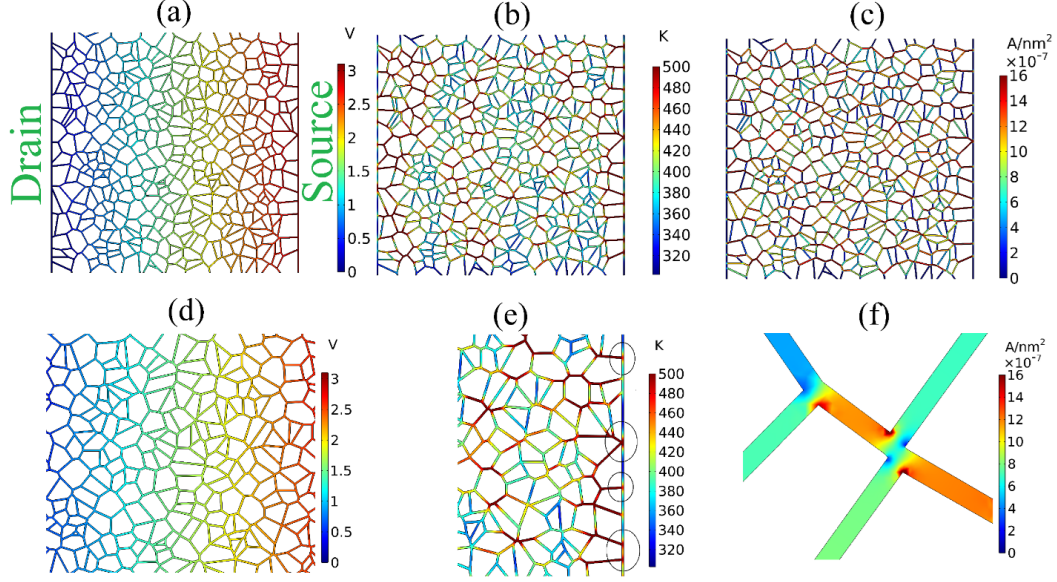
Figure 4.15: Colour maps produced from the electrothermal COMSOL Multiphysics® model [110] of an Ag seamless NWN. (a) Electrostatic potential generated along the source and drain electrodes. (b) Local network temperature profile and (c) current density across the same seamless NWN. (d) Magnified screenshot of the central region of the network in panel (a); this illustrates how the electrostatic potential varies at that region. (e) Magnified screenshot at the right electrode of the network in panel (b); this illustrates how the temperature fluctuates in the vicinity of the electrode. The circles emphasise crucial "hotspots" of high temperatures coloured in red. (f) Magnified screenshot at a seamless section from panel (c) showing high current densities coloured in red. The seamless NWNs is $50 \times 50 \, \mu m$ in size, $AR_\blacksquare = 1.0$, AF = 0.185, and voltage drop of 3.1 V. Reproduced from Ref. [106] with permission from the Royal Society of Chemistry.

Using high-spatial-resolution visualization analysis of temperature fluctuation throughout the network areas, we can understand better the device's conduction channels and the physical features that hinder performance, particularly in regard to electrothermal fracture [141]. Because of this, the temperature profiles determined by COMSOL Multiphysics® simulation [110] (see Figure 4.15 (b)) for a seamless NWN with settings of fixed AF = 0.185 and $AR_\blacksquare = 3$ were graphed as probability distributions that can be fitted by probability density functions (PDFs) of temperature differences (ΔT) as depicted in Figure 4.16. In this context, the temperature variation ΔT is defined as the outcome of deducting the predicted temperature from the ambient temperature, as determined by our simulations. Two bias voltages of 1.1 V and 4.6 V were applied to networks constructed of Ag, Al, Au, and Cu nanowire

121

ridges, and various temperature mappings were generated using COMSOL Multiphysics®
software [110] from which the temperature gradient distributions were ascertained. All distributions adhere to the two-parameter Weibull distribution, which is supported by our fitting study and is represented as

$$p(x, k, \varphi) = \frac{k}{\varphi} \left(\frac{x}{\varphi} \right)^{k-1} e^{-(x/\varphi)^k} \tag{4.3}$$

in which k is the shape parameter, φ is the scaling parameter, and x is the random variable. Regardless of the specifics of the networks' topology or the materials used, a Weibull PDF can properly reflect the distributions of temperature variations. Similarly as seen and reported in earlier studies [141, 146], the temperature distributions of standard disordered conducting networks commonly exhibit a Weibull pattern.
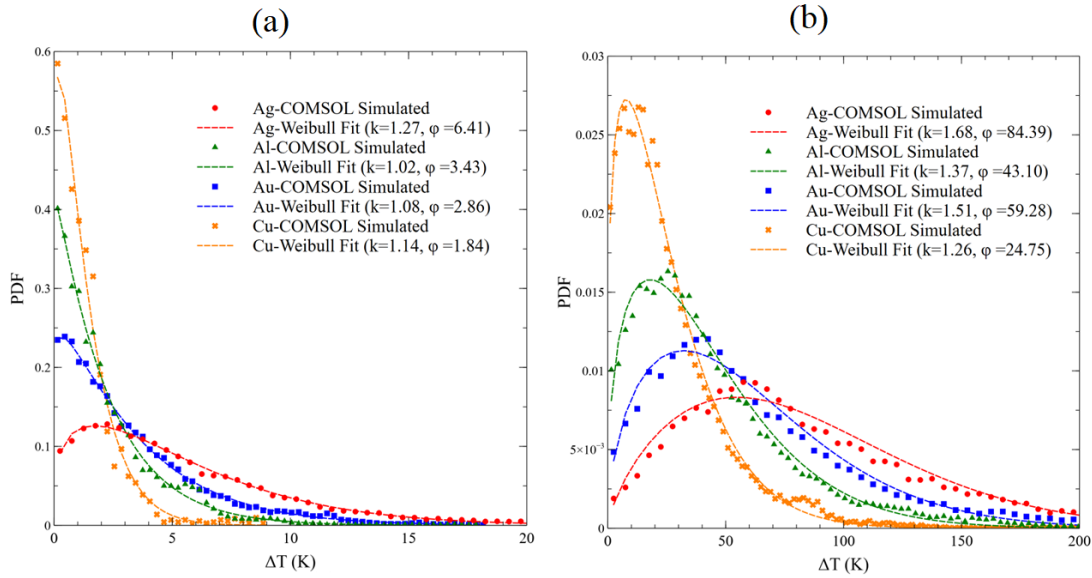
Figure 4.16: (Symbols) Temperature difference distributions obtained for seamless NWNs made of different nanomaterials, $AR_\blacksquare$ = 3, AF = 0.185 and two fixed biased voltages at (a) 1.1 V (b) 4.6 V. These were calculated utilizing COMSOL Multiphysics® software [110] for electrothermal simulations. The Weibull PDF was fitted for each case study as indicated by the dashed lines. The fitting parameters are provided in the legends. Panels reproduced from Ref. [106] with permission from the Royal Society of Chemistry.

To establish the Weibull distribution of temperature profiles, it is crucial to take into

account the impact of Joule heating on the percolative behaviour of the network. The Weibull PDF is verified to be well-fit to the estimated temperature distributions in Figure 4.16 for metallic seamless NWNs. Previously, it was shown that junction-based random NWNs exhibit the universal temperature characteristic given by the same two-parameter Weibull PDF [141, 146]. Our numerical results demonstrate that the heat transport parameters of seamless metallic NWNs also follow the Weibull distribution. Our findings supplement the existing literature on thermal Weibull profiles in spatially inhomogeneous percolating networks observed for junction-based and seamless NWN systems.

Let's now analyse and interpret the results shown in Figure 4.16; the majority of the PDFs are right-skewed, indicating that, for a given bias voltage, the temperature of the large percentage of the nanowires actively involving in the spreading of current rises relative to the initial temperature setting. In addition, this finding illustrates that the Weibull fitting parameters rely on the materials being used, which can be examined in terms of the total electrical current in the network, the latter of which will be addressed later. Weibull PDF's central features reveal intriguing differences across the materials; for example, Ag seamless NWNs show a higher temperature change dispersion with a mode at ~55 K, whereas Cu seamless NWNs show a smaller spread with a mode placed at ~7 K. Weibull PDFs are often used to describe random variables labelled as "time-to-failure", and by varying the value of the exponent k, we can learn more about the failure rate of the system under study. if $k > 1$, it implies that the failure rate of a system tends to rise over time, which can be attributed to the phenomenon of ageing where certain components of the system can deteriorate or wear out as time progresses. Our "ageing" process is temperature-driven, hence the random variable is ΔT (or "ΔT-to-failure"). In Figure 4.16, the k-values of all the NWNs reflect failure rates that rise with temperature difference. According to the average of a Weibull PDF, we can predict the average temperature difference to failure ($\langle \Delta T \rangle_f$) as

$$\langle \Delta T \rangle_f = \varphi \Gamma \left(1 + \frac{1}{k} \right).$$ (4.4)

Table 4.2 presents the mode and mean temperature-change to failure values for the seamless NWNs illustrated in Figure 4.16 (b). The data reveals that the Ag NWN has the highest mean temperature-change to failure, which is ~84 K, while the Cu NWN has the lowest mean temperature-change to failure, which is ~24 K.

Table 4.2: Mode and mean temperature-change to failure ($\langle \Delta T \rangle_f$) calculated from the Weibull PDF fitted on the data of Figure 4.16 (b).

Material	Mode (K)	$\langle \Delta T \rangle_f$ (K)
Ag	55.16	84.39
Au	32.02	59.28
Al	18.12	43.10
Cu	7.61	24.75

Based on the Weibull distribution analysis, we conclude that the Ag NWN is better equipped to withstand greater temperature fluctuations because of its efficient current/temperature spreading mechanism. Although the Cu NWN's self-heating mechanism and material attenuation can cover smaller temperature swings, its inability to expand out in the presence of more extreme heat makes them more vulnerable to electrothermal failure. Figure 4.17 presents a direct examination of the Weibull parameters derived from the fitting in Figure 4.16 at fixed 4.6 V and from another thermal analysis we performed for the identical systems but setting the voltage at 1.1 V. For this investigation, we plotted the total current passing through each seamless NWN constructed from distinct nanomaterials. The scatters in the plot for both voltage values are arranged in a crescent order, corresponding to distinct metals in a specific sequence: Cu→ Al → Au → Ag. The currents were calculated using Ohm's law $I_m = V/R_m$, in which V is the constant voltage shown in the legend, and R_m is the electrical resistance of each material (m = Cu, Al, Au, Ag) obtained from the COMSOL Multiphysics® model [110]. It is evident that both Weibull parameters (k and φ) exhibit distinct linear trends, particularly the scale parameter, indicating a scaling characteristic with the fixed voltage. In panel (a), there is a linear fit represented by the equation $y = cx + b$. The dependent variable y represents the φ/V^γ ratio, and the independent variable x represents the current I_m for each material m. To make the linear trends of the two voltage

sets align visually, the scaling exponent γ was adjusted and found to be $\gamma = 1.27$. For the high (V_h = 4.6 V) and low voltage (V_l = 1.1 V) regimes in panel (a), the slope and linear shift were fitted to be $c_h \approx c_l \approx 14$, with values for b_h = 0.477 and b_l = 0.129, respectively. In panel (b), there was no need to determine a voltage scaling exponent for the shape parameter k because the alignment of the slope was already visible. The slope and linear shift for this case were found to be $c_h \approx c_l \approx 0.61$, with values for b_h = 1.108 and b_l = 1.011, respectively. In conclusion, the analysis shown in Figure 4.17 generalises the Weibull thermal response of seamless NWNs constructed from different metals, in which the parameters can be derived via linear extrapolation of the models described here.
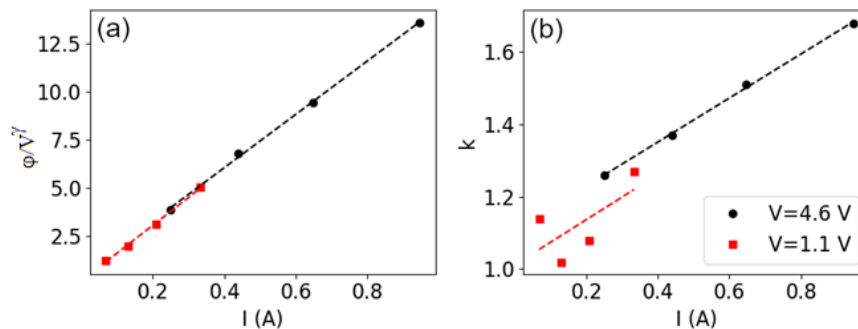
Figure 4.17: Analysis of the Weibull fitting parameters (φ, k) derived in Figure 4.16 as a function of voltage and materials' differences. The current shown in both panels serves as a proxy to indicate changes in the material. The scatters in the plot, for both high and low voltage values, correspond to a crescent order indicating a current increase with the material change: Cu→ Al → Au → Ag. In both panels, back circles show the data representing a high voltage regime (V_h = 4.6 V) whereas red squares show the data representing a low voltage regime (V_l = 1.1 V). The dashed lines are linear fits obtained from $y = cx + b$. The slope and the linear shift calculated in all linear fittings are: (a) $c_h \approx c_l \approx 14$, with values for b_h = 0.477 and b_l = 0.129. The scale parameter φ was scaled by V^γ to visually align the slope trends for different voltage values. The scaling exponent was found $\gamma = 1.27$. (b) $c_h \approx c_l \approx 0.61$, with values for b_h = 1.108 and b_l = 1.011. Reproduced from Ref. [106] with permission from the Royal Society of Chemistry.

4.4   Summary

This research employed computational techniques to analyse the thermo-electro-optical properties of seamless metallic NWNs with potential use as transparent conductors in flexible

display technologies. In this study, we demonstrated our computational framework for identifying material-dependent features and designing bespoke systems using nanowires made of Ag, Au, Al, and Cu. We established a computational method that incorporates electro-optical-thermal evaluation of seamless NWN thin films. Using this method, we were able to span a large parametric phase space, which involves intrinsic material properties, structural features of the device layouts, and coupling terms describing the exchange between the NWN and electrodes or substrate. Our primary results demonstrate, in a qualitative sense, that the FOM of seamless NWNs performs better than junction-based NWNs, making seamless NWNs a more suitable option for applications requiring transparent conductors. The sheet resistance ranges of the seamless NWNs studied here were heavily influenced by the material composition. Nevertheless, the seamless 2D structure of the NWNs, which was modelled as Voronoi diagrams, generally promoted transparency. Numerical predictions indicated that the NWNs had optical transmissions exceeding > 95%. We conducted a significant analysis to examine the local electrical and thermal impacts that could result in structural network failures, specifically wire segment breakdown, caused by Joule heating. Our results demonstrate that seamless NWNs display a temperature gradient distribution that can be described using a two-parameter Weibull probability density function, regardless of the materials' characteristics, bias voltage, and most crucially network node mapping. Our studies reveal that seamless NWNs fall into the same Weibull temperature distribution classification as junction-based NWNs, based on a comparison with earlier research that explored temperature profiles in junction-based NWNs. By comprehending the properties of Weibull distributions, we were able to derive crucial details about the seamless NWNs investigated in this study: Ag seamless NWNs have a broader temperature-spreading mechanism that permits better temperature tolerances than, for instance, Cu seamless NWNs. This research furthers our understanding of the basic principles behind the electrical conduction, optical transmission, and thermal aspects of seamless NWN devices. In conclusion, our robust computational framework appears as a crucial tool for informing the design and de-

126

velopment of versatile thermoelectric and electro-optical devices comprised of network-based nanostructures, as well as for providing accurate quantitative estimates of their thermo-electro-optical responses, which can support experimental efforts targeting their application in next-generation display technologies. It is also worth mentioning that we attempted to perform a direct comparison of our quantitative results here depicted. This is to make sure once more that our computational framework is tuned with past predictions conducted theoretically/computationally and experimentally. This comparison – catalogued in a table – can be found in Appendix A.

Chapter 5

Conclusions

This thesis explores the electro-optical-thermal characteristics of random NWNs by means of computational tools that can perform qualitative and quantitative analyses of physical quantities that describe the coupling and trade-off behaviours of those responses. This study uses computational and theoretical methods to anticipate the electro-optical-thermal responses of extremely disordered NWN structures and to elucidate the basic physical principles that drive these responses. The ability to forecast the behaviour of complex systems and gain insight into the processes responsible for that behaviour is a key reason why these computational tools and theoretical descriptions are so valuable. This thesis explores the characteristics of NWNs that are essential for their use as TCEs, including high transparency, variable sheet resistance, and thermal stability. Meanwhile, time restrictions prevented us from investigating another important facet of flexible display technologies: their mechanical endurance. The upcoming section will provide a scholarly discourse on the mechanical properties of these intricate networks as an outlook. The primary experimental findings related to this aspect will be highlighted, along with an overview of the relevant theoretical and computational investigations that can be integrated to establish a comprehensive understanding of the mechanical properties, in conjunction with the electro-optical-thermal properties expounded in this thesis. Below, I will briefly summarise the topics discussed in

each chapter of this thesis and our key conclusions.

A thorough introduction to metallic nanowires and their possible use in disordered NWNs as transparent conductors were provided in Chapter 1. The inherent characteristics of these materials, such as inner resistance, and the junction resistance that emerges when two nanowires cross and touch were discussed in detail in this chapter. The chapter also looked at introducing the electrical, optical, and thermal characteristics of disordered metallic NWNs, and in the context of how they functioned in an actual nanodevice. Several well-known examples of NWNs in which they are manufactured using different methods to modify the nanostructure physical characteristics of these materials for specific uses were also briefly covered in this chapter, including the junction-based (standard) disordered NWNs and the seamless NWNs. We introduced the research objectives that led to this work which is how complex NWN systems behave electrically, optically, and thermally and how can we couple these responses so one can understand how they affect each other.

The mathematical and theoretical foundations laid forth in Chapter 2 are the bedrock upon which the computational toolset presented in the rest of this thesis is built. This chapter provides an in-depth explanation of the theories and models that serve as the foundation for the computational framework. These theories and models include but are not limited to, percolation theory, graph/network characterization, MLST, Kirchhoff's circuit laws, the conduction properties of nanomaterials, Multiphysics computational package, and resistive network theory.

The computational framework and techniques for modelling the electro-optical characteristics of two distinct NWN layouts namely standard random NWNs and networks patterned with a transparent mesh to increase transparency are discussed in detail in Chapter 3 [97]. Nanowires of various metals including Ag, Al, Cu, and Au are used as transparent conducting electrodes in this research, and a number of adjustable parameters, including network area fraction, length-to-diameter aspect ratio, and angular orientations of nanowires, are explored. MLST with MatScat developed by Schäfer [108,109] and FEM in COMSOL Multiphysics®

software [110] were employed to provide predictions about the optical extinction efficiency coefficients of each material. The work gives useful insights into the trade-offs between improved optical transmittance and lower conductance via the analysis of different figures of merit (optical transmittance versus sheet resistance), which can influence the design of next-generation transparent conductor devices based on NWNs. We have identified and quantified the trade-off when employing grid-pattern networks instead of standard random networks by achieving more optical transmittance while hindering conductance. Moreover, the calculated EMI SE demonstrated that device layout such as grid-pattern design is a dominant factor and hence it can be re-casted to a certain level of attenuation to meet specific electro-optical criteria.

Chapter 4 builds upon the previous one by focusing on the investigation of the thermo-electro-optical properties of seamless NWNs, which are networks that do not have any junctions (by wire-wire contact), resulting in a continuous and uninterrupted network structure [106]. These NWNs possess unique properties, such as high conductivity and surface area-to-volume ratios, making them attractive for various applications in nanotechnology. To explore these properties, we employed in-house computational methods and electro-thermal models developed in COMSOL Multiphysics® software [110] to conduct a detailed computational analysis. Our in-house computational scripts estimated the sheet resistance of random seamless NWNs using Ohm's law and Kirchhoff's circuit laws and compared them with those obtained using COMSOL Multiphysics®. The study focused on four types of nanowires, including Al, Au, Cu, and Ag, to evaluate their transparent and electrical conduction properties, as well as their thermal response. We obtained corresponding figures of merit (optical transmittance versus sheet resistance) and temperature distributions to provide a complete characterization of the performance of transparent conductors idealized with seamless NWNs. Our calculations demonstrated in quantitative terms that material composition heavily impacts the sheet resistance ranges of the studied seamless NWNs, however, overall, their seamless 2D structure (modelled as Voronoi diagrams) favoured transparency

with numerical predictions indicating optical transmissions > 95%. Our findings reveal that seamless NWNs exhibit temperature difference distributions that can be modelled using a two-parameter Weibull probability density function, irrespective of the materials' properties, applied bias voltage, and most importantly network nodal mapping. By comparing with previous works that investigated temperature profiles in junction-based NWNs, our results confirm that seamless NWNs fall in the same Weibull temperature distribution category as junction-based NWNs. By understanding the characteristics of Weibull distributions, we were able to infer important specifics about the seamless films analyzed in this work. For instance, Ag seamless NWNs exhibit a wider temperature-spreading mechanism that allows for greater tolerances to temperature variations than for instance Cu seamless NWNs. This study contributes to the advancement of knowledge regarding the fundamental mechanisms underlying electrical conduction, optical transmission, and thermal properties of seamless NWN devices.

In summary, our robust computational framework detailed in this thesis appears as an important tool to inform the design and development of versatile thermoelectric and electro-optical devices made of NWN structures prone to transparent conductor applications and to provide reliable quantitative predictions of their thermo-electro-optical responses that can assist experimental efforts targeting their use in next-generation display technologies.

5.1   Outlook

Mechanical flexibility is another important feature that TCEs built out of the random NWNs required for applications in next-generation display technologies and solar cells [32, 39, 262]. Such applications require endurance to mechanical distortions. The sheet resistance of the distorted NWN can increase significantly in comparison to the resistance of the original network when subjected to external deformation such as bending [186, 263]. Thus, many percolation paths that exist within the network can be cut off upon bending, and the network

resistance rises as a consequence [190]. This resistance enhancement due to deformation is specific to 1D random networks and has not been observed significantly in other TCs including 2D (flake-like) and bulk materials [156]. To be more precise, a NWN encased in a thin film has exceptional mechanical resilience under a variety of bending test configurations. Therefore, many experimental efforts to overcome basic limits for mechanical durability have resulted in improved performance of random NWNs under harsh mechanical settings [28, 190, 264]. Metallic nanowires, particularly Ag nanowires, have a variety of mechanical qualities, the most notable of which are their surface roughness, flexibility, and bending capabilities. Low surface roughness is a critical criterion for optoelectronic device use as it has a significant impact on the device's functioning ability and efficacy [66, 265]. The roughness of the surface is highly dependent on the quality of the metal nanowires and the manufacturing method. By fabricating nanowires with long lengths and nanoscale diameters, the roughness and contact resistances between the nanowires may be efficiently reduced. Eliminating nanojunctions between nanowires by the previously described approaches can also massively reduce surface roughness and contact resistances [66, 265]. As a flexible device is desired, having a high deformation performance as a flexible transparent electrode is a necessity. The electrical conductivity of the metal nanowire-based device should endure minor variations after repeated bending under a particular bending angle, which is not only linked to flexibility stability but also directly to conductivity stability [28].

Due to the difficulty in regulating and manipulating NWNs during mechanical testing, determining and quantifying their mechanical properties can be a challenging task. The obtained mechanical properties from the current scientific literature report a wide variability in mechanical reactions depending on multiple lab setups and nanofabricated materials' characteristics. For example, the mechanical behaviour of individual nanowires can be influenced by imperfections, such as defects or impurities, resulting in variations in their properties. The accumulation of imperfections in NWNs can result in a subsequent deterioration of the mechanical properties of the entire network. Insufficient knowledge of the intrinsic and

size-dependent behaviour of nanowires upon mechanical deformation is a source of difficulty for such studies. To obtain a complete comprehension of the ultimate performance of complex networks, it is critical to simultaneously examine their electrical, optical, thermal, and mechanical characteristics. A list of the most important theoretical parameters that are typically controlled to determine the mechanical properties of NWNs is: (i) the elastic modulus that evaluates the stiffness of the NWN; (ii) yield strength that evaluates the amount of stress required to deform the NWN permanently; (iii) fracture strength that measures the maximum stress that the NWN can sustain before it breaks; (iv) plasticity that measures the amount of deformation that the NWN can undergo before it fails; (v) toughness that assesses the amount of energy needed to break the NWN, and (vi) yield strain that evaluates the amount of strain that the NWN can undergo before it starts to exhibiting permanent deformation [264].

In the context of investigating the mechanical properties of NWNs, experimental examinations as done in [266] can serve as the basis for developing computational models that allow for thorough testing of the structural and intrinsic properties of NWNs, and their resultant influence on the mechanical flexibility performance of nanodevices. Researchers can benefit from using a computational framework to replicate NWNs' behaviour and get a deeper understanding of the factors behind NWNs' optimised-superior performance. For example, Hwang et al. [190] have developed quantitative models to predict the electrical performance of random NWNs when exposed to external bending deformation. Their models rely on Monte Carlo-based simulations, which allow for an assessment of the behaviour of the networks. By utilizing solutions derived from their models, they were able to enhance the tolerance of the R_s of the networks subjected to deformation. They concluded that to enhance the tolerance of R_s against the bending of the network, increasing the AF and the length of individual nanowires can be an effective strategy. In addition, by aligning the nanowires parallel to the bend axis, it is possible to improve the network's efficacy even further in terms of R_s tolerance. Therefore, these works plus the computational framework

conducted in this thesis can serve as motivation for future work resulting in the incorporation of an in-depth mechanical analysis coupled with the electro-optical-thermal responses of disordered NWNs.

Bibliography

[1] Ladan Rashidi and Kianoush Khosravi-Darani. The applications of nanotechnology in food industry. *Critical Reviews in Food Science and Nutrition*, 51(8):723–730, 2011.

[2] Monica J. Hanus and Andrew T. Harris. Nanotechnology innovations for the construction industry. *Progress in Materials Science*, 58(7):1056–1102, 2013.

[3] Jurgen Schulte. *Nanotechnology: global strategies, industry trends and applications.* John Wiley & Sons, 2005.

[4] Anika Benozir Asha and Ravin Narain. Nanomaterials properties. In *Polymer Science and Nanotechnology*, pages 343–359. Elsevier, 2020.

[5] Richard C. Pleus and Vladimir Murashov. *Physico-chemical properties of nanomaterials.* CRC Press, 2018.

[6] Qi Zhang, Qi-Kai Li, and Mo Li. Internal stress and its effect on mechanical strength of metallic glass nanowires. *Acta Materialia*, 91:174–182, 2015.

[7] Tingting Zhou and Tong Zhang. Recent progress of nanostructured sensing materials from 0D to 3D: overview of structure-property-application relationship for gas sensors. *Small Methods*, 5(9):2100515, 2021.

[8] Thomas Ihn. *Semiconductor nanostructures: quantum states and electronic transport.* OUP Oxford, 2009.

[9] Daniel J. Blumenthal. Photonic integration for UV to IR applications. *APL Photonics*, 5(2):020903, 2020.

[10] Rashmi Choubey, Neha Sonker, Jaya Bajpai, Preeti Jain, and Anamika Singh. Synthesis of polymer nanomaterials, mechanisms, and their structural control. In *Advances in Polymeric Nanomaterials for Biomedical Applications*, pages 41–63. Elsevier, 2021.

[11] Zhengdi Wang, Tingting Hu, Ruizheng Liang, and Min Wei. Application of zero-dimensional nanomaterials in biosensing. *Frontiers in Chemistry*, 8:320, 2020.

[12] Y. Liu, A. Kannegulla, B. Wu, and L.-J. Cheng. Quantum dot Fullerene-based molecular beacon nanosensors for rapid, highly sensitive nucleic acid detection. *ACS Applied Materials & Interfaces*, 10:18524–18531, 2018.

[13] Zhao Sheng Qian, Xiao Yue Shan, Lu Jing Chai, Juan Juan Ma, Jian Rong Chen, and Hui Feng. DNA nanosensor based on biocompatible graphene quantum dots and carbon nanotubes. *Biosensors and Bioelectronics*, 60:64–70, 2014.

[14] Shi Ying Lim, Wei Shen, and Zhiqiang Gao. Carbon quantum dots and their applications. *Chemical Society Reviews*, 44(1):362–381, 2015.

[15] Yuanhong Xu, Xiaoxia Wang, Wen Ling Zhang, Fan Lv, and Shaojun Guo. Recent progress in two-dimensional inorganic quantum dots. *Chemical Society Reviews*, 47(2):586–625, 2018.

[16] R. H. Kodama. Magnetic nanoparticles. *Journal of Magnetism and Magnetic Materials*, 200(1-3):359–372, 1999.

[17] Ning Wang, Y. Cai, and R. Q. Zhang. Growth of nanowires. *Materials Science and Engineering: R: Reports*, 60(1-6):1–51, 2008.

[18] C. N. R. Rao, B. C. Satishkumar, A. Govindaraj, and Manashi Nath. Nanotubes. *ChemPhysChem*, 2(2):78–105, 2001.

[19] Krishnan Jayaraman, M. Kotaki, Yanzhong Zhang, Xiumei Mo, and S. Ramakrishna. Recent advances in polymer nanofibers. *Journal of Nanoscience and Nanotechnology*, 4(1-2):52–65, 2004.

[20] Jingwei Bai, Xing Zhong, Shan Jiang, Yu Huang, and Xiangfeng Duan. Graphene nanomesh. *Nature Nanotechnology*, 5(3):190–194, 2010.

[21] David M. B. Dombroski, Anqi Wang, John Z. Wen, and Marco Alfano. Joining and welding with a nanothermite and exothermic bonding using reactive multi-nanolayers– a review. *Journal of Manufacturing Processes*, 75:280–300, 2022.

[22] T. A. Dow and R. O. Scattergood. Mesoscale and microscale manufacturing processes: challenges for materials, fabrication and metrology. In *Proceedings of the ASPE Winter Topical Meeting*, volume 28, pages 14–19. Citeseer, 2003.

[23] Laetitia Bardet, Dorina T. Papanastasiou, Chiara Crivello, Masoud Akbari, João Resende, Abderrahime Sekkat, Camilo Sanchez-Velasquez, Laetitia Rapenne, Carmen Jiménez, David Muñoz-Rojas, et al. Silver nanowire networks: ways to enhance their physical properties and stability. *Nanomaterials*, 11(11):2785, 2021.

[24] Yugang Sun, Brian Mayers, Thurston Herricks, and Younan Xia. Polyol synthesis of uniform silver nanowires: a plausible growth mechanism and the supporting evidence. *Nano Letters*, 3(7):955–960, 2003.

[25] Neil P. Dasgupta, Jianwei Sun, Chong Liu, Sarah Brittman, Sean C. Andrews, Jongwoo Lim, Hanwei Gao, Ruoxue Yan, and Peidong Yang. 25th anniversary article: semiconductor nanowires–synthesis, characterization, and applications. *Advanced Materials*, 26(14):2137–2184, 2014.

[26] Li Na Quan, Joohoon Kang, Cun-Zheng Ning, and Peidong Yang. Nanowires for photonics. *Chemical Reviews*, 119(15):9153–9169, 2019.

[27] Ha Young Lee and Sejeong Kim. Nanowires for 2D material-based photonic and optoelectronic devices. *Nanophotonics*, 11:2571–2582, 2022.

[28] Dongchen Tan, Chengming Jiang, Qikun Li, Sheng Bi, and Jinhui Song. Silver nanowire networks with preparations and applications: a review. *Journal of Materials Science: Materials in Electronics*, 31(18):15669–15696, 2020.

[29] Daniel Langley, Gaël Giusti, Céline Mayousse, Caroline Celle, Daniel Bellet, and Jean-Pierre Simonato. Flexible transparent conductive materials based on silver nanowire networks: a review. *Nanotechnology*, 24(45):452001, 2013.

[30] Weiwei He and Changhui Ye. Flexible transparent conductive films on the basis of Ag nanowires: design and applications: a review. *Journal of Materials Science & Technology*, 31(6):581–588, 2015.

[31] Shengyun Huang, Yannan Liu, Fan Yang, Yong Wang, Ting Yu, and Dongling Ma. Metal nanowires for transparent conductive electrodes in flexible chromatic devices: a review. *Environmental Chemistry Letters*, 20:3005–3037, 2022.

[32] Fevzihan Basarir, Farid Sayar Irani, Arif Kosemen, B. Tugba Camic, Faruk Oytun, Bahadir Tunaboylu, Hee Jeong Shin, Ki Young Nam, and Hyosung Choi. Recent progresses on solution-processed silver nanowire based transparent conducting electrodes for organic solar cells. *Materials Today Chemistry*, 3:60–72, 2017.

[33] Kwok Wei Shah and Yong Lu. Morphology, large scale synthesis and building applications of copper nanomaterials. *Construction and Building Materials*, 180:544–578, 2018.

[34] Shihui Yu, Zengwen Liu, Le Zhao, and Lingxia Li. Degradable, ultra-flexible, transparent and conductive film made of assembling CuNWs on chitosan. *Optical Materials*, 123:111752, 2022.

[35] Rabeea D. Abdel-Rahim, Adham M. Nagiub, and Mahmoud A. Taher. Electrical and optical properties of flexible transparent silver nanowires electrodes. *International Journal of Thin Film Science and Technology*, 11(1):16, 2022.

[36] Jindong Liu, Shiyu Liu, and Yuying Wu. Flexible transparent conducting strontium vanadate/mica heteroepitaxial membranes with mechanically tunable transport behaviors. *Journal of Alloys and Compounds*, 895:162725, 2022.

[37] Houbao Liu, Zeya Huang, Tian Chen, Xinqing Su, Yunan Liu, and Renli Fu. Construction of 3D MXene/silver nanowires aerogels reinforced polymer composites for extraordinary electromagnetic interference shielding and thermal conductivity. *Chemical Engineering Journal*, 427:131540, 2022.

[38] Arij Naser Abougreen, Ahmed Esmail Shalan, Esraa Samy Abu Serea, and Mustafa K. A. Mohammed. Polymer nanocomposites for energy storage applications. In *Advances in Nanocomposite Materials for Environmental and Energy Harvesting Applications*, pages 697–724. Springer, 2022.

[39] Pedro Costa, Rita Polícia, Nikola Perinka, Yolanda Alesanco, Ana Viñuales, Estela O. Carvalho, Nelson Pereira, Margarida M. Fernandes, and Senentxu Lanceros-Mendez. Multifunctional touch sensing and antibacterial polymer-based core-shell metallic nanowire composites for high traffic surfaces. *Advanced Materials Technologies*, 7:2101575, 2022.

[40] Lei Oscar M. Cuasay, Francesca Louis M. Salazar, and Mary Donnabelle L. Balela. Flexible tactile sensors based on silver nanowires: material synthesis, microstructuring, assembly, performance, and applications. *Emergent Materials*, 5:51–76, 2022.

[41] Gundam Sandeep Kumar, Ranadeep Raj Sumukam, Rakesh Kumar Rajaboina, Ramu Naidu Savu, Mudavat Srinivas, and Murali Banavoth. Perovskite nanowires

for next-generation optoelectronic devices: lab to fab. *ACS Applied Energy Materials*, 5:1342–1377, 2022.

[42] Seyedeh Leila Mortazavifar, Mohammad Reza Salehi, Mojtaba Shahraki, and Ebrahim Abiri. Optimization of light absorption in ultrathin elliptical silicon nanowire arrays for solar cell applications. *Journal of Modern Optics*, 69(7):368–380, 2022.

[43] Xuesong Cai, Xiudi Xiao, Guizhang Sheng, Jieyuan Zheng, Yajie Zhao, and Gang Xu. Effect of pH on the structure and morphology of $W_{18}O_{49}$ nanowires and their electrochromic properties. *Ceramics International*, 48:20791–20800, 2022.

[44] Wanzhong Li, Ting Bai, Guoxing Fu, Qianqian Zhang, Jingbing Liu, Hao Wang, Yuying Sun, and Hui Yan. Progress and challenges in flexible electrochromic devices. *Solar Energy Materials and Solar Cells*, 240:111709, 2022.

[45] Andrew Balilonda, Ziqi Li, Yuequn Fu, Fatemeh Zabihi, Shengyuan Yang, Xinxin Huang, Xiaoming Tao, and Wei Chen. Perovskite fiber-shaped optoelectronic devices for wearable applications. *Journal of Materials Chemistry C*, 10:6957–6991, 2022.

[46] Rudai Zhao, Zhenkun Gu, Pengwei Li, Yiqiang Zhang, and Yanlin Song. Flexible and wearable optoelectronic devices based on perovskites. *Advanced Materials Technologies*, 7(3):2101124, 2022.

[47] Hao Yi, Ling Xia, and Shaoxian Song. Three-dimensional montmorillonite/Ag nanowire aerogel supported stearic acid as composite phase change materials for superior solar-thermal energy harvesting and storage. *Composites Science and Technology*, 217:109121, 2022.

[48] Ying-jie He, Yao-wen Shao, Yuan-yuan Xiao, Jing-hui Yang, Xiao-dong Qi, and Yong Wang. Multifunctional phase change composites based on elastic MXene/silver nanowire sponges for excellent thermal/solar/electric energy storage, shape memory,

and adjustable electromagnetic interference shielding functions. *ACS Applied Materials & Interfaces*, 14:6057–6070, 2022.

[49] Jeffery L. Coffer. An overview of semiconducting silicon nanowires for biomedical applications. *Semiconducting Silicon Nanowires for Biomedical Applications*, pages 1–6, 2022.

[50] Gengfeng Zheng. Growth and characterization of silicon nanowires for biomedical applications. In *Semiconducting Silicon Nanowires for Biomedical Applications*, pages 7–24. Elsevier, 2022.

[51] Vardan Galstyan, Abderrahim Moumen, Gayan W. C. Kumarage, and Elisabetta Comini. Progress towards chemical gas sensors: Nanowires and 2D semiconductors. *Sensors and Actuators B: Chemical*, page 131466, 2022.

[52] Matawee Punginsang, Dario Zappa, Elisabetta Comini, Anurat Wisitsoraat, Giorgio Sberveglieri, Andrea Ponzoni, and Chaikarn Liewhiran. Selective H_2S gas sensors based on ohmic hetero-interface of Au-functionalized WO_3 nanowires. *Applied Surface Science*, 571:151262, 2022.

[53] Gianluca Milano, Giacomo Pedretti, Kevin Montano, Saverio Ricci, Shahin Hashemkhani, Luca Boarino, Daniele Ielmini, and Carlo Ricciardi. In materia reservoir computing with a fully memristive architecture based on self-organizing nanowire networks. *Nature Materials*, 21(2):195–202, 2022.

[54] Suhas Kumar, Xinxin Wang, John Paul Strachan, Yuchao Yang, and Wei D. Lu. Dynamical memristors for higher-complexity neuromorphic computing. *Nature Reviews Materials*, 7:575–591, 2022.

[55] Ritu Gupta, K. D. M. Rao, S. Kiruthika, and Giridhar U. Kulkarni. Visibly transparent heaters. *ACS Applied Materials & Interfaces*, 8(20):12559–12575, 2016.

[56] Dorina T. Papanastasiou, Amélie Schultheiss, David Muñoz-Rojas, Caroline Celle, Alexandre Carella, Jean-Pierre Simonato, and Daniel Bellet. Transparent heaters: a review. *Advanced Functional Materials*, 30(21):1910225, 2020.

[57] Danning Fu, Rendang Yang, Yang Wang, Ruibin Wang, and Feiguo Hua. Silver nanowire synthesis and applications in composites: progress and prospects. *Advanced Materials Technologies*, 7:2200027, 2022.

[58] Neha Sharma, Nitheesh M. Nair, Garikapati Nagasarvari, Debdutta Ray, and Parasuraman Swaminathan. A review of silver nanowire-based composites for flexible electronic applications. *Flexible and Printed Electronics*, 7:014009, 2022.

[59] Xueteng Zhu, Jinyan Xiong, Zhiyuan Wang, Rong Chen, Gang Cheng, and Yuen Wu. Metallic copper-containing composite photocatalysts: fundamental, materials design, and photoredox applications. *Small Methods*, 6(2):2101001, 2022.

[60] Vu Binh Nam and Daeho Lee. Copper nanowires and their applications for flexible, transparent conducting films: a review. *Nanomaterials*, 6(3):47, 2016.

[61] Yuanchao Zhang, Wendy Chu, Alireza Dibaji Foroushani, Hongbin Wang, Da Li, Jingquan Liu, Colin J. Barrow, Xin Wang, and Wenrong Yang. New gold nanostructures for sensor applications: a review. *Materials*, 7(7):5169–5201, 2014.

[62] Maria E. Messing, Karla Hillerich, Jonas Johansson, Knut Deppert, and Kimberly A. Dick. The use of gold for fabrication of nanowire structures. *Gold Bulletin*, 42(3):172–181, 2009.

[63] I. K. Yanson, O. I. Shklyarevskii, J. M. Van Ruitenbeek, and Sylvia Speller. Aluminum nanowires: Influence of work hardening on conductance histograms. *Physical Review B*, 77(3):033411, 2008.

[64] M. Zgirski, K. P. Riikonen, V. Touboltsev, and K. Yu Arutyunov. Quantum fluctuations in ultranarrow superconducting aluminum nanowires. *Physical Review B*, 77(5):054508, 2008.

[65] Jinwei Gao, Krzysztof Kempa, Michael Giersig, Eser Metin Akinoglu, Bing Han, and Ruopeng Li. Physics of transparent conductors. *Advances in Physics*, 65(6):553–617, 2016.

[66] Chuan Fei Guo and Zhifeng Ren. Flexible transparent conductors based on metal nanowire networks. *Materials Today*, 18(3):143–154, 2015.

[67] Go Kawamura, Hiroyuki Muto, and Atsunori Matsuda. Hard template synthesis of metal nanowires. *Frontiers in Chemistry*, 2:104, 2014.

[68] Timothy R. Kline, Mingliang Tian, Jinguo Wang, Ayusman Sen, Moses W. H. Chan, and Thomas E. Mallouk. Template-grown metal nanowires. *Inorganic Chemistry*, 45(19):7555–7565, 2006.

[69] Haibo Zeng, Jingbiao Cui, Bingqiang Cao, Ursula Gibson, Yoshio Bando, and Dmitri Golberg. Electrochemical deposition of ZnO nanowire arrays: organization, doping, and properties. *Science of Advanced Materials*, 2(3):336–358, 2010.

[70] D. V. Ravi Kumar, Kyoohee Woo, and Jooho Moon. Promising wet chemical strategies to synthesize Cu nanowires for emerging electronic applications. *Nanoscale*, 7(41):17195–17210, 2015.

[71] Agil Aditya Dinata, Abel Maaruf Rosyadi, Syukri Hamid, and Rahadian Zainul. A review chemical vapor deposition: process and application. *INA-Rxiv*, 2018.

[72] Peiyuan Guan, Renbo Zhu, Yanzhe Zhu, Fandi Chen, Tao Wan, Zhemi Xu, Rakesh Joshi, Zhaojun Han, Long Hu, Tom Wu, et al. Performance degradation and mitigation

strategies of silver nanowire networks: a review. *Critical Reviews in Solid State and Materials Sciences*, 47:435–459, 2021.

[73] Shengrong Ye, Aaron R. Rathmell, Zuofeng Chen, Ian E. Stewart, and Benjamin J. Wiley. Metal nanowire networks: the next generation of transparent conductors. *Advanced Materials*, 26(39):6670–6687, 2014.

[74] LePing Yu, Cameron Shearer, and Joseph Shapter. Recent development of carbon nanotube transparent conductive films. *Chemical Reviews*, 116(22):13413–13453, 2016.

[75] Jonathan K. Wassei and Richard B. Kaner. Graphene, a promising transparent conductor. *Materials Today*, 13(3):52–59, 2010.

[76] Jianyong Ouyang. Application of intrinsically conducting polymers in flexible electronics. *SmartMat*, 2(3):263–285, 2021.

[77] Takehiro Tokuno, Masaya Nogi, Makoto Karakawa, Jinting Jiu, Thi Thi Nge, Yoshio Aso, and Katsuaki Suganuma. Fabrication of silver nanowire transparent electrodes at room temperature. *Nano Research*, 4(12):1215–1222, 2011.

[78] Erik C. Garnett, Wenshan Cai, Judy J. Cha, Fakhruddin Mahmood, Stephen T. Connor, M. Greyson Christoforo, Yi Cui, Michael D. McGehee, and Mark L. Brongersma. Self-limited plasmonic welding of silver nanowire junctions. *Nature Materials*, 11(3):241–249, 2012.

[79] Donggyun Kim, Sung-Hoon Kim, Jong Hak Kim, Jae-Chul Lee, Jae-Pyoung Ahn, and Sang Woo Kim. Failure criterion of silver nanowire electrodes on a polymer substrate for highly flexible devices. *Scientific Reports*, 7:45903, 2017.

[80] Tahmina Akter and Woo Soo Kim. Reversibly stretchable transparent conductive coatings of spray-deposited silver nanowires. *ACS Applied Materials & Interfaces*, 4(4):1855–1859, 2012.

144

[81] Emmet Sheerin. *A Study on the Fabrication of Seamless Semiconducting and Metallic Nanowire Networks and their Applications for Transparent Electronics.* PhD thesis, Trinity College Dublin, 2020.

[82] Colin J. O'Callaghan. *Transport Properties of Disordered Nanowire Networks: From Conducting Thin Films to Neuromorphic Applications.* PhD thesis, Trinity College Dublin, 2018.

[83] Allen T. Bellew, Hugh G. Manning, Claudia Gomes da Rocha, Mauro S. Ferreira, and John J. Boland. Resistance of single Ag nanowire junctions and their role in the conductivity of nanowire networks. *ACS Nano*, 9(11):11422–11429, 2015.

[84] Hugh G. Manning, Patrick F. Flowers, Mutya A. Cruz, Claudia Gomes da Rocha, Colin O' Callaghan, Mauro S. Ferreira, Benjamin J. Wiley, and John J. Boland. The resistance of Cu nanowire–nanowire junctions and electro-optical modeling of Cu nanowire networks. *Applied Physics Letters*, 116(25):251902, 2020.

[85] Hui Wu, Desheng Kong, Zhichao Ruan, Po-Chun Hsu, Shuang Wang, Zongfu Yu, Thomas J. Carney, Liangbing Hu, Shanhui Fan, and Yi Cui. A transparent electrode based on a metal nanotrough network. *Nature Nanotechnology*, 8(6):421–425, 2013.

[86] Yang Yang, Sai Chen, Wanli Li, Peng Li, Jiangang Ma, Bingsheng Li, Xiaoning Zhao, Zhongshi Ju, Huicong Chang, Lin Xiao, et al. Reduced graphene oxide conformally wrapped silver nanowire networks for flexible transparent heating and electromagnetic interference shielding. *ACS Nano*, 14(7):8754–8765, 2020.

[87] Xuecheng Yu, Xianwen Liang, Rajavel Krishnamoorthy, Wen Jiang, Leicong Zhang, Longquan Ma, Pengli Zhu, Yougen Hu, Rong Sun, and Ching-Ping Wong. Transparent and flexible hybrid nanogenerator with welded silver nanowire networks as the electrodes for mechanical energy harvesting and physiological signal monitoring. *Smart Materials and Structures*, 29(4):045040, 2020.

[88] Joana P. Neto, Adriana Costa, Joana Vaz Pinto, André Marques-Smith, Júlio Costa, Rodrigo Martins, Elvira Fortunato, Adam R. Kampff, and Pedro Barquinha. Transparent and flexible ECoG electrode arrays based on silver nanowire networks for neural recordings. *bioRxiv*, 2021.

[89] Sangyeob Lee, Jiseong Jang, Taejun Park, Young Min Park, Joon Sik Park, Yoon-Kee Kim, Hyoung-Keun Lee, Eun-Chae Jeon, Doh-Kwon Lee, Byungmin Ahn, et al. Electrodeposited silver nanowire transparent conducting electrodes for thin-film solar cells. *ACS Applied Materials & Interfaces*, 12(5):6169–6175, 2020.

[90] Viet Huong Nguyen, Dorina T. Papanastasiou, Joao Resende, Laetitia Bardet, Thomas Sannicolo, Carmen Jiménez, David Muñoz-Rojas, Ngoc Duy Nguyen, and Daniel Bellet. Advances in flexible metallic transparent electrodes. *Small*, 18(19):2106006, 2022.

[91] Phillip Lee, Jinhwan Lee, Hyungman Lee, Junyeob Yeo, Sukjoon Hong, Koo Hyun Nam, Dongjin Lee, Seung Seob Lee, and Seung Hwan Ko. Highly stretchable and highly conductive metal electrode by very long metal nanowire percolation network. *Advanced Materials*, 24(25):3326–3332, 2012.

[92] David S. Hecht, Liangbing Hu, and Glen Irvin. Emerging transparent electrodes based on thin films of carbon nanotubes, graphene, and metallic nanostructures. *Advanced Materials*, 23(13):1482–1513, 2011.

[93] Huiying Li, Yunfei Liu, Anyang Su, Jintao Wang, and Yu Duan. Promising hybrid graphene-silver nanowire composite electrode for flexible organic light-emitting diodes. *Scientific Reports*, 9:17998, 2019.

[94] Pengfei Kou, Liu Yang, Cheng Chang, and Sailing He. Improved flexible transparent conductive electrodes based on silver nanowire networks by a simple sunlight illumination approach. *Scientific Reports*, 7:42052, 2017.

146

[95] Toshiaki Kondo, Naoya Kitagishi, Tatsuro Fukushima, Takashi Yanagishita, and Hideki Masuda. Fabrication of aluminum nanowires by mechanical deformation of Al using anodic porous alumina molds. *Materials Express*, 6(4):363–366, 2016.

[96] Rose M. Mutiso, Michelle C. Sherrott, Aaron R. Rathmell, Benjamin J. Wiley, and Karen I. Winey. Integrating simulations and experiments to predict sheet resistance and optical transmittance in nanowire films for transparent conductors. *ACS Nano*, 7(9):7654–7663, 2013.

[97] Koorosh Esteki, Hugh G. Manning, Emmet Sheerin, Mauro S. Ferreira, John J. Boland, and Claudia Gomes da Rocha. Tuning the electro-optical properties of nanowire networks. *Nanoscale*, 13(36):15369–15379, 2021.

[98] Hugh G. Manning, Claudia Gomes da Rocha, Colin O' Callaghan, Mauro S. Ferreira, and John J. Boland. The electro-optical performance of silver nanowire networks. *Scientific Reports*, 9:11550, 2019.

[99] Jeremy Hicks, Junying Li, Chen Ying, and Ant Ural. Effect of nanowire curviness on the percolation resistivity of transparent, conductive metal nanowire networks. *Journal of Applied Physics*, 123(20):204309, 2018.

[100] Jessamyn A. Fairfield, Carlos Ritter, Allen T. Bellew, Eoin K. McCarthy, Mauro S. Ferreira, and John J. Boland. Effective electrode length enhances electrical activation of nanowire networks: experiment and simulation. *ACS Nano*, 8(9):9542–9549, 2014.

[101] Colin O'Callaghan, Claudia Gomes da Rocha, Hugh G. Manning, John J. Boland, and Mauro S. Ferreira. Effective medium theory for the conductivity of disordered metallic nanowire networks. *Physical Chemistry Chemical Physics*, 18(39):27564–27571, 2016.

[102] Hugh G. Manning. *An Investigation of the Electrical Behaviours of Metallic, Semiconducting and Core-shell Nanowires.* PhD thesis, Trinity College Dublin, 2018.

[103] Tao Wan, Peiyuan Guan, Xinwei Guan, Long Hu, Tom Wu, Claudio Cazorla, and Dewei Chu. Facile patterning of silver nanowires with controlled polarities via inkjet-assisted manipulation of interface adhesion. *ACS Applied Materials & Interfaces*, 12(30):34086–34094, 2020.

[104] Jiahui Gu, Shaowei Hu, Hongjun Ji, Huanhuan Feng, Weiwei Zhao, Jun Wei, and Mingyu Li. Multi-layer silver nanowire/polyethylene terephthalate mesh structure for highly efficient transparent electromagnetic interference shielding. *Nanotechnology*, 31(18):185303, 2020.

[105] Zhenxing Yin, Seung Keun Song, Duck-Jae You, Yeongun Ko, Sanghun Cho, Jeeyoung Yoo, Si Yun Park, Yuanzhe Piao, Suk Tai Chang, and Youn Sang Kim. Novel synthesis, coating, and networking of curved copper nanowires for flexible transparent conductive electrodes. *Small*, 11(35):4576–4583, 2015.

[106] K. Esteki, D. Curic, H. G. Manning, E. Sheerin, M. S. Ferreira, J. J. Boland, and C. G. Rocha. Thermo-electro-optical properties of seamless metallic nanowire networks for transparent conductor applications. *Nanoscale*, 15(24):10394–10411, 2023.

[107] Craig F. Bohren and Donald R. Huffman. *Absorption and scattering of light by small particles*. John Wiley & Sons, 2008.

[108] J. Schäfer. MatScat, MATLAB Central File Exchange. `https://www.mathworks.com/matlabcentral/fileexchange/36831-matscat`, 2023.

[109] Jan-Patrick Schäfer. *Implementierung und Anwendung analytischer und numerischer Verfahren zur Lösung der Maxwellgleichungen für die Untersuchung der Lichtausbreitung in biologischem Gewebe*. PhD thesis, Universität Ulm, 2011.

[110] COMSOL ® V. 5.6. COMSOL AB, Stockholm, Sweden.

[111] Sukang Bae, Sang Jin Kim, Dolly Shin, Jong-Hyun Ahn, and Byung Hee Hong. Towards industrial applications of graphene electrodes. *Physica Scripta*, 2012(T146):014024, 2012.

[112] I. Dierking. Carbon allotropes as ITO electrode replacement materials in liquid crystal devices. *C*, 6(4):80, 2020.

[113] L. X. He and S. C. Tjong. Nanostructured transparent conductive films: fabrication, characterization and applications. *Materials Science and Engineering: R: Reports*, 109:1–101, 2016.

[114] Mukti Aryal, Joseph Geddes, Oliver Seitz, Jonathan Wassei, Ian McMackin, and Boris Kobrin. Sub-micron transparent metal mesh conductor for touch screen displays. *SID Symposium Digest of Technical Papers*, 45:194–196, 2014.

[115] D. Bellet, M. Lagrange, T. Sannicolo, S. Aghazadehchors, V. H. Nguyen, D. P. Langley, D. Muñoz Rojas, C. Jiménez, Y. Bréchet, and N. D. Nguyen. Transparent electrodes based on silver nanowire networks: from physical considerations towards device integration. *Materials*, 10:570, 2017.

[116] T. Kim, Y. W. Kim, H. S. Lee, H. Kim, W. S. Yang, and K. S. Suh. Uniformly interconnected silver-nanowire networks for transparent film heaters. *Adv. Funct. Mater.*, 23:1250–1255, 2013.

[117] Shengrong Ye, Aaron R. Rathmell, Ian E. Stewart, Yoon-Cheol Ha, Adria R. Wilson, Zuofeng Chen, and Benjamin J. Wiley. A rapid synthesis of high aspect ratio copper nanowires for high-performance transparent conducting films. *Chem. Commun.*, 50:2562–2564, 2014.

[118] Cecilia Mattevi, Hokwon Kim, and Manish Chhowalla. A review of chemical vapour deposition of graphene on copper. *J. Mater. Chem.*, 21:3324–3334, 2011.

149

[119] A. Elschner and W. Lövenich. Solution-deposited PEDOT for transparent conductive applications. *MRS Bulletin*, 36:794–798, 2011.

[120] Weiran Cao, Jian Li, Hongzheng Chen, and Jiangeng Xue. Transparent electrodes for organic optoelectronic devices: a review. *Journal of Photonics for Energy*, 4(1):040990–040990, 2014.

[121] Ankush Kumar and G. U. Kulkarni. Evaluating conducting network based transparent electrodes from geometrical considerations. *Journal of Applied Physics*, 119(1):015102, 2016.

[122] Ankush Kumar, N. S. Vidhyadhiraja, and Giridhar U. Kulkarni. Current distribution in conducting nanowire networks. *Journal of Applied Physics*, 122(4):045101, 2017.

[123] Robert Benda, Eric Cancès, and Bérengère Lebental. Effective resistance of random percolating networks of stick nanowires: functional dependence on elementary physical parameters. *Journal of Applied Physics*, 126(4):044306, 2019.

[124] Milan Žeželj and Igor Stanković. From percolating to dense random stick networks: conductivity model investigation. *Physical Review B*, 86(13):134202, 2012.

[125] Sukanta De, Thomas M. Higgins, Philip E. Lyons, Evelyn M. Doherty, Peter N. Nirmalraj, Werner J. Blau, John J. Boland, and Jonathan N. Coleman. Silver nanowire networks as flexible, transparent, conducting films: extremely high DC to optical conductivity ratios. *ACS Nano*, 3(7):1767–1774, 2009.

[126] Lea Hu, D. S. Hecht, and G. Grüner. Percolation in transparent and conducting carbon nanotube networks. *Nano Letters*, 4(12):2513–2517, 2004.

[127] Seunghoe Koo, Jaehee Park, Sangmo Koo, and Kyeongtae Kim. Local heat dissipation of Ag nanowire networks examined with scanning thermal microscopy. *The Journal of Physical Chemistry C*, 125(11):6306–6312, 2021.

[128] Zijing Zeng, Changhong Wang, and Jinwei Gao. Numerical simulation and optimization of metallic network for highly efficient transparent conductive films. *Journal of Applied Physics*, 127(6):065104, 2020.

[129] Ritu Gupta, Ankush Kumar, Sridhar Sadasivam, Sunil Walia, Giridhar U. Kulkarni, Timothy S. Fisher, and Amy Marconnet. Microscopic evaluation of electrical and thermal conduction in random metal wire networks. *ACS Applied Materials & Interfaces*, 9(15):13703–13712, 2017.

[130] R. Franz and G. Wiedemann. Ueber die Wärme-Leitungsfähigkeit der Metalle. *Annalen Der Physik*, 165(8):497–531, 1853.

[131] Jianli Wang, Zhizheng Wu, Chengkun Mao, Yunfeng Zhao, Juekuan Yang, and Yunfei Chen. Effect of electrical contact resistance on measurement of thermal conductivity and Wiedemann-Franz law for individual metallic nanowires. *Scientific Reports*, 8:4862, 2018.

[132] F. Völklein, H. Reith, T. W. Cornelius, M. Rauber, and R. Neumann. The experimental investigation of thermal conductivity and the Wiedemann–Franz law for single metallic nanowires. *Nanotechnology*, 20(32):325706, 2009.

[133] Yue Shi, Liang He, Qian Deng, Quanxiao Liu, Luhai Li, Wei Wang, Zhiqing Xin, and Ruping Liu. Synthesis and applications of silver nanowires for transparent conductive films. *Micromachines*, 10(5):330, 2019.

[134] Lin Qiu, Ning Zhu, Yanhui Feng, Efstathios E. Michaelides, Gaweł Żyła, Dengwei Jing, Xinxin Zhang, Pamela M. Norris, Christos N. Markides, and Omid Mahian. A review of recent advances in thermophysical properties at the nanoscale: from solid state to colloids. *Physics Reports*, 843:1–81, 2020.

[135] Dong Chul Choo and Tae Whan Kim. Degradation mechanisms of silver nanowire electrodes under ultraviolet irradiation and heat treatment. *Scientific Reports*, 7:1696, 2017.

[136] Harim Oh, Jeeyoung Lee, and Myeongkyu Lee. Transformation of silver nanowires into nanoparticles by rayleigh instability: comparison between laser irradiation and heat treatment. *Applied Surface Science*, 427:65–73, 2018.

[137] Kerry Maize, Suprem R. Das, Sajia Sadeque, Amr M. S. Mohammed, Ali Shakouri, David B. Janes, and Muhammad A. Alam. Super-joule heating in graphene and silver nanowire network. *Applied Physics Letters*, 106(14):143104, 2015.

[138] Sajia Sadeque, Aaditya Candadai, Yu Gong, Kerry Maize, Amir K. Ziabari, Amr M. S. Mohammed, Ali Shakouri, Timothy Fisher, and David B. Janes. Transient self-heating at nanowire junctions in silver nanowire network conductors. *IEEE Transactions on Nanotechnology*, 17(6):1171–1180, 2018.

[139] Hadi Hosseinzadeh Khaligh, L. Xu, Alireza Khosropour, Alexandra Madeira, M. Romano, Christophe Pradére, Mona Tréguer-Delapierre, Laurent Servant, Michael A. Pope, and Irene A. Goldthorpe. The joule heating problem in silver nanowire transparent electrodes. *Nanotechnology*, 28(42):425703, 2017.

[140] Thomas Sannicolo, Nicolas Charvin, Lionel Flandin, Silas Kraus, Dorina T. Papanastasiou, Caroline Celle, Jean-Pierre Simonato, David Munoz-Rojas, Carmen Jiménez, and Daniel Bellet. Electrical mapping of silver nanowire networks: a versatile tool for imaging network homogeneity and degradation dynamics during failure. *ACS Nano*, 12(5):4648–4659, 2018.

[141] Suprem R. Das, Amr M. S. Mohammed, Kerry Maize, Sajia Sadeque, Ali Shakouri, David B. Janes, and Muhammad A. Alam. Evidence of universal temperature scaling in self-heated percolating networks. *Nano Letters*, 16(5):3130–3136, 2016.

152

[142] Colin O'Callaghan, Claudia G. Rocha, Fabio Niosi, Hugh G. Manning, John J. Boland, and Mauro S. Ferreira. Collective capacitive and memristive responses in random nanowire networks: emergence of critical connectivity pathways. *Journal of Applied Physics*, 124(15):152118, 2018.

[143] J. A. Fairfield, C. G. Rocha, C. O'Callaghan, M. S. Ferreira, and J. J. Boland. Co-percolation to tune conductive behaviour in dynamical metallic nanowire networks. *Nanoscale*, 8(43):18516–18523, 2016.

[144] Claudia Gomes da Rocha, Hugh G. Manning, Colin O'Callaghan, Carlos Ritter, Allen T. Bellew, John J. Boland, and Mauro S. Ferreira. Ultimate conductivity performance in metallic nanowire networks. *Nanoscale*, 7(30):13011–13016, 2015.

[145] Sahar Alialy, Koorosh Esteki, Mauro S. Ferreira, John J. Boland, and Claudia Gomes da Rocha. Nonlinear ion drift-diffusion memristance description of TiO_2 RRAM devices. *Nanoscale Advances*, 2(6):2514–2524, 2020.

[146] Man Prakash Gupta, Nitish Kumar, and Satish Kumar. Computational study of thermal transport in nanowire-graphene thin films. *IEEE Transactions on Nanotechnology*, 17(4):829–836, 2018.

[147] Parveen Saini, Veena Choudhary, B. P. Singh, R. B. Mathur, and S. K. Dhawan. Enhanced microwave absorption behavior of polyaniline-CNT/polystyrene blend in 12.4–18.0 GHz range. *Synthetic Metals*, 161(15-16):1522–1526, 2011.

[148] Parveen Saini, Veena Choudhary, B. P. Singh, R. B. Mathur, and S. K. Dhawan. Polyaniline–MWCNT nanocomposites for microwave absorption and EMI shielding. *Materials Chemistry and Physics*, 113(2-3):919–926, 2009.

[149] Li-Chuan Jia, Ding-Xiang Yan, Xiaofeng Liu, Rujun Ma, Hong-Yuan Wu, and Zhong-Ming Li. Highly efficient and reliable transparent electromagnetic interference shielding film. *ACS Applied Materials & Interfaces*, 10(14):11941–11949, 2018.

[150] Xingzhong Zhu, Juan Xu, Feng Qin, Zhiyang Yan, Aoqi Guo, and Caixia Kan. Highly efficient and stable transparent electromagnetic interference shielding films based on silver nanowires. *Nanoscale*, 12(27):14589–14597, 2020.

[151] G. E. Pike and C. H. Seager. Percolation and conductivity: a computer study. i. *Physical Review B*, 10(4):1421, 1974.

[152] Daniel P. Langley, Mélanie Lagrange, Ngoc Duy Nguyen, and Daniel Bellet. Percolation in networks of 1-dimensional objects: comparison between Monte Carlo simulations and experimental observations. *Nanoscale Horizons*, 3(5):545–550, 2018.

[153] Kim Christensen. *Percolation theory*. Imperial College London, 2002.

[154] P. R. King, S. V. Buldyrev, Nikolay V. Dokholyan, S. Havlin, Y. Lee, G. Paul, H. E. Stanley, and N. Vandesteeg. Predicting oil recovery using percolation theory. *Petroleum Geoscience*, 7(S):S105–S107, 2001.

[155] Graeme P. Boswell, Nicholas F. Britton, and Nigel R. Franks. Habitat fragmentation, percolation theory and the conservation of a keystone species. *Proceedings of the Royal Society of London. Series B: Biological Sciences*, 265(1409):1921–1925, 1998.

[156] Rose M. Mutiso and Karen I. Winey. Electrical percolation in quasi-two-dimensional metal nanowire networks for transparent conductors. *Physical Review E*, 88(3):032134, 2013.

[157] Stephan Mertens and Cristopher Moore. Continuum percolation thresholds in two dimensions. *Physical Review E*, 86(6):061109, 2012.

[158] William Thomas Tutte and William Thomas Tutte. *Graph theory*, volume 21. Cambridge University Press, 2001.

[159] Python 3.11.2. https://docs.python.org/3.

[160] Constantine Pozrikidis. *An introduction to grids, graphs, and networks.* Oxford University Press, 2014.

[161] Gilbert Strang and L. B. Freund. Introduction to applied mathematics. *Journal of Applied Mechanics*, 53(2):480, 1986.

[162] István Vágó and István Vágó. *Graph theory: Application to the calculation of electrical networks*, volume 15. Elsevier Science Limited, 1985.

[163] Hugh G. Manning, Fabio Niosi, Claudia Gomes da Rocha, Allen T. Bellew, Colin O'Callaghan, Subhajit Biswas, Patrick F. Flowers, Benjamin J. Wiley, Justin D. Holmes, Mauro S. Ferreira, et al. Emergence of winner-takes-all connectivity paths in random nanowire networks. *Nature Communications*, 9:3219, 2018.

[164] Jiantong Li and Shi-Li Zhang. Finite-size scaling in stick percolation. *Physical Review E*, 80(4):040104, 2009.

[165] O. Kallmes and H. Corte. The structure of paper, I. The statistical geometry of an ideal two dimensional fiber network. *TAPPI J.*, 43(9):737–752, 1960.

[166] Sukanta De, Paul J. King, Philip E. Lyons, Umar Khan, and Jonathan N. Coleman. Size effects and the problem with percolation in nanostructured transparent conductors. *ACS Nano*, 4(12):7064–7072, 2010.

[167] Sophie Sorel, Philip E. Lyons, Sukanta De, Janet C. Dickerson, and Jonathan N. Coleman. The dependence of the optoelectrical properties of silver nanowire networks on nanowire length and diameter. *Nanotechnology*, 23(18):185201, 2012.

[168] Sadhan Samanta, Priyanka Sarkar, Santanu Pyne, Gobinda Prasad Sahoo, and Ajay Misra. Synthesis of silver nanodiscs and triangular nanoplates in PVP matrix: photophysical study and simulation of UV–vis extinction spectra using DDA method. *Journal of Molecular Liquids*, 165:21–26, 2012.

[169] Jan Schaefer, S. C. Lee, and Alwin Kienle. Calculation of the near fields for the scattering of electromagnetic waves by multiple infinite cylinders at perpendicular incidence. *Journal of Quantitative Spectroscopy and Radiative Transfer*, 113(16):2113–2123, 2012.

[170] Gustav Mie. Beiträge zur optik trüber medien, speziell kolloidaler metallösungen. *Annalen Der Physik*, 330(3):377–445, 1908.

[171] Tatyana A. Bashkatova, Alexey N. Bashkatov, Vyacheslav I. Kochubey, and Valery V. Tuchin. Light-scattering properties for spherical and cylindrical particles: a simple approximation derived from Mie calculations. In *Saratov Fall Meeting 2000: Optical Technologies in Biophysics and Medicine II*, volume 4241, pages 247–259. SPIE, 2001.

[172] Peter B. Johnson and R. W. Christy. Optical constants of the noble metals. *Physical Review B*, 6(12):4370, 1972.

[173] Aleksandar D. Rakić. Algorithm for the determination of intrinsic optical constants of metal films: application to aluminum. *Applied Optics*, 34(22):4755–4767, 1995.

[174] Mikhail Polyanskiy. `https://refractiveindex.info`.

[175] Mayuri Kashyap, Aparajita Bandyopadhyay, and Amartya Sengupta. Studying the scattering of electromagnetic wave by a composite 3D model at terahertz frequencies. `https://www.comsol.com/paper`, Technical Papers and Presentations, 2019.

[176] Sergei Yushanov, Jeffrey S. Crompton, and Kyle C. Koppenhoefer. Mie scattering of electromagnetic waves. In *Proceedings of the COMSOL Conference*, volume 116, 2013.

[177] Stefan A. Maier. *Plasmonics: fundamentals and applications*, volume 1. Springer, 2007.

[178] Vladimir D. Miljković, Timur Shegai, Peter Johansson, and Mikael Käll. Simulating light scattering from supported plasmonic nanowires. *Optics Express*, 20(10):10816–10826, 2012.

[179] Lisa V. Brown, Heidar Sobhani, J. Britt Lassiter, Peter Nordlander, and Naomi J. Halas. Heterodimers: plasmonic properties of mismatched nanoparticle pairs. *ACS Nano*, 4(2):819–832, 2010.

[180] Dirk Jan Dikken, Marko Spasenović, Ewold Verhagen, Dries van Oosten, and L. Kobus Kuipers. Characterization of bending losses for curved plasmonic nanowire waveguides. *Optics Express*, 18(15):16112–16119, 2010.

[181] Ji-Young Kim, Myung-Geun Han, Miao-Bin Lien, Sergei Magonov, Yimei Zhu, Heather George, Theodore B. Norris, and Nicholas A. Kotov. Dipole-like electrostatic asymmetry of gold nanorods. *Science Advances*, 4(2):e1700682, 2018.

[182] CMC Microsystems. https://www.cmc.ca.

[183] Manjeet Singh and Sravendra Rana. Silver and copper nanowire films as cost-effective and robust transparent electrode in energy harvesting through photovoltaic: a review. *Materials Today Communications*, 24:101317, 2020.

[184] Arshad Khan. *Novel embedded metal-mesh transparent electrodes: vacuum-free fabrication strategies and applications in flexible electronic devices*. Springer Nature, 2020.

[185] T. S. Sathiaraj. Effect of annealing on the structural, optical and electrical properties of ITO films by RF sputtering under low vacuum level. *Microelectronics Journal*, 39(12):1444–1451, 2008.

[186] Thomas Sannicolo, Mélanie Lagrange, Anthony Cabos, Caroline Celle, Jean-Pierre Simonato, and Daniel Bellet. Metallic nanowire-based transparent electrodes for next generation flexible devices: a review. *Small*, 12(44):6052–6075, 2016.

[187] Sedigheh Pirsalami, Seyed Mojtaba Zebarjad, and Habib Daneshmanesh. An overview of metallic nanowire networks, promising building blocks for next generation trans-

parent conductors: emergence, fundamentals and challenges. *Journal of Electronic Materials*, 46(8):4707–4715, 2017.

[188] Bong Sup Shim, Jian Zhu, Edward Jan, Kevin Critchley, and Nicholas A. Kotov. Transparent conductors from layer-by-layer assembled SWNT films: importance of mechanical properties and a new figure of merit. *ACS Nano*, 4(7):3725–3734, 2010.

[189] Fei Han, Thirupathi Maloth, Gilles Lubineau, Recep Yaldiz, and Amit Tevtia. Computational investigation of the morphology, efficiency, and properties of silver nano wires networks in transparent conductive film. *Scientific Reports*, 8:17494, 2018.

[190] Jinyoung Hwang, Hiesang Sohn, and Sang Hyun Lee. Computational characterization and control of electrical conductivity of nanowire composite network under mechanical deformation. *Scientific Reports*, 8:16617, 2018.

[191] Milind Jagota and Nelson Tansu. Conductivity of nanowire arrays under random and ordered orientation configurations. *Scientific Reports*, 5:10219, 2015.

[192] Mohammad-Reza Azani, Azin Hassanpour, Yuri Yu Tarasevich, Irina V. Vodolazskaya, and Andrei V. Eserkepov. Transparent electrodes with nanorings: a computational point of view. *Journal of Applied Physics*, 125(23):234903, 2019.

[193] A. Belardini, M. Centini Larciprete, M. Centini, E. Fazio, C. Sibilia, D. Chiappe, C. Martella, A. Toma, M. Giordano, and F. Buatier De Mongeot. Circular dichroism in the optical second-harmonic emission of curved gold metal nanowires. *Physical Review Letters*, 107(25):257401, 2011.

[194] Ye Zhang, Jiangna Guo, Dan Xu, Yi Sun, and Feng Yan. Synthesis of ultrathin semicircle-shaped copper nanowires in ethanol solution for low haze flexible transparent conductors. *Nano Research*, 11(7):3899–3910, 2018.

[195] Sophie Sorel, Daniel Bellet, and Jonathan N. Coleman. Relationship between material properties and transparent heater performance for both bulk-like and percolative nanostructured networks. *ACS Nano*, 8(5):4805–4814, 2014.

[196] Faisal Shahzad, Mohamed Alhabeb, Christine B. Hatter, Babak Anasori, Soon Man Hong, Chong Min Koo, and Yury Gogotsi. Electromagnetic interference shielding with 2D transition metal carbides (MXenes). *Science*, 353(6304):1137–1140, 2016.

[197] Bing Zhou, Mengjie Su, Daozheng Yang, Gaojie Han, Yuezhan Feng, Bo Wang, Jialu Ma, Jianmin Ma, Chuntai Liu, and Changyu Shen. Flexible MXene/silver nanowire-based transparent conductive film with electromagnetic interference shielding and electro-photo-thermal performance. *ACS Applied Materials & Interfaces*, 12(36):40859–40869, 2020.

[198] Wenting Li, Huan Zhang, Shengwei Shi, Jinxin Xu, Xin Qin, Qiqi He, Kecong Yang, Wubin Dai, Gang Liu, Quanguo Zhou, et al. Recent progress in silver nanowire networks for flexible organic electronics. *Journal of Materials Chemistry C*, 8(14):4636–4674, 2020.

[199] Dong Gyu Kim, Jong Han Choi, Duck-Kyun Choi, and Sang Woo Kim. Highly bendable and durable transparent electromagnetic interference shielding film prepared by wet sintering of silver nanowires. *ACS Applied Materials & Interfaces*, 10(35):29730–29740, 2018.

[200] Parveen Saini and Manju Arora. Microwave absorption and EMI shielding behavior of nanocomposites based on intrinsically conducting polymers, graphene and carbon nanotubes. *New Polymers for Special Applications*, 3:73–112, 2012.

[201] Xiaojuan Ni, Chao Hui, Ninghai Su, Wei Jiang, and Feng Liu. Monte Carlo simulations of electrical percolation in multicomponent thin films with nanofillers. *Nanotechnology*, 29(7):075401, 2018.

[202] Philip E. Lyons, Sukanta De, Jamil Elias, Matthias Schamel, Laetitia Philippe, Allen T. Bellew, John J. Boland, and Jonathan N. Coleman. High-performance transparent conductors from networks of gold nanowires. *The Journal of Physical Chemistry Letters*, 2(24):3058–3062, 2011.

[203] Kevin Critchley, Bishnu P. Khanal, Marcin Ł. Górzny, Leonid Vigderman, Stephen D. Evans, Eugene R. Zubarev, and Nicholas A. Kotov. Near-bulk conductivity of gold nanowires as nanoscale interconnects and the role of atomically smooth interface. *Advanced Materials*, 22(21):2338–2342, 2010.

[204] Junmo Lee and Jaewook Nam. Percolation threshold of curved linear objects. *Physical Review E*, 103(1):012126, 2021.

[205] Wanbo Li, Kangning Ren, and Jianhua Zhou. Aluminum-based localized surface plasmon resonance for biosensing. *TrAC Trends in Analytical Chemistry*, 80:486–494, 2016.

[206] Eleonora Petryayeva and Ulrich J. Krull. Localized surface plasmon resonance: nanostructures, bioassays and biosensing—a review. *Analytica Chimica Acta*, 706(1):8–24, 2011.

[207] William L. Barnes. Particle plasmons: why shape matters. *American Journal of Physics*, 84(8):593–601, 2016.

[208] Sukjoon Hong, Habeom Lee, Jinhwan Lee, Jinhyeong Kwon, Seungyong Han, Young D. Suh, Hyunmin Cho, Jaeho Shin, Junyeob Yeo, and Seung Hwan Ko. Highly stretchable and transparent metal nanowire heater for wearable electronics applications. *Advanced Materials*, 27(32):4744–4751, 2015.

[209] Nesrine Jaziri, Ayda Boughamoura, Jens Müller, Brahim Mezghani, Fares Tounsi, and Mohammed Ismail. A comprehensive review of thermoelectric generators: technologies and common applications. *Energy Reports*, 6:264–287, 2020.

[210] Franz Selzer, Carlo Floresca, David Kneppe, Ludwig Bormann, Christoph Sachse, Nelli Weiß, Alexander Eychmüller, Aram Amassian, Lars Müller-Meskamp, and Karl Leo. Electrical limit of silver nanowire electrodes: direct measurement of the nanowire junction resistance. *Applied Physics Letters*, 108(16):163302, 2016.

[211] Jianfang Liu, Yongjie Ge, Dumeng Zhang, Mei Han, Moxia Li, Meng Zhang, Xidong Duan, Zhilin Yang, and Jiawen Hu. Plasma cleaning and self-limited welding of silver nanowire films for flexible transparent conductors. *ACS Applied Nano Materials*, 4(2):1664–1671, 2021.

[212] Gui-Shi Liu, Ting Wang, Yexiong Wang, Huajian Zheng, Yunsen Chen, Zijie Zeng, Lei Chen, Yaofei Chen, Bo-Ru Yang, Yunhan Luo, et al. One-step plasmonic welding and photolithographic patterning of silver nanowire network by UV-programable surface atom diffusion. *Nano Research*, 15:2582–2591, 2022.

[213] Jihun Noh and Dongsik Kim. Laser shock pressing of silver nanowires on flexible substrates to fabricate highly uniform transparent conductive electrode films. *Nanotechnology*, 32(15):155303, 2021.

[214] S .V. N. Pammi, Venkatraju Jella, Jin-Seok Choi, and Soon-Gil Yoon. Enhanced thermoelectric properties of flexible Cu_{2-x} Se ($x \geq 0.25$) NW/polyvinylidene fluoride composite films fabricated via simple mechanical pressing. *Journal of Materials Chemistry C*, 5(3):763–769, 2017.

[215] Jong-Seol Park, Tae-Gon Park, and Jin-Seok Park. Characterization of silver nanowire flexible transparent electrode with grid pattern formed via thermocompression. *Electronic Materials Letters*, 17:260–267, 2021.

[216] D. P. Langley, Mélanie Lagrange, Gael Giusti, Carmen Jiménez, Yves Bréchet, Ngoc Duy Nguyen, and Daniel Bellet. Metallic nanowire networks: effects of thermal annealing on electrical resistance. *Nanoscale*, 6(22):13535–13543, 2014.

[217] Jinwei Gao, Zhike Xian, Guofu Zhou, Jun-Ming Liu, and Krzysztof Kempa. Nature-inspired metallic networks for transparent electrodes. *Advanced Functional Materials*, 28(24):1705023, 2018.

[218] Moon Kyu Kwak, Jong G. Ok, Jae Yong Lee, and L. Jay Guo. Continuous phase-shift lithography with a roll-type mask and application to transparent conductor fabrication. *Nanotechnology*, 23(34):344008, 2012.

[219] K. D. M. Rao, Christoph Hunger, Ritu Gupta, Giridhar U. Kulkarni, and Mukundan Thelakkat. A cracked polymer templated metal network as a transparent conducting electrode for ITO-free organic solar cells. *Physical Chemistry Chemical Physics*, 16(29):15107–15110, 2014.

[220] Mozakkar Hossain, Gundam Sandeep Kumar, S. N. Barimar Prabhava, Emmet D. Sheerin, David McCloskey, Somobrata Acharya, K. D. M. Rao, and John J. Boland. Transparent, flexible silicon nanostructured wire networks with seamless junctions for high-performance photodetector applications. *ACS Nano*, 12(5):4727–4735, 2018.

[221] K. D. M. Rao, Ritu Gupta, and Giridhar U. Kulkarni. Fabrication of large area, high-performance, transparent conducting electrodes using a spontaneously formed crackle network as template. *Advanced Materials Interfaces*, 1(6):1400090, 2014.

[222] M. G. Kang and L. Jay Guo. Nanoimprinted semitransparent metal electrodes and their application in organic light-emitting diodes. *Advanced Materials*, 19(10):1391–1396, 2007.

[223] Ritu Gupta and Giridhar U. Kulkarni. Holistic method for evaluating large area transparent conducting electrodes. *ACS Applied Materials & Interfaces*, 5(3):730–736, 2013.

[224] Jingyu Zou, Hin-Lap Yip, Steven K. Hau, and Alex K. Y. Jen. Metal grid/conducting polymer hybrid transparent electrode for inverted polymer solar cells. *Applied Physics Letters*, 96(20):96, 2010.

[225] Yang Zhao, Matthew L. Fitzgerald, Yi Tao, Zhiliang Pan, Godfrey Sauti, Dongyan Xu, Ya-Qiong Xu, and Deyu Li. Electrical and thermal transport through silver nanowires and their contacts: effects of elastic stiffening. *Nano Letters*, 20(10):7389–7396, 2020.

[226] Maxime Verdier, David Lacroix, and Konstantinos Termentzidis. Thermal transport in two-and three-dimensional nanowire networks. *Physical Review B*, 98(15):155434, 2018.

[227] Cheng Zhang, Chengang Ji, Yong-Bum Park, and L. Jay Guo. Thin-metal-film-based transparent conductors: Material preparation, optical design, and device applications. *Advanced Optical Materials*, 9(3):2001298, 2021.

[228] Su Shen, Shi-Yu Chen, Dong-Yu Zhang, and Yan-Hua Liu. High-performance composite Ag-Ni mesh based flexible transparent conductive film as multifunctional devices. *Optics Express*, 26(21):27545–27554, 2018.

[229] A. S. Voronin, Y. V. Fadeev, I. V. Govorun, I. V. Podshivalov, M. M. Simunin, I. A. Tambasov, D. V. Karpova, T. E. Smolyarova, A. V. Lukyanenko, A. A. Karacharov, et al. Cu–Ag and Ni–Ag meshes based on cracked template as efficient transparent electromagnetic shielding coating with excellent mechanical performance. *Journal of Materials Science*, 56(26):14741–14762, 2021.

[230] Monee K. Roul, Jasmine Beckford, Brandon Obasogie, Kelsea Yarbrough, Messaoud Bahoura, and A. K. Pradhan. High-performance transparent film heater using random mesowire silver network. *Journal of Materials Science: Materials in Electronics*, 29:21088–21096, 2018.

[231] Bing Han, Yuanlin Huang, Ruopeng Li, Qiang Peng, Junyi Luo, Ke Pei, Andrzej Herczynski, Krzysztof Kempa, Zhifeng Ren, and Jinwei Gao. Bio-inspired networks for optoelectronic applications. *Nature Communications*, 5:5674, 2014.

[232] Jinwook Jung, Kyun Kyu Kim, Young D. Suh, Sukjoon Hong, Junyeob Yeo, and Seung Hwan Ko. Recent progress in controlled nano/micro cracking as an alternative nano-patterning method for functional applications. *Nanoscale Horizons*, 5(7):1036–1049, 2020.

[233] Qiang Peng, Songru Li, Bing Han, Qikun Rong, Xubing Lu, Qianming Wang, Min Zeng, Guofu Zhou, Jun-Ming Liu, Krzysztof Kempa, et al. Colossal figure of merit in transparent-conducting metallic ribbon networks. *Advanced Materials Technologies*, 1(6), 2016.

[234] Christopher P. Muzzillo. Metal nano-grids for transparent conduction in solar cells. *Solar Energy Materials and Solar Cells*, 169:68–77, 2017.

[235] Shapley 1.0.3. https://pypi.org/project/shapley.

[236] Networkx 3.2. https://networkx.org.

[237] Scipy 1.10.1. https://scipy.org.

[238] Mengqi Cui, Xiaohan Zhang, Qikun Rong, Li Nian, Lingling Shui, Guofu Zhou, and Na Li. High conductivity and transparency metal network fabricated by acrylic colloidal self-cracking template for flexible thermochromic device. *Organic Electronics*, 83:105763, 2020.

[239] Vivekanandan Raman, Yong-Hwan Cho, Hye-Min Kim, Yong-Jun Kim, Hyeong-Min Sim, and Han-Ki Kim. Ag mesh network framework based nano composite for transparent conductive functional electrodes for capacitive touch sensor and thin film heater. *Ceramics International*, 47(19):27230–27240, 2021.

[240] Bobby Singh Soram, Jiuyi Dai, Tolendra Kshetri, Nam Hoon Kim, and Joong Hee Lee. Vertically grown and intertwined $Co(OH)_2$ nanosheez@Ni-mesh network for transparent flexible supercapacitor. *Chemical Engineering Journal*, 391:123540, 2020.

[241] Kin Wai Cheuk, Ke Pei, and Paddy K. L. Chan. Degradation mechanism of a junction-free transparent silver network electrode. *RSC Advances*, 6(77):73769–73775, 2016.

[242] Claude Indermitte, T. h .M. Liebling, Marc Troyanov, and Heinz Clémençon. Voronoi diagrams on piecewise flat surfaces and an application to biological growth. *Theoretical Computer Science*, 263(1-2):263–274, 2001.

[243] J. E. Bolander Jr and Shigehiko Saito. Fracture analyses using spring networks with random geometry. *Engineering Fracture Mechanics*, 61(5-6):569–591, 1998.

[244] Michael T. Carlson, Andrew J. Green, Aurangzeb Khan, and Hugh H. Richardson. Optical measurement of thermal conductivity and absorption cross-section of gold nanowires. *The Journal of Physical Chemistry C*, 116(15):8798–8803, 2012.

[245] N. Stojanovic, J. M. Berg, D. H. S. Maithripala, and M. Holtz. Direct measurement of thermal conductivity of aluminum nanowires. *Applied Physics Letters*, 95(9):091905, 2009.

[246] Wei-Tsu Peng, Fu-Ren Chen, and Ming-Chang Lu. Thermal conductivity and electrical resistivity of single copper nanowires. *Physical Chemistry Chemical Physics*, 23(36):20359–20364, 2021.

[247] Voronoi Grid Generator. https://github.com/bonafid3/voronoi.

[248] Gholamreza Kadkhodaei, Keyhan Sheshyekani, and Mohsen Hamzeh. Coupled electric–magnetic–thermal–mechanical modelling of busbars under short-circuit conditions. *IET Generation, Transmission & Distribution*, 10(4):955–963, 2016.

[249] Joyce Harrington Anderson. *Measurement of Thermal Conductivity of Gold Nanofilms and Nanowires*. PhD thesis, Texas State University, 2020.

[250] Hazim B. Awbi. Calculation of convective heat transfer coefficients of room surfaces for natural convection. *Energy and Buildings*, 28(2):219–227, 1998.

[251] Matthew L. Fitzgerald, Yang Zhao, Zhiliang Pan, Lin Yang, Shihong Lin, Godfrey Sauti, and Deyu Li. Contact thermal resistance between silver nanowires with poly (vinylpyrrolidone) interlayers. *Nano Letters*, 21(10):4388–4393, 2021.

[252] S. B. DiCenzo and G. K. Wertheim. Monte Carlo calculation of the size distribution of supported clusters. *Physical Review B*, 39(10):6792, 1989.

[253] Járai-Szabó Ferenc and Zoltán Néda. On the size distribution of poisson voronoi cells. *Physica A: Statistical Mechanics and its Applications*, 385(2):518–526, 2007.

[254] Xóchitl López-Lozano, Hector Barron, Christine Mottet, and Hans-Christian Weissker. Aspect-ratio-and size-dependent emergence of the surface-plasmon resonance in gold nanorods– an ab initio TDDFT study. *Physical Chemistry Chemical Physics*, 16(5):1820–1823, 2014.

[255] Lucas V. Besteiro, Xiang-Tian Kong, Zhiming Wang, Gregory Hartland, and Alexander O. Govorov. Understanding hot-electron generation and plasmon relaxation in metal nanocrystals: quantum and classical mechanisms. *ACS Photonics*, 4(11):2759–2781, 2017.

[256] Abhishek Chowdhury and Sudeep Bhattacharjee. Experimental investigation of change in sheet resistance and Debye temperatures in metallic thin films due to low-energy ion beam irradiation. *Journal of Physics D: Applied Physics*, 46(43):435304, 2013.

[257] Huachun Wang, Chenping Wu, Youyang Huang, Feipeng Sun, Na Lin, Abdul Majid Soomro, Zhibai Zhong, Xiaodong Yang, Xiaohong Chen, Junyong Kang, et al. One-pot synthesis of superfine core–shell Cu@metal nanowires for highly tenacious transparent LED dimmer. *ACS Applied Materials & Interfaces*, 8(42):28709–28717, 2016.

[258] Po-Chun Hsu, Xiaoge Liu, Chong Liu, Xing Xie, Hye Ryoung Lee, Alex J. Welch, Tom Zhao, and Yi Cui. Personal thermal management by metallic nanowire-coated textile. *Nano Letters*, 15(1):365–371, 2015.

[259] Malkeshkumar Patel, Ji Heun Seo, Sangho Kim, Thanh Tai Nguyen, Manjeet Kumar, Juhyung Yun, and Joondong Kim. Photovoltaic-driven transparent heater of ZnO-coated silver nanowire networks for self-functional remote power system. *Journal of Power Sources*, 491:229578, 2021.

[260] V. Bahadur, J. Xu, Y. Liu, and T. S. Fisher. Thermal resistance of nanowire-plane interfaces. *J. Heat Transfer*, 127(6):664–668, 2005.

[261] Tianzhuo Zhan, Shuaizhe Ma, Zhicheng Jin, Hiroki Takezawa, Kohei Mesaki, Motohiro Tomita, Yen-Ju Wu, Yibin Xu, Takashi Matsukawa, Takeo Matsuki, et al. Effect of the thermal boundary resistance in metal/dielectric thermally conductive layers on power generation of silicon nanowire microthermoelectric generators. *ACS Applied Materials & Interfaces*, 12(30):34441–34450, 2020.

[262] Hahn-Gil Cheong, Ross E. Triambulo, Gun-Hwan Lee, In-Sook Yi, and Jin-Woo Park. Silver nanowire network transparent electrodes with highly enhanced flexibility by welding for application in flexible organic light-emitting diodes. *ACS Applied Materials & Interfaces*, 6(10):7846–7855, 2014.

[263] Dustin Chen, Jiajie Liang, and Qibing Pei. Flexible and stretchable electrodes for next generation polymer electronics: a review. *Science China Chemistry*, 59(6):659–671, 2016.

[264] Shiliang Wang, Zhiwei Shan, and Han Huang. The mechanical properties of nanowires. *Advanced Science*, 4(4):1600332, 2017.

[265] Jianhua Liu, Donglin Jia, James M. Gardner, Erik M. J. Johansson, and Xiaoliang Zhang. Metal nanowire networks: Recent advances and challenges for new generation photovoltaics. *Materials Today Energy*, 13:152–185, 2019.

[266] Minkyu Park, Wonsik Kim, Byungil Hwang, and Seung Min Han. Effect of varying the density of Ag nanowire networks on their reliability during bending fatigue. *Scripta Materialia*, 161:70–73, 2019.

[267] Marco Bobinger, Josef Mock, Paolo La Torraca, Markus Becherer, Paolo Lugli, and Luca Larcher. Tailoring the aqueous synthesis and deposition of copper nanowires for transparent electrodes and heaters. *Advanced Materials Interfaces*, 4(20):1700568, 2017.

[268] Marco Bobinger, Paolo La Torraca, Josef Mock, Markus Becherer, Luca Cattani, Diego Angeli, Luca Larcher, and Paolo Lugli. Solution-processing of copper nanowires for transparent heaters and thermo-acoustic loudspeakers. *IEEE Transactions on Nanotechnology*, 17(5):940–947, 2018.

[269] Le Zhao, Shihui Yu, Xiaopeng Li, Muying Wu, and Lingxia Li. High-performance copper mesh transparent flexible conductors based on electroplating with vacuum-free processing. *Organic Electronics*, 82:105511, 2020.

[270] S. Kiruthika, Ritu Gupta, and Giridhar U. Kulkarni. Large area defrosting windows based on electrothermal heating of highly conducting and transmitting Ag wire mesh. *RSC Advances*, 4(91):49745–49751, 2014.

[271] Jingqi Tao, Shuxin Li, Jun Shi, and Shulin Ji. Enhancing the optical response speed of thermochromic paper displays by heat exchange manipulation of invisible heaters. *ACS Applied Energy Materials*, 6(5):2897–2905, 2023.

[272] Ritu Gupta, K. D. M. Rao, Kartikeya Srivastava, Ankush Kumar, S. Kiruthika, and Giridhar U. Kulkarni. Spray coating of crack templates for the fabrication of transparent conductors and heaters on flat and curved surfaces. *ACS Applied Materials & Interfaces*, 6(16):13688–13696, 2014.

[273] S. Kiruthika, K. D. M. Rao, Ankush Kumar, Ritu Gupta, and G. U. Kulkarni. Metal wire network based transparent conducting electrodes fabricated using interconnected crackled layer as template. *Materials Research Express*, 1(2):026301, 2014.

[274] K. D. M. Rao and Giridhar U. Kulkarni. A highly crystalline single Au wire network as a high temperature transparent heater. *Nanoscale*, 6(11):5645–5651, 2014.

[275] Xinzuo Huang, Fenghua Zhang, and Jinsong Leng. Metal mesh embedded in colorless shape memory polyimide for flexible transparent electric-heater and actuators. *Applied Materials Today*, 21:100797, 2020.

[276] Tao Chen, Heping Li, Jing Li, Sanyuan Hu, Pin Ye, and Youwei Yan. Direct writing of silver microfiber with precise control on patterning for robust and flexible ultrahigh-performance transparent conductor. *Journal of Materials Science & Technology*, 47:103–112, 2020.

[277] Ritu Gupta, Sunil Walia, Markus Hösel, Jacob Jensen, Dechan Angmo, Frederik C. Krebs, and Giridhar U. Kulkarni. Solution processed large area fabrication of Ag patterns as electrodes for flexible heaters, electrochromics and organic solar cells. *Journal of Materials Chemistry A*, 2(28):10930–10937, 2014.

[278] Baekhoon Seong, Hyunwoong Yoo, Vu Dat Nguyen, Yonghee Jang, Changkook Ryu, and Doyoung Byun. Metal-mesh based transparent electrode on a 3-d curved surface by electrohydrodynamic jet printing. *Journal of Micromechanics and Microengineering*, 24(9):097002, 2014.

[279] Eshwar Thouti, Chirag Mistry, Achu Chandran, Deepak Kumar Panwar, Prem Kumar, Heena Suman, and Jamil Akhtar. Study of seamless Au mesh flexible transparent heaters: Influence of mesh coverage. *Journal of Physics D: Applied Physics*, 52(42):425301, 2019.

Appendix A

Supplementary Information: Chapter 4

This material is based on Esteki et al. "Thermo-electro-optical properties of seamless metallic nanowire networks for transparent conductor applications" (supplementary information) published in Nanoscale [106].

Table A.1 presents a comprehensive literature review of the electro-thermal characteristics of different NWN configurations composed of metallic materials including Ag, Au, Al, and Cu [106]. These NWNs were fabricated with varying device dimensions and exposed to diverse bias voltages. Notably, these works have already addressed the topic of transparent conductors possessing optical transmissions of a sufficiently high magnitude (i.e. $\gtrsim 90\%$). Consequently, this particular information has been omitted from the table. The present study demonstrates a high degree of concurrence between the outcomes of our computational examination and the previously reported (empirical) observations, thereby attesting to the robustness of our computational analysis. Despite the smaller dimensions of our seamless NWNs, the electrothermal outcomes demonstrate consistency with the experimental results. The reduced dimensions of our NWNs suggest enhanced electrical and thermal conductivity, making them highly suitable for use as transparent electrodes. Several notable findings from

the table deserve attention as follows:

- The average temperatures we obtained for seamless Cu NWNs align with the results reported in references [267] and [268]. However, they are significantly lower compared to the findings of reference [269]. It is worth noting that reference [269] investigated regular seamless Cu meshes, which can exhibit considerable differences in temperature distributions when compared to the more disordered network frames, such as the Voronoi arrangement studied in our work.

- The literature contains a broad range of average temperatures achieved for seamless Ag NWNs, as indicated in the first five rows of the table. Our results are consistent with the findings of references [230] and [270], in which Voronoi-like Ag NWNs fabricated on insulating substrates were investigated experimentally. Other experimental setups result in temperature differences as for the case of reference [271], in which Ag NWNs were utilized as paper-based heaters. Figure 4.14 showcases how adjusting the contact thermal conductance enables tuning the thermal interaction between the NWN and the substrate. That figure shows that elevating the contact thermal conductance leads to a notable decrease in the average temperature of Ag NWNs, reaching average temperature ranges of approximately ~300 K. Therefore, the NWN-substrate thermal interaction is an important factor to take into account when computing average temperatures of the network materials.

- The sheet resistance values reported in the cited works on Table A.1 appear to be comparatively lower than some of our estimations due to significant differences in the NWN sizes. It is worth noting that sheet resistance (R_s) values are significantly influenced by the contact resistance (R_c) between the NWN and the electrodes used for electrical interrogation. R_c is a quantity that can be challenging to determine precisely as it describes the contact resistance of an interface between two distinctive materials, the NWN and the electrode. In our simulations, we assumed sufficiently good contacts

between the NWN and the electrodes by setting $R_c \sim 1\ \Omega$ or $R_c \approx \langle R_{in} \rangle$, in which $\langle R_{in} \rangle$ is the average inner resistance of all nanowire segments within the Voronoi NWN. With the exception of the study in [271] which presents a wide range of sheet resistance values for Ag NWNs, our numerical predictions encompass the values of all selected works depicted on the table for seamless NWNs. We also included, for the sake of reference, sheet resistance values for NWNs of other layouts than the Voronoi arrangement such as grid mesh NWNs and junction-based (standard) NWNs.

Table A.1: Literature comparison of physical quantities reported in various studies, including experimental ones, as well as our own research, focusing on transparent conductors/heaters fabricated from NWNs [106]. 'PS' stands for 'present study', 'N/A' stands for 'not applicable' or 'not available' in the corresponding reference, 'Temp.' refers to temperature, 'R_s' is the sheet resistance, and 'Ref.' stands for 'reference'.

Material	W_w/D_w (μm)	Device Area	Voltage (V)	Temp. (K)	R_s (Ω/□)	Ref.
Ag[1]	55/0.08	2.5×2.5 cm^2	N/A	380	8	[128]
Ag[1]	N/A	5×5 cm^2	3-9	350	27-142	[271]
Ag[1]	100/125	4×2 cm^2	1-5	373	2-6	[272]
Ag[1]	2-9/1-5	2×2 cm^2	1-4	473	1.13	[230]
Ag[1]	21-70/0.3	10×8 cm^2	8.5	443	1	[270]
Au[1]	3–20/10	N/A	3-6	320-360	3-6	[273]
Au[1]	2-10/0.08	0.015×0.01 cm^2	0.7-1.5	373	1.5-10	[129]
Au[1]	0.5-2/0.06-0.22	2.5×2.5 cm^2	7-12	583-783	3.1-5.4	[274]
Al[2]	2-6/6.5	0.02×0.02 cm^2	4-14	323-573	3	[275]
Cu[3]	N/A/0.8	N/A	0.5-5	433	2-160	[269]
Ag[3]	Diameter: 0.055	N/A	1-4	323-573	1-10	[276]
Ag[3]	250/0.2	1×1 cm^2	0.8	343	2-4	[277]
Ag[3]	7/1.12	0.03×0.01 cm^2	5	380	2-7	[278]
Au[3]	5/0.15	2×2 cm^2	5.5	434	1.5-5.5	[279]
Cu[4]	Diameter: 0.25	5×5 cm^2	N/A	345	6.5	[267]
Cu[4]	Diameter: 0.115	3.5×5 cm^2	N/A	333	1-124	[268]
Ag[1]	0.05-0.5/0.05-2	50×50 μm^2	0.5-4.6	470	1-19	PS.
Au[1]	0.05-0.5/0.05-2	50×50 μm^2	0.5-4.6	425	1-28	PS.
Al[1]	0.05-0.5/0.05-2	50×50 μm^2	0.5-4.6	390	1-42	PS.
Cu[1]	0.05-0.5/0.05-2	50×50 μm^2	0.5-4.6	350	1-80	PS.

[1] Seamless NWN
[2] Hybrid Seamless NWN
[3] Grid Mesh NWN
[4] Standard NWN